CHARACTERIZATION OF

FEMTOSECOND LASER MACHINING

ON DIELECTRIC MATERIALS

CHARACTERIZATION OF FEMTOSECOND LASER MACHINING ON DIELECTRIC MATERIALS

By

MARIANA BUDIMAN, B.Eng.

A thesis

Submitted to the School of Graduate Studies

In Partial Fulfillment of the Requirements

For the Degree

Master of Applied Science

McMaster University

MASTER OF APPLIED SCIENCE (2008) McMaster University

(Department of Materials Science and Engineering) Hamilton, Ontario

TITLE: Characterization of Femtosecond Laser Machining on Dielectric Materials

AUTHOR: Mariana Budiman, B.Eng (Bandung Institute of Technology-Indonesia)

SUPERVISOR: Professor Gianluigi Botton

NUMBER OF PAGES: xvi, 170

ABSTRACT

This thesis presents the investigations of femtosecond laser machining on three different dielectric materials, namely quartz, sapphire and diamond. The laser micromachining experiments were performed with a Titanium:Sapphire solid state laser with a repetition rate of 1 kHz, centered at a wavelength of 800 nm and pulse duration of 150-200 femtoseconds (fs). A 5× microscope objective for surface micromachining and a 50× microscope objective for sub-surface micromachining. The 50× microscope objective was used to obtain a smaller spot size and a shorter confocal parameter.

The purpose of this research was to study the interaction between the femtosecond laser pulses and quartz, sapphire and diamond which have bandgap energies of 8.4 eV (λ=148 nm), 9.9 eV (125 nm), and c) diamond 5.5 eV (225 nm) respectively. Since the photon energy of the laser was below the wide bandgap energies of the aforementioned dielectrics, the materials were essentially transparent to the incident laser.

In order to study the behavior of the dielectric materials under femtosecond laser irradiation, several experiments with varying type and number of pulses (N) were performed, such as single pulse ablation, plural pulse ablation

($N \leq 10$ pulses), multiple pulse ablation ($N \leq 100$ pulses), and continuous lines micromachining on the surface and in the sub-surface of materials were performed. The features, damage, and structural changes introduced by femtosecond laser irradiation on the materials studied were characterized through examination of both the plan and cross-section views. The characterization process was carried out using optical microscopy (operated in the Nomarski mode), scanning electron microscopy, focused ion beam, atomic force microscopy, and transmission electron microscopy.

The laser micromachining demonstrated distinct behaviors of the three wide bandgap materials. Quartz was very prone to cracking and showed near-wavelength alternating crystalline and amorphous sub-structure with the orientation parallel with respect to the electric field direction. Sapphire showed sub-wavelength ripples formation in lower fluences. Finally, diamond showed a strong tendency for ripples formation from near- to sub-wavelength spacing with the orientation of the ripples perpendicular and parallel with respect to electric field polarization.

ACKNOWLEDGMENTS

I would like to thank God for guiding me in writing this thesis.

I would like to thank my supervisor, Gianluigi Botton. Gianluigi who has always been available for discussions, and I would like to thank him for being a perfectionist to the last detail and for being friendly companion in daily life. He provided me the freedom to follow my own thoughts and inclinations. He has given me a new world of research that I never experience by seeing something I can not see with my bare eyes.

I would like to thank Harold Haugen, Henry Tiedje, Eugene Hsu and Travis Crawford from the Photonic Research Laboratory where I did my laser micromachining work and had useful discussions and open-minded brainstorming. My special appreciation goes to Harold, who gave me very detailed attentions and suggestions in my research, and also to Eugene Hsu, who was cheerfully present with me in every micromachining experiment and who provided an excellent and discussion partner.

I would like to thank all the staffs at the CCEM, Andy Duft, Steve Koprich, and Julia Huang who helped me in the laboratory and in research.

I would like to thank my group, a best group that I can be with, especially for Nadi Braidy, Lina Gunawan, and Yang Shao who shared with me their broad knowledge and experiences about microscopy. I would also like to thank Beth McNally and David Rossouw who advised me in editing.

I would like to express my great appreciation to Gilles Payen, who always has a way to cheer me up when I am down. The one who can make me laugh and cry at the same time with jokes.

Finally, thank you to my parents and siblings, Eka Yuliana Budiman, Yoan Budiman, and Kristi Budi Prakoso who continually support me with love, care and prayer, and also encourage me in my distant journey.

TABLE OF CONTENTS

LIST OF TABLES

LIST OF FIGURES

1 Introduction

1.1 Overview of Ultrashort Pulse Laser Machining, Its Application and Interaction with Materials

This section will give an overview of ultrashort pulse laser machining and its application and interaction with materials. This chapter also specifies the work range of these investigations where it would be dedicated for dielectric materials or wide bandgap materials.

Femtosecond laser machining is a promising technique that offers precise and reproducible means of surface and sub-surface patterning and structuring on various materials and applications, from dielectric [1], metals [2], semiconductor [3, 4], medical, technical component, cutting tool processing, cornea [5-8], teeth and optoelectronic devices repair [9], ranging from transparent to opaque, soft to hard materials. Surface micromachining is widely applied in Micro-Electro-Mechanical Systems (MEMS) and Nano-Electro-Mechanical Systems (NEMS). These systems require less melting phase because of rapid energy deposition and a much smaller heat affected zone [10]. Other requirements include high precision, high cleanliness, less debris, reduced ablation threshold fluence and an

enhanced lateral and vertical precision as compared to machining with longer pulses [10-12]. Sub-surface micromachining can be used in the fabrication of photonic devices such as waveguides [13], optical fibre technology[14], microfluidic channels [15] and three dimensional optical storage arrays [16].

Ultrashort pulse laser machining is the term used for the sub-picosecond and femtosecond regime. In this research, only femtosecond pulses were employed. In the femtosecond regime, the duration of the laser pulse is shorter than the electron-phonon coupling time, thereby invalidating the assumption of an equilibrium state. The femtosecond lasers give high radiation intensity that has the ability to create high density plasmas. Consequently, the femtosecond pulse ablation can be considered as a solid-plasma transition. This short pulse duration is also shorter than the thermal diffusion time scale [17-19]. For these reasons, the femtosecond lasers can be used for micromachining with optimum energy deposition in a minimized volume and heat affected zone, as well as offering contamination-free machining.

The aforementioned special features can not be performed with longer pulse lasers (e.g. pulses in the nanosecond regime). The nanosecond time scale is much longer than the characteristic relaxation time in the systems, causing the existence of thermal diffusion and a melting phase. The duration of melting is on order of a few tens of nanoseconds.

We used a solid-state laser Ti:Sapphire that offers pulse-to-pulse stability and reliability, whereas gas lasers may be subject to pulse-to-pulse variations that

can be within ±10 %. Ti:Sapphire laser is also well suited for application involving surface modification since it exhibits stability over a wide wavelength range (720 nm to 1010 nm) and can produce femtosecond pulses at a number of wavelengths through a combination of nonlinear optical techniques [17].

The materials used in this research are α-quartz, sapphire, and diamond. They are all crystalline transparent materials with wide bandgap energies, e.g., quartz 8.4 eV (λ=148 nm) [20], sapphire 9.9 eV (125 nm) [20] and diamond 5.5 eV (225 nm) [20, 21]. These materials are important crystalline materials in the fields of optoelectronics, micro-optics and fiber technology due to their wide transparency spectra from UV to IR.

Nevertheless, several related studies about the interaction between femtosecond pulses and materials show evident damage and structural change. These studies primarily focus on surface modifications and investigations [22-29]. In our research, we want to expand upon these investigations, not only considering the surfaces, but also the sub-surface in wide bandgap materials. Sub-surface micromachining is usually followed by chemical etching to reveal the structures [30-36]. This study would exploit further the ability of the focused ion beam method to investigate the sub-structure, together with optical microscopy operated in the Nomarski mode, scanning electron microscopy (SEM), atomic force microscopy (AFM) operated in the contact mode, and transmission electron microscopy (TEM), such that the original feature and structure of the materials right after laser micromachining could be investigated and determined.

The Ti:Sapphire laser was centered at an 800 nm wavelength which is equivalent to a photon energy of 1.55 eV. This laser photon energy is below the bandgap of the three materials being studied. The average laser power (P_a) used for these experiments was typically 20 mW. With a repetition rate (f) of 1 kHz, the energy per pulse (E) will be

$$E = \frac{P_a}{f} = \frac{20.10^{-3}\left[Js^{-1}\right]}{1000\left[s^{-1}\right]} = 20[\mu J].$$

Such a small energy within a short pulse duration (τ_l) in the range of 150-200 femtoseconds (fs), will yield to a peak power (P_p) of

$$P_p = \frac{E}{\tau_l} = \frac{20[\mu J]}{200[fs]} = 100[MW]$$

and a peak intensity (I_p) of

$$I_p = \frac{P_p}{A} = \frac{100[MW]}{\pi(5.10^{-4})^2[cm^2]} \approx 15.10^{13}[Wcm^{-2}]$$

where A is the area of the laser beam, with beam radius (spot size) of approximately 5 μm. Even though the materials studied are transparent to the laser photons, the high intensity of the femtosecond laser allows for the machining of these materials through multiphoton and avalanche ionization processes [37, 38].

1.2 Thesis Outline

This thesis focuses on characterizing the femtosecond laser pulse machining of dielectric materials. Therefore the detailed processes will be mainly related to the characterizations methods and the materials.

This thesis consists of five chapters. Chapter 2 provides a brief background related to this femtosecond laser pulse machining work and all phenomena that are seen in this regime. Chapter 3 provides details of experimental techniques and procedures. Chapter 4 contains the results and discussions related to the experiments outlined in the previous chapter. There are three different series of study considering the three different samples that were investigated separately. Chapter 5 contains a summary and the conclusions reached.

2 Literature Review

2.1 Introduction

This chapter contains a background and literature review related to mechanisms of damage in femtosecond laser pulse ablation processes, the nature of breakdown in dielectric materials, and characterization methods which are used to investigate features on materials. The theories of laser ablation mechanisms in the femtosecond laser regime are still under discussion in the literature. Consequently some phenomena that have been observed in different experiments and materials sometimes can not be explained satisfactorily with established theory. In general, materials behave similarly after laser irradiation, but in some cases, specific materials showed distinctive behaviors. Those behaviors are due to the particular properties of each material. This chapter contains most of the references and literature reviews of the experiments that have been performed, nevertheless some of them will be included in later corresponding section to maintain simultaneous discussion.

2.2 Materials Selection Backgrounds

Investigations of wide bandgap materials are currently attracting significant interest. They are attracting due to their distinct mechanism of damage under laser machining compared to metals. The applications of wide bandgap materials in devices are becoming more important because of beneficial properties. The following sections provide detailed explanations of each material that has been selected for this research.

2.2.1 Quartz

Quartz is a well-known material that has piezoelectric properties [39, 40]. Thus it is often used as a resonator [41], transducer [42], pressure, thermal, corrosion, and biomedical sensor [41, 43-48]. Its superior optical properties also make quartz an important material for optoelectronics, laser-optics, and fiber technology. Quartz has low thermal conductivity, 7.5||a and 12.7||c W/mK at 250 K [20] and high chemical resistivity. The light transmission range of quartz is wide, 0.16-4 μm from UV to IR range [20]. Quartz is also used as an optical window in laser micromachining set-up. A high intensity of laser can damage optical components, so it is essential to find out the threshold of quartz with respect to laser irradiation. Quartz used in this experiment is a single crystal α-quartz with C-orientation. The orientation of the crystal was confirmed via an X-ray diffraction experiments with the Laue method.

2.2.2 Sapphire

Sapphire is one form of Al_2O_3 that is highly abundant on earth. Its natural state is in the form of white powder that is widely used in industry or research as an abrasive material. When this white powder is heated above 2050°C, it melts and can be grown as a single crystal. Sapphire windows that are very extensively used in laser-optics devices have the same crystal structure as the sapphire gemstone. Both sapphire windows and sapphire gemstones possess a rhombohedral crystal structure [40]. However sapphire windows and industrial sapphire have only negligible impurity and as a result they have the color of distilled–water and more controllable properties.

Favorable optical and mechanical properties of sapphire make it as an important choice in optical systems, laser optics, high pressure components and substrates. Because of its mechanical properties, sapphire has been used to make nozzles, acoustic rods, laser windows, and bearings. Its ability to transmit radiation over a broad wavelength range, 0.19-5.2 μm [20], from the vacuum ultra violet (VUV) to the infrared (IR) spectrum, combined with the mechanical properties have lead to the use of sapphire in space and military applications. Sapphire is also used in microfluidic chips [35]. Intensive research has been done to develop a large size sapphire crystals for laser interferometery based on its high density and superior quality factor [49].

This research used fine annealed sapphire windows made by Crystal Systems Inc[1] which has a purity of 99.996 % Al_2O_3 using the Heat Exchanger Method (HEM). The orientation of the crystal axis was C-Plane ± 2°. In a window, the C-direction is perpendicular to the face. The dimension of the circular sapphire window is 1±0.005 inches in diameter and 0.5±0.002 inches in thickness. It was ready polished at 80-50 (equivalent of one micro-inch), fine grind OD and flatness: 10 waves per inch of diameter.

This research will be dealing with the optical properties of the sapphire material. It is a highly important optical material because it combines high transmission with outstanding mechanical-strength properties at high and low temperatures. It is mentioned by the manufacturer that the VUV grade of sapphire is especially resistant to solarization and damage from radiation or high-power-density laser beams.

2.2.3 Diamond

Silicon (Si) is a first generation semiconductor in the 20th century, followed by gallium arsenide (GaAs) and indium phospide (InP) as second generation semiconductor in the turn of the 21st century, and silicon carbide (SiC) and gallium nitride (GaN) at the beginning of 21st century as third generation

---

[1] Crystal System Inc, 27 Congress Street, Salem MA 01970-5597, www.crystalsystem.com phone 978.745.0088 fax 978.744.5059

semiconductors. Diamond offers unique and suitable properties to be a candidate for a future generation semiconductor devices [50]. According to this trend, we are interested in investigating diamond.

Currently, diamond is used in applications such as microwave filters[51], acoustic wave filters[52, 53], sensors,[54], coatings, [55], detectors [56], heat sinks, micro- and nano-electro mechanical devices [35, 57, 58], and cutting tools[59-64]. All these applications are possible because of diamond's high mechanical hardness of 10 Mohs, high Young's modulus of 1100 GPa, high thermal conductivity of 2800 W/mK at 250 K, low friction coefficient, high transmission in broad range of wavelength of 0.24-2.7 μm and high refractive index of 2.42 [20]. However, the serious issue of graphitization on the surface by laser irradiation can degrade the performance of diamond in some cases [65-67].

The diamond window obtained from Harris International[2] was manufactured using the chemical vapor deposition method. The diamond window has a diameter of 2 mm and a thickness of 500 μm. This diamond is classified as type 2A which means it is effectively free of nitrogen impurities.

---

[2] Harris International, 35 West 45th St, New York, NY 10036, www.harrisinternational.com phone 212-869-3037 fax 212-764-0349

2.3 Femtosecond Laser Micromachining Background

This research is divided into two main activities. The first activity is femtosecond laser machining and the second is characterization of the features introduced by femtosecond laser machining. However, characterization is the main focus of this thesis. Since femtosecond laser machining of different materials have been studied by several other research groups, the details of femtosecond laser micromachining set-up have been discussed in *Femtosecond Laser Machining Manual* [68] and several different theses [69, 70]. In this thesis, only a general background related to micromachining will be described.

2.3.1 Femtosecond Pulse Laser Generation

The micromachining of hard materials was performed using laser pulses on the femtosecond time scale. The principle of femtosecond pulse laser generation is illustrated in Figure 2-1.

A continuous wave green laser beam at 532 nm was produced by frequency-doubled the output of a Nd:YVO_4 laser at 1064 nm (this system is called Millenia V). The Millenia V pumps a Ti:Sapphire mode-locked oscillator (Tsunami). This oscillator generates pulses with a duration of 90 fs and a wavelength of 800 nm that is subsequently amplified in a Ti:Sapphire Chirped Pulse Amplifier (CPA) (Spitfire).

The CPA system consists of three parts, a pulse stretcher, a regenerative pulse amplifier and a pulse compressor. The pulses are sent to the CPA (Spitfire)

system to obtain higher energy. In the CPA system, the ultrashort pulse is not amplified directly since this process has several challenges which must be overcome. In the ultrashort duration of the pulses, the energy is compressed in the very short time. In other words, the pulse intensity can be tremendous. Amplifying ultrashort pulses can lead to unwanted nonlinearity and damage of components in the amplifier. In order to resolve the problems, the output pulse from the oscillator is stretched to 220 ps to obtain lower intensity. The Ti:Sapphire regenerative amplifier is pumped by a Nd:YLF Q–Switched laser, frequency–doubled to 527 nm with a repetition rate of 1 kHz (Merlin). The stretched pulse from the pulse stretcher is then amplified into higher energy of 565 μJ with a wavelength of 800 nm at a repetition rate of 1 kHz. In these series of experiments, the output pulse from the regenerative amplifier is maximally recompressed in a pulse compressor to provide ~150 femtosecond pulses. The final pulse now has pulse duration of 150 fs, energy of 350 μJ, at a repetition rate of 1 kHz, and wavelength of 800 nm.

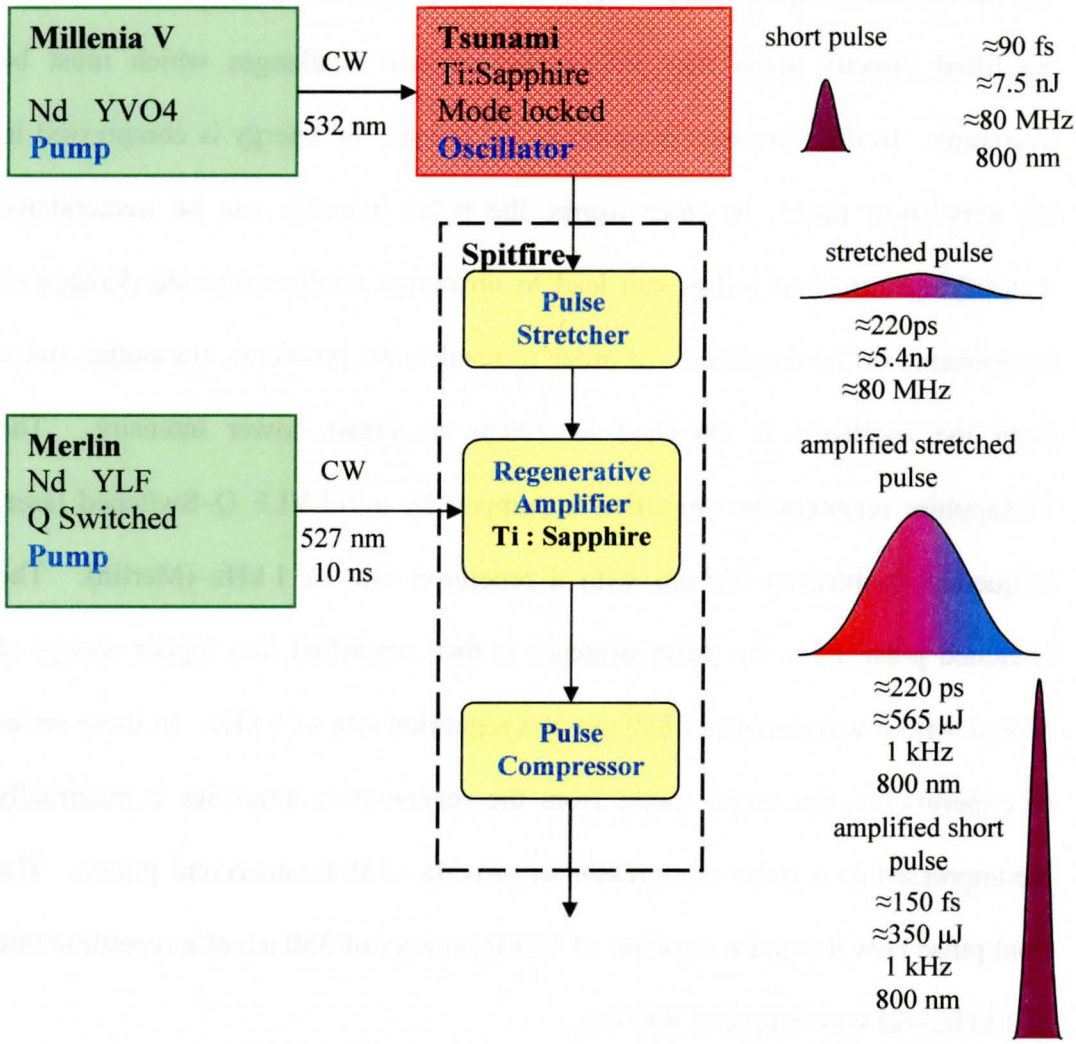

Figure 2-1: Representative diagrams of the principles of femtosecond laser pulse generation and the Chirped Pulse Amplification (CPA) system.

2.3.2 Pulse Spectrum

The laser pulse spectrum is monitored with an Ocean Optics PC2000 Spectrometer. Figure 2-2 is a screenshot of the Ocean Optics PC2000 Spectrometer software window that shows the output wavelength spectrum used

in all experiments, i.e. centered at 800 nm with ~10 nm FWHM bandwidth from the Ti:Sapphire oscillator.

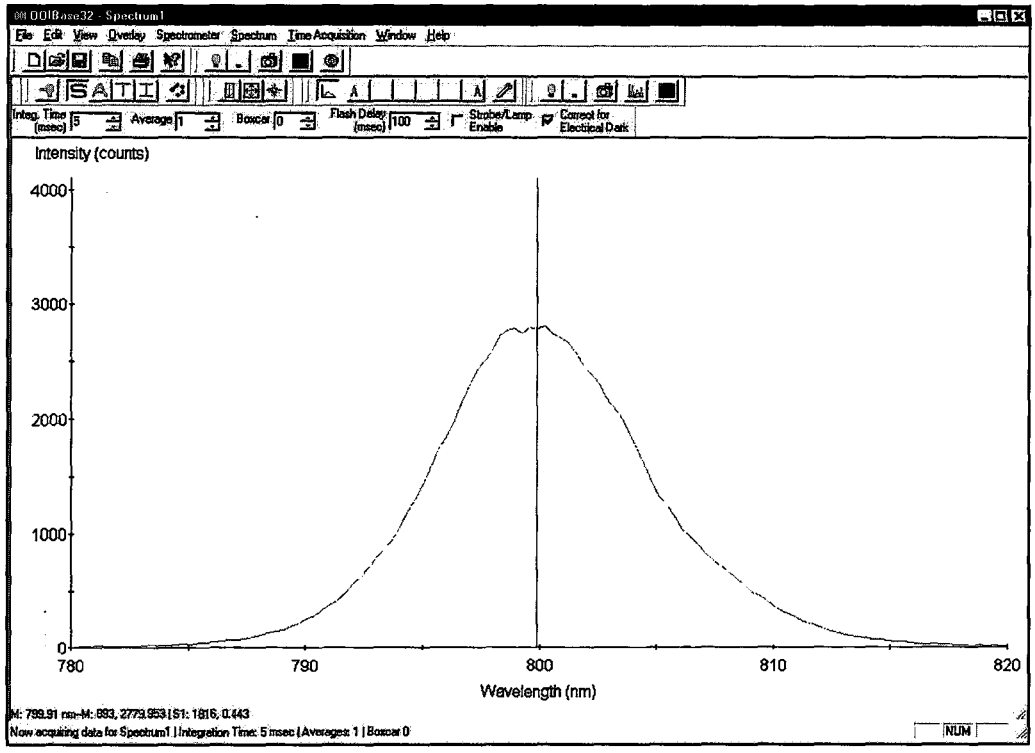

Figure 2-2: Image of the Ocean Optics PC2000 software window showing the output wavelength spectrum centered at an 800 nm with 10 nm FWHM bandwidth from the Ti:Sapphire oscillator.

2.3.3 Beam Profile

The laser beam has a Gaussian profile distribution. We can monitor the distribution of the beam using Beam Star OPHIR Software. Any clipping or fault in the beam path can be detected in the software. Figure 2-3 shows the laser beam profile from the CPA system that is taken with the OPHIR BeamStar silicon CCD camera placed behind the iris 2 (I2) in Figure 2-4. A good alignment of optical

components will lead to a concentric profile centered about the iris. The general beam profile can be viewed in the top-left corner of Figure 2-3. An ellipticity was detected on the almost concentric profile. The ellipticity phenomenon is caused by damaged or not well aligned optical components such as pockel cells or diffraction gratings in the regenerative amplifier. On the right-hand side of the window shows the Gaussian profile for vertical (top) and horizontal (bottom). The red lines are ideal Gaussian profiles whereas the white lines are actual beam traces that are approaching to ideal Gaussian profiles with some spiking. Some speckles are found in the beam profile image. The spiking and speckles are present from the existence of dust or impurities on the optical components and often in the detection optics itself.

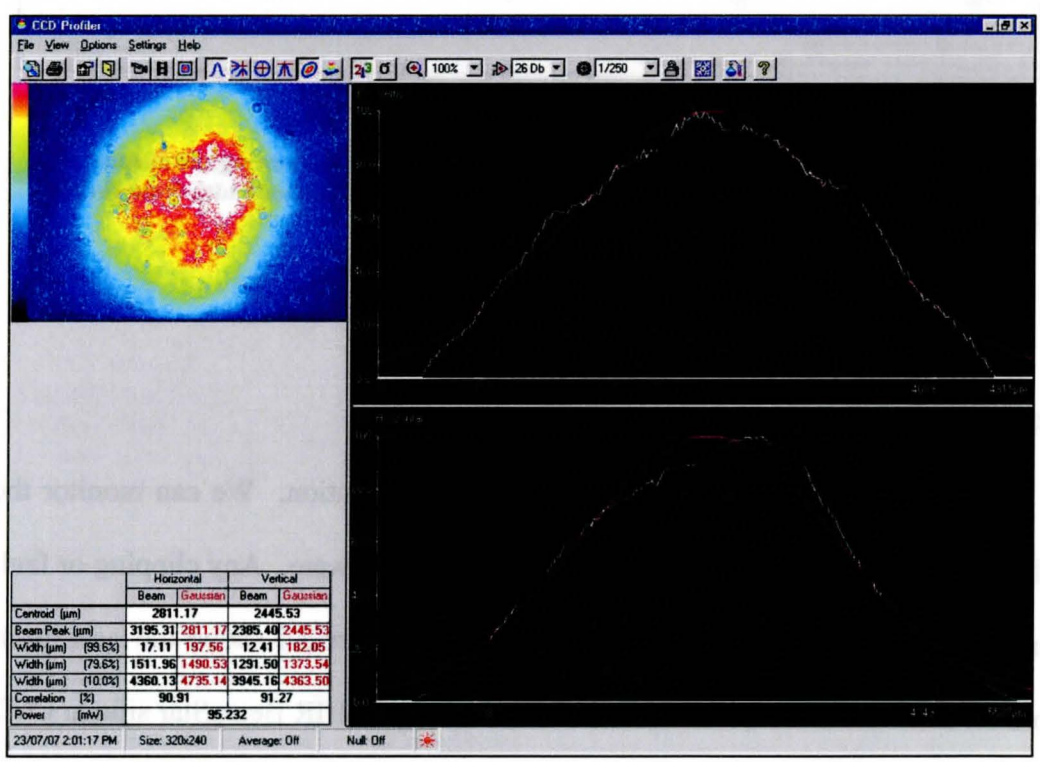

Figure 2-3: Image of beam profile window.

2.3.4 Laser Micromachining Setup

The femtosecond laser machining set-up is illustrated in Figure 2-4. The output from the amplifier (Chirped Pulsed Amplifier = CPA) was delivered to the ablation setup by some dielectric mirrors. Mirror M4 functions as a beam splitter which can select the output from the Spitfire beam. The beam from Spitfire is is reduced in size by a beam condenser which consists of an achromatic doublet lens (L1) and a plano-concave singlet lens (L2). The beam is size-reduced intentionally to avoid beam clipping on thin film polarizer (TFP), wave plates and some other small aperture optical equipments. After passing through the thin film polarizer, the dielectric mirrors M5 and M6 are used to align the beam through two irises I1 and I2 before entering the main part of the machining setup to ensure that the beam is straight. The energy of the laser is adjusted with a set of thin (1 mm) reflective neutral density (ND) filters. Those filters are mounted in two filter wheels to allow power adjustments in steps of 0.1 OD ($\frac{P_{out}}{P_{in}} = 10^{-O.D}$ where P_{out} is transmitted power and P_{in} is input power). The two filter wheels are mounted on custom-built rotation stages and the position of each wheel can be controlled manually or by a computer. A part of the laser beam is reflected into photodiode (PD) by pellicle beam splitter (PBS). The photodiode monitors the laser energy during experiments. A chopper is used to reduce the repetition rate from 1 kHz to 50 Hz, because the shutter needs 1-3 ms exposure (from open to close). A fast mechanical shutter, synchronized with the laser, is used to control

the number of pulses delivered to the sample. After the shutter, three mirrors are used (M7-M9) in order to direct beam from the top to the specimen chamber. The laser was focused on the sample by a Newport 5× microscope objective. A confocal imaging system and a CCD camera were used to monitor the machining process on-line. A piece of transparent material sample was placed inside a small vacuum chamber mounted on a computer controlled xyz translation stage with a maximum linear speed of 500 μm/s. The laser beam was delivered through a fused silica window cut perpendicular to the c-axis to avoid birefringence effects in the window Figure 2-4 illustrates the symbolic chart of femtosecond laser machining setup.

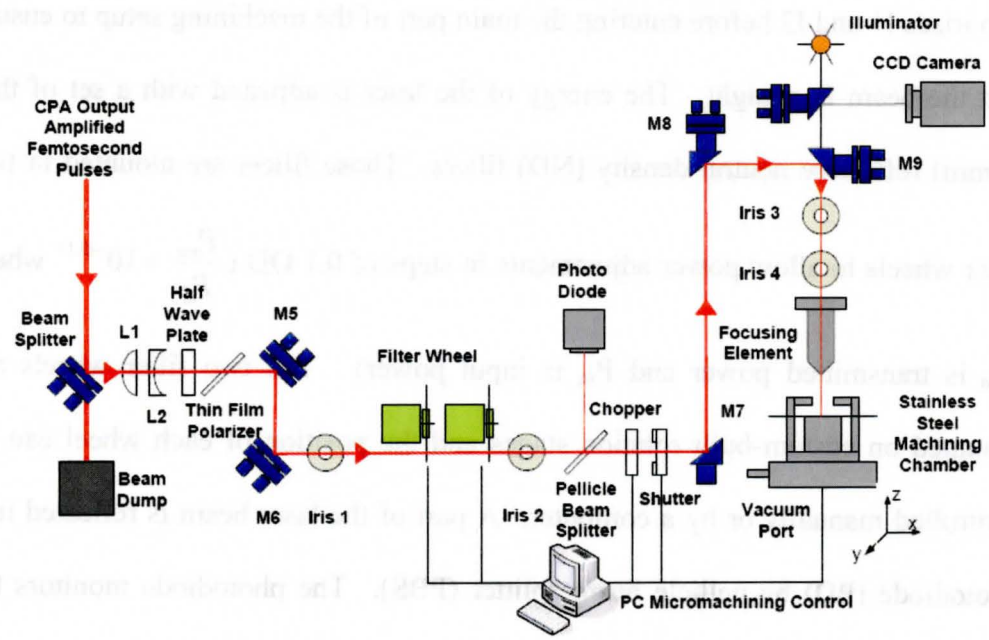

Figure 2-4: Symbolic chart of femtosecond laser machining setup (Adapted from [68]).

2.4 Time scale effects in laser material ablation

This section will compare the femtosecond (ultrashort) and nanosecond (long) regime. Some publications classified these further into femtosecond, picosecond, nanosecond, and millisecond (Continuous Wave) regimes. Few picoseconds still belong to ultrashort regime. However, this thesis will discuss femtosecond regime only.

2.4.1 Femtosecond regime

Figure 2-5 illustrates a schematic of femtosecond-pulse laser ablation. Assuming there are few free electrons in dielectric material, when a laser pulse hits the material, the laser energy is initially absorbed by those free electrons. If τ_e is the electron cooling time (1 ps); τ_i is the lattice heating time; and τ_l is the duration of laser pulse, the femtosecond regime can be stated with $\tau_l << \tau_e << \tau_i$, where laser pulse duration (τ_l) is much less then electron cooling time (τ_e). The absorbed energy heats the electrons instantly and is transferred strongly to positive lattice ions via electron-lattice coupling. When the intensity is high enough, which is the case in femtosecond laser pulse ablation, the same charge in lattice ions repulse each other and break up the bonds of lattice structure instantly without having time to transfer their energy to their neighboring lattice ions [19]. As a result, a direct solid-vapor (solid-plasma) transition can be achieved. Strong electron-phonon coupling causes rapid cooling of the hot electrons and thereby prevents long-range energy transport by electron diffusion, indicated by dashed

wavy arrow in Figure 2-5. The surrounding material stays undisturbed. With fs pulses, no vapor/plasma plume can develop during the pulse and ablation takes place only after the pulse. In materials where the excitation energy is rapidly transferred to the lattice, large stresses are built up and may result in explosive material ablation [71].

Short pulse duration does not have enough time to heat the materials to experience liquid phase because lattice heating is in order of few picoseconds, thus materials will experience a solid-plasma transition. The time required for actual material removal after lattice heating is about 10^{-10}-10^{-9} s [72]. Heat diffusion will be insignificant for such short time frame, the shockwave which induces mechanical stress is reduced [73]. The aforementioned advantages of femtosecond laser pulses allow precise processing pulse after pulse [74]. With femtoseconds laser pulses, materials also experience highly non-equilibrium states before ablation is accomplished. The Heat Affected Zone (HAZ) is also strongly reduced. Theoretically no collateral damage in the materials is expected. However our materials show differently where cracks, melting phase, and amorphization caused by rapid cooling on the surface and in the sub-surface of materials are observed. These phenomena are also observed in other materials such as silicon [29, 75], InP [76, 77] and GaP [27].

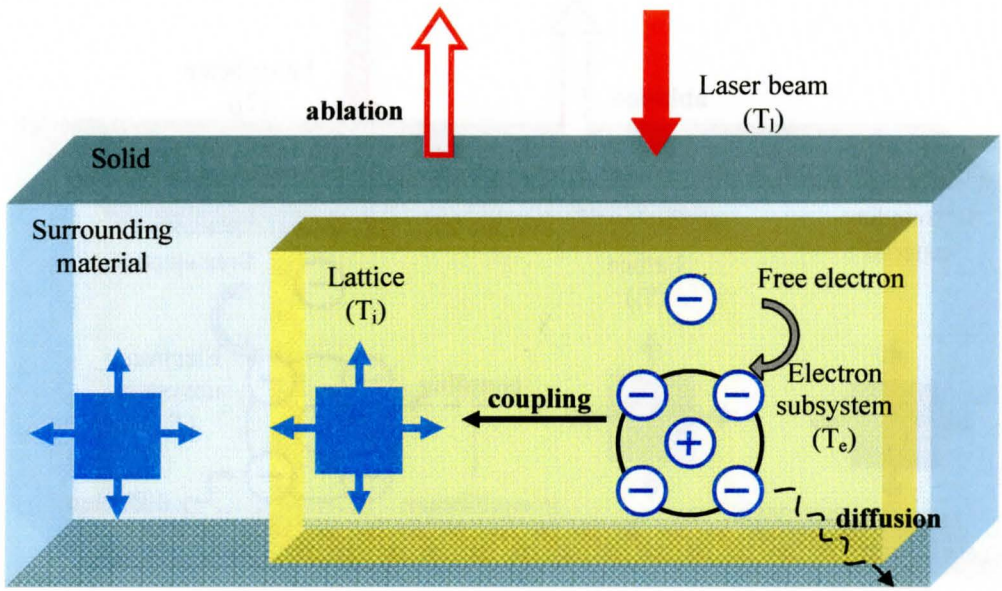

Figure 2-5: Schematic diagram of femtosecond-pulse laser ablation (Adapted from [74, 78]).

2.4.2 Nanosecond regime

In nanosecond regime, the condition can be explained as $\tau_l > 1$ ns $>> \tau_i >> \tau_e$. This duration is much longer than the electron-lattice energy coupling time. The schematic diagram of nanosecond-pulse laser ablation is illustrated in Figure 2-6. When a laser pulse hits the material, the laser energy is initially absorbed by free electrons. The absorbed laser energy has enough time to be transferred to the positive lattice ions through weakly electron-lattice coupling. In case of nanosecond pulse ablation, electron and lattice can reach thermal equilibrium. The laser energy heats the surface of materials into melting phase and then further to vaporization temperature.

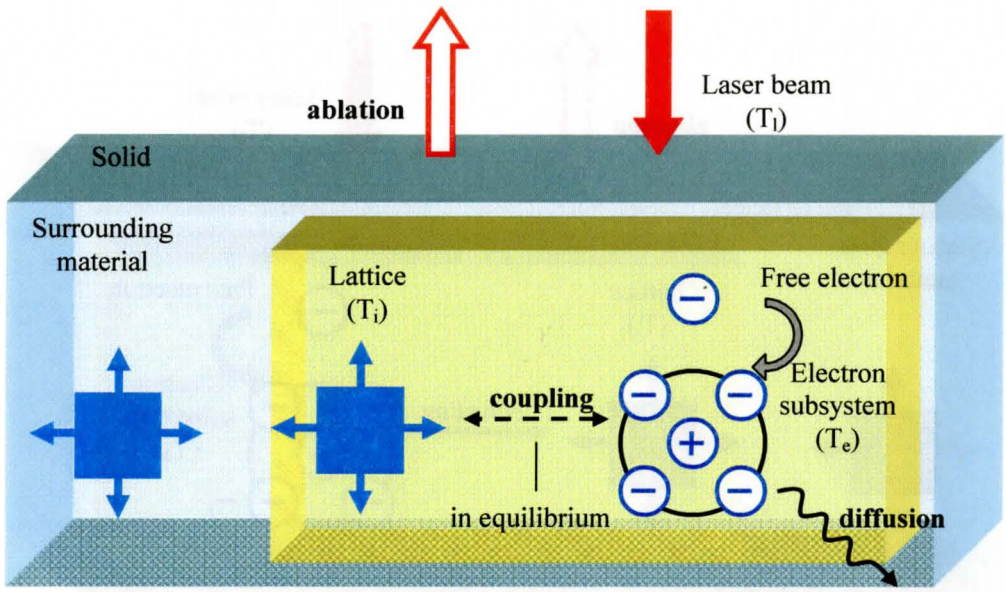

Figure 2-6: Schematic diagram of nanosecond-laser laser ablation (Adapted from [74, 78]).

The heat diffusion in this regime is very large because of the energy dissipation to ambient material. The main material removal mechanism is from melting phenomena. The complete model of femtosecond and nanosecond pulse laser ablation of solids were well described Yao et al [19, 74] and Chichkov et al [74].

2.5 Mechanism of Ultrashort Pulse Laser Ablation

2.5.1 Absorption and Desorption

Laser induced desorption is described with a phenomenon of particle ejection without any detectable mesoscopic modification of surface composition

or structure. In contrast, laser ablation is a sputtering process in which material removal rates typically exceed one-tenth monolayer per pulse. Laser ablation modified the surface in structural and/or composition at mesoscopic length scales. Laser ablation process involved the formation of an ablation plume or plasma [17].

However laser-induced desorption and laser ablation are not entirely separate phenomena. Laser-induced desorption is a conditioning surface process which may lead to material modifications that affect subsequent laser ablation. Additionally, laser ablation does not need massive and catastrophic destruction of a surface. Laser ablation is a well-controlled and repeatable method of injecting target material into the gas phase. It is probably more correct to view desorption and ablation as two points on a continuum of phenomena seen in laser interactions with material surfaces, beginning with desorption and ending at multiphoton and avalanche ionization on the surfaces [17].

2.5.2 Dielectric Breakdown

Note that we are working in the ultrashort (femtosecond) pulse regime. Femtosecond pulse laser interacts with materials very differently from longer pulse lasers. For comparison, in the longer (nanosecond or Continuous Wave) pulse regime, the breakdown of the dielectric materials strongly depends on the number of free electrons. The more free electrons, the more severe the damage on the materials. As mentioned in the previous section, we have shown by the

simple calculation in section 1.1 that an average power laser of 20 mW, 1 kHz repetition rate, and 200 fs pulse duration will yield to peak intensity of $\sim 15.10^{13}$ W/cm^2. So we are working in the range of gigawatt- and terawatt-per square centimeter. In such a high intensity range, even the valence electrons that are bounded to parent atoms can be knocked free.

For opaque materials, linear absorption is the main absorption mechanism at long pulse duration, low intensity and nonlinear absoption may become significant at ultrashort pulse duration with high intensity. For transparent materials, absorption has to come from nonlinear processes through ultrashort laser-induced optical breakdown. The significant nonlinear absorption which causes optical breakdown at the gigawatt- and terawatt-per-square centimeter intensities are avalanche and multiphoton ionization. [19, 37].

Transparent dielectric materials have very few free electrons. The bound electrons are tightly localized and can only oscillate weakly. On the contrary, the free electrons, which are unbound, can oscillate strongly once they are in the laser field. Avalanche ionization process is initiated with one free electron colliding with surrounding atoms, and if the laser field is intense enough it will break off more free electrons and create additional free electrons at an exponential rate[37]. Avalanche ionization is illustrated in the Figure 2-7.

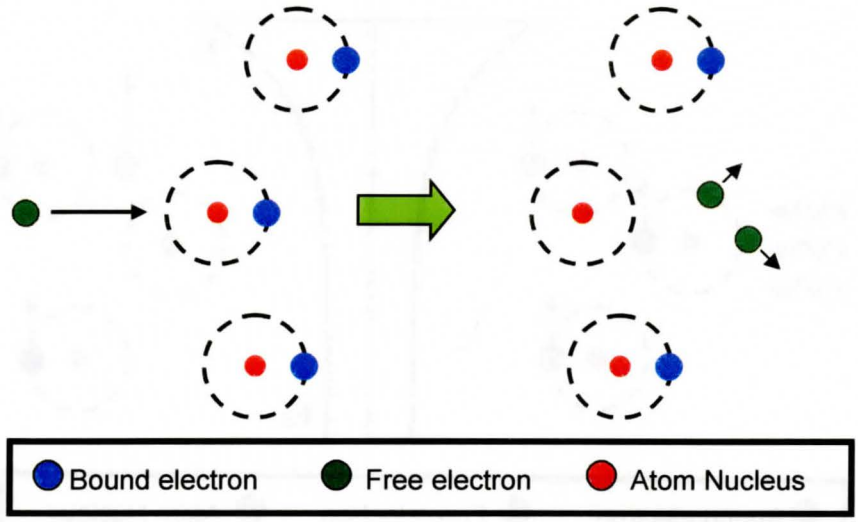

Figure 2-7: Schematic diagram of avalanche ionization (Adapted from [37]).

Again, in the ultrashort-pulse laser regime, the laser field is very high. Bound electrons of the dielectric transparent materials can be ionized directly through a process called multiphoton ionization. A bound electron can be excited from its valence band (E_0) to the conduction band (E_i) by absorbing two-or more photons simultaneously in the laser pulse. Figure 2-8 is the illustration of multiphoton ionization.

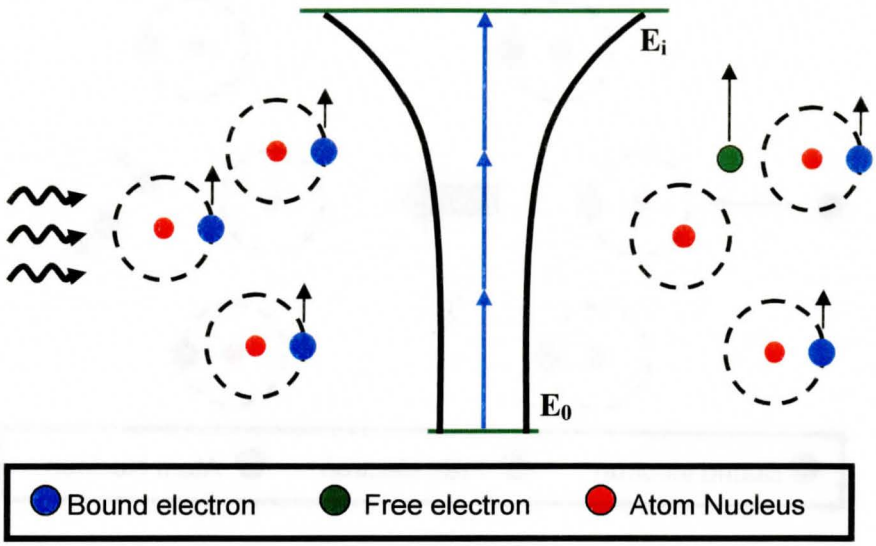

Figure 2-8: Schematic diagram of multiphoton ionization (Adapted from [37]).

Lasers have been applied in different applications in materials processing depending on the interaction time (pulse duration) of the laser beam-materials and the power density, such as welding, cutting, annealing, surface modification, synthesis, etc. Figure 2-9 and Figure 2-10 show the diagram of power density versus interaction time or pulse duration and different applications of laser In this research, we were doing laser micromachining in femtosecond regime with high power density Specifically we use Ti:sapphire with 1 kHz repetition rate, 150-200 fs pulse duration, Newport–5× microscope objective, yielding to spot sizes (beam radius at $1/e^2$) on the dielectrics sample surface of ≈5 μm centered at an 800 nm wavelength. We are in the region where avalanche and multiphoton

ionization (MPI), no liquid phase and negligible heat diffusion occurs, on the top-left area of the diagram.

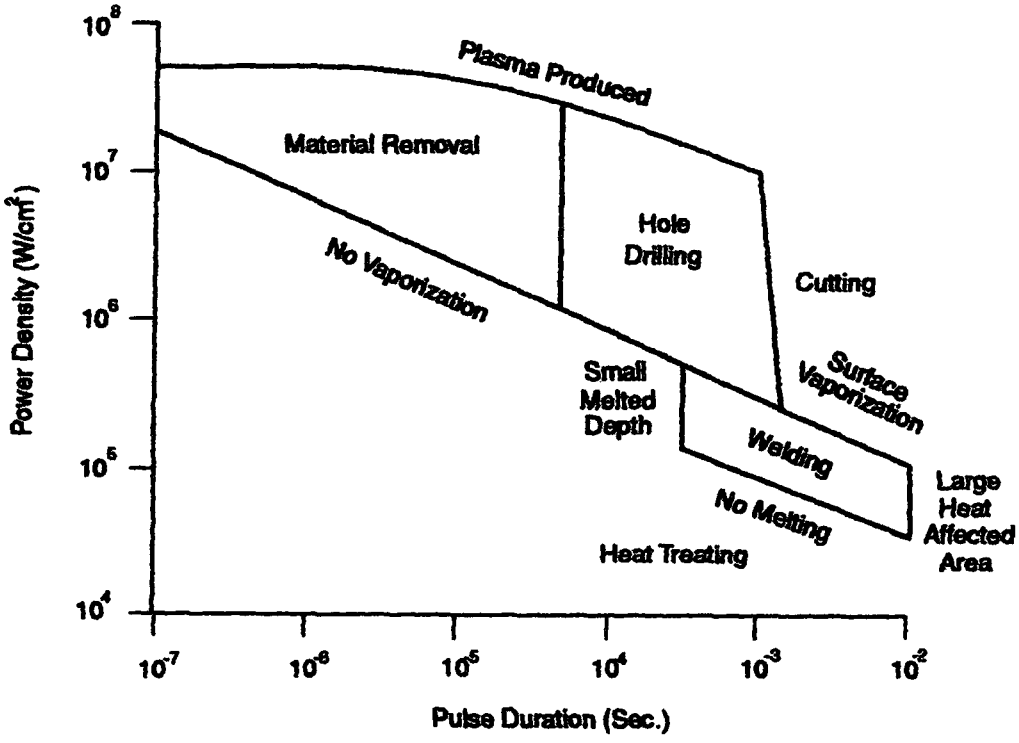

Figure 2-9: Graph of power density vs pulse duration, the ordinate represents the pulse duration for a pulsed laser or the time that the beam dwells on a spot for a continuous laser (Graph from [79]).

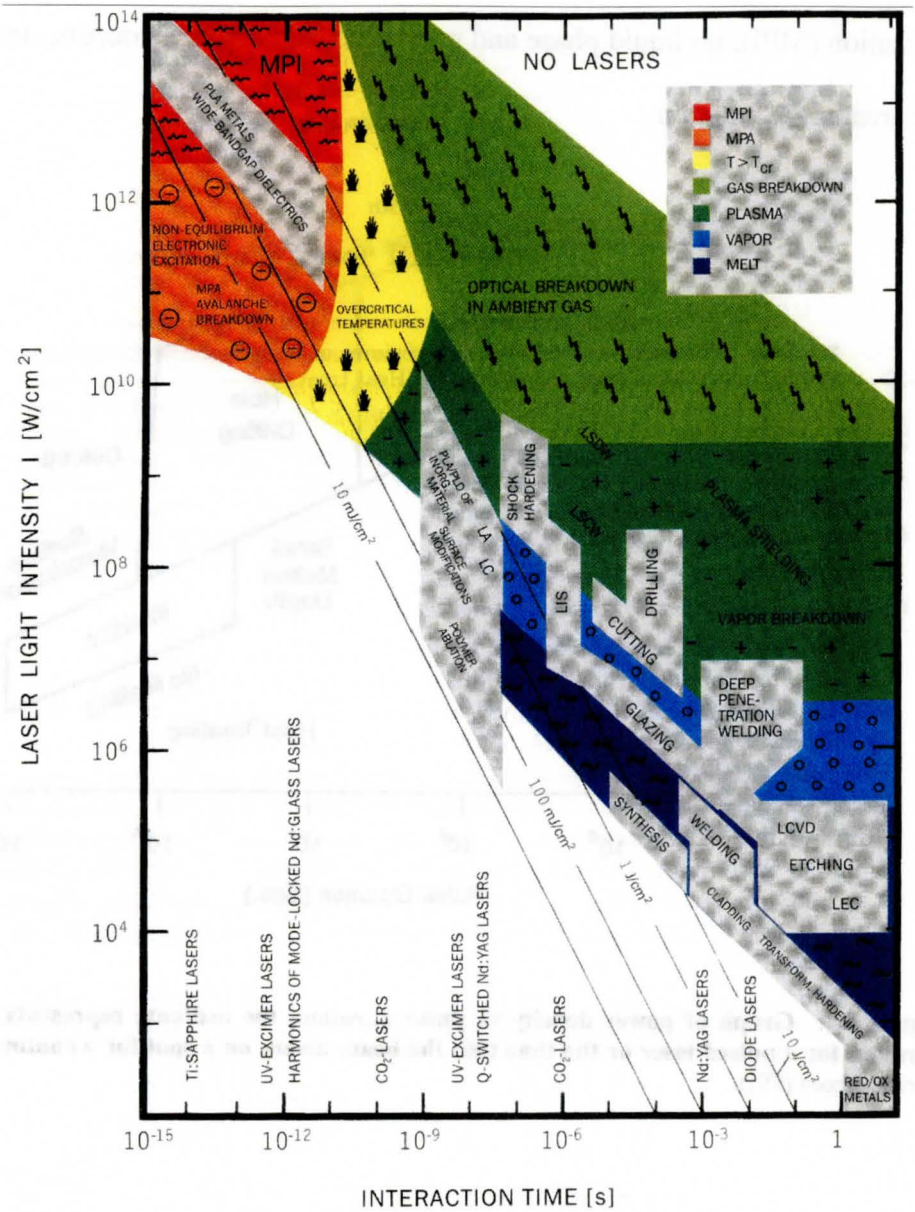

Figure 2-10: Applications of lasers in materials processing. PLA/PLD: pulsed-laser ablation/deposition. Surface modifications include laser-induced oxidation/nitridation of metals, surface doping, etc. LA: laser annealing, LC: laser cleaning, LIS: laser-induced isotope separation/IR-laser photochemistry. MPA/MPI:multiphoton absorption/ionization. LSDW/LSCW: laser supported detonation/combustion waves. LCVD: laser-induced CVD, lEC: laser-induced electrochemical plating/etching, RED/OX: long pulse or CW CO2-laser induced reduction/oxidation (Graph from [71]).

2.5.3 Gaussian Beam

The laser beam used in this research has Gaussian beam distribution as depicted in Figure 2-11. 5× and 50× microscope objectives are used to focus the laser beam. They both have working distance of 2.54 cm (1 inch).

For a Gaussian beam, the spatial fluence profile $\Phi(r)$ is given by [71]

$$\Phi(r) = \Phi_0 e^{-\frac{2r^2}{\omega_0^2}} \qquad \textbf{Equation 2-1}$$

where r represents the distance from the beam axis, ω_0 is the $1/e^2$ radius of the field distribution, and Φ_0 represents the maximum laser fluence at the cross-sectional surface.

The spatial variation of the phase of the wave is measured with respect to that of an infinite plane wave. In this formula, ω_0 represents the beam radius (that is, the value of ω at the plane z=0) [80]

$$\Theta(z) = -\arctan(\lambda z / \pi\omega_0^2) \qquad \textbf{Equation 2-2}$$

The wavelength of the radiation in the medium is depicted as follows:

$$\lambda = 2\pi c / n\omega \qquad \textbf{Equation 2-3}$$

In the theoretical work, it is convenient to represent the Gaussian beam in the more compact form in a dimensionless longitudinal coordinate defined in terms of the confocal parameter. The confocal parameter is the measure of the longitudinal extent of the focal region of the Gaussian laser beam [79, 80], which illustrated in Figure 2-11 (c)

$$b = 2\pi\omega_0^2 / \lambda$$ **Equation 2-4**

While

$$z_R = d_f = \pm\frac{\pi\omega_0^2}{\lambda}$$ **Equation 2-5**

is known as the Rayleigh range, which is denoted by z_R. The Rayleigh range is a measure of the length of the waist region over which the spot size does not change significantly. For smaller Rayleigh range, the growth of the beam radius from the waist is more rapid. In practical applications, care must be taken to maintain an optimum Rayleigh range. The changes in Rayleigh range modify the penetration depth of the laser beam into the workpiece and affect the quality and repeatability of the process [79].

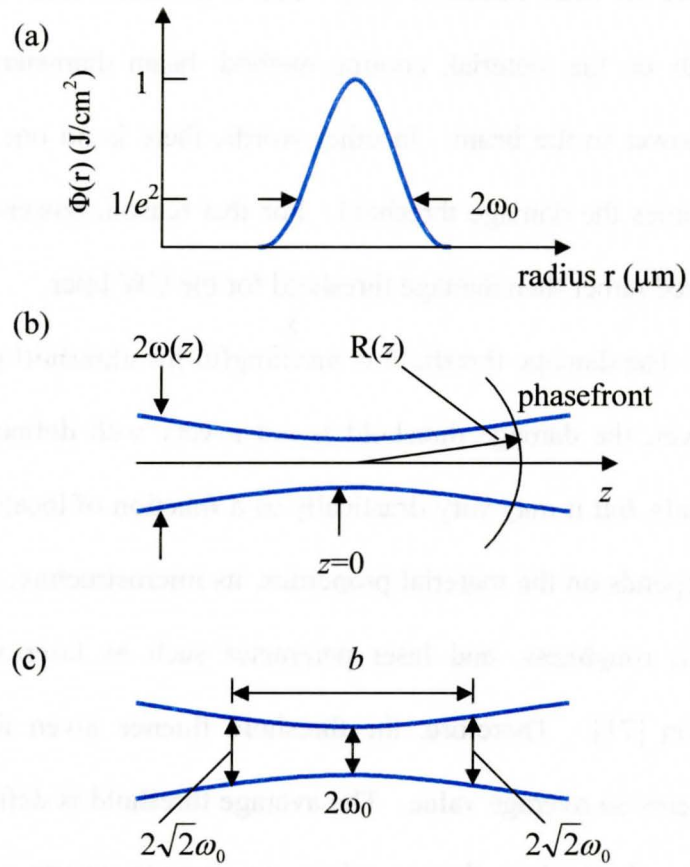

Figure 2-11: (a) Spatial fluence profile of a Gaussian beam (b) Variation of the beam radius ω and wavefront radius of curvature R with position *z* (c) Relation between the beam waist radius and the confocal parameter *b* (Adapted from [80]).

2.5.4 The damage threshold, Φ_{th}

The determination of the damage threshold is the most interesting property for the practical purpose of the characterization of optical components and materials. The damage threshold is a property of the crystal to withstand the laser radiation without damage or the point at which optics begin to fail due to

exposure to laser radiation [79]. For CW laser beams the damage threshold depends on the material, cooling method, beam diameter, mode structure, and total power in the beam. In other words, there is no one absolute number that determines the damage threshold. For that reason, power-handling capability is preferred rather than damage threshold for the CW laser.

The damage threshold is meaningful for ultrashort pulse laser processing. However, the damage threshold is not a very well defined quantity for optical materials, but it may vary drastically as a function of location on the sample [79] and depends on the material properties, its microstructure, physical and chemical defects, roughness, and laser parameter such as laser wavelength and pulse duration [71]. Therefore, the threshold fluence given for a sample normally represents an average value. The average threshold is defined as the mean value between the highest fluence where no damage occurs and the lowest fluence where damage is observed. In this study, we tend to extrapolate a curve to obtain the damage threshold of materials. Another important parameter for damage testing is how to perform the laser irradiation; i.e. whether single pulse or multiple pulses are applied. For multiple pulses experiments, the damage threshold also differs for a train of pulses at a constant fluence or increasing fluence. The earlier method is significant for the study of incubation phenomena whereas the latter include surface cleaning and conditioning effects [17].

Φ_{th} decreases with an increasing absoption coefficient, irrespective of whether this is related to a decrease in laser wavelength, the addition of dopants,

or to the generation of defects. A decrease of Φ_{th} with increasing effective absorption coefficient is expected for both thermal and non-thermal ablation mechanisms, because the excitation energy will be localized in a smaller volume [71]. Specifically, defects may become the major source of absorption and thus give a lateral spatial distribution to absorption. In such case, a cleaved surface always has much higher ablation threshold than a cut surface due to the greater defect density of the cut surface [17].

The effective absorption coefficient can be described by [71]:

$$\alpha = \alpha_0 + \sigma_i N_i + \alpha_D(N_l) + \alpha^{NL} \qquad \textbf{Equation 2-6}$$

Here α_0 denotes the linear temperature-dependent absorption coefficient of the pure material. The second term, $\sigma_i N_i$, describes the effect of light-absorbing impurities/dopants, where N_i is the number of impurity/dopant atoms or molecules per unit volume. The third term, $\alpha_D(N_l)$ is radiation-induced defects (incubation centers). α_D is a function of laser intensity, I, and it saturates after a certain number of laser pulses, N_l. With transient defects, α_D depends on the laser-pulse repetition rate. The last term, $\alpha^{NL} \equiv \alpha(I)$ stands for multiphoton (nonlinear optical) absorption processes. With very high laser-light intensities, when self-induced transparency, thermal runaway, avalanche ionization, etc., become important [71].

The maximum fluence and the pulse energy E_{pulse} are equally related by

$$\Phi_0 = \frac{2E_{pulse}}{\pi\omega_0^2}$$ **Equation 2-7**

2.5.5 Spot Size Measurement

With a modification threshold fluence Φ_{th}, the diameter D of an modified crater is also related to the maximum fluence [81]

$$D^2 = 2\omega_0^2 \ln\left(\frac{\Phi_0}{\Phi_{th}}\right)$$ **Equation 2-8**

From linear dependence of the maximum laser fluence and pulse energy in equation 2-7, we can verify the beam radius (spot size) and hence the threshold fluence from the squared diameter (D^2) versus the logarithm of the pulse energy (E_p). The slope of the plot is used to determine the beam radius (ω_0). It will be noticed the data points at higher fluences will not be linear anymore. It is caused by the intensity divergence from Gaussian distribution at the periphery of the beam. Thus, lower energy data points are accurate for the determination of beam radius in equation 2-8.

From the gradient of the plots, we will get the beam radius ω_0. After getting the beam radius, the pulse energy can be replaced by the maximum fluence of the beam using equation 2-7. The extrapolation of regression or linear fit from the plot to D^2 equal to zero yields the modification threshold fluence Φ_{th}.

The following paragraphs explain how to determine the diameter of the single pulse ablation experiments. Each material has specific behavior with

respect to femtosecond laser pulse. According to some literature about single pulse crater measurement [29, 82], we use term of modification threshold instead of ablation threshold. "Ablation" refers to the process that ejects material away from the original sample. "Modification" is preferably used as in all cases presented in this research. The crater diameter D was measured to the outermost periphery of visible modified irradiated area. The degree of circularity of the beam varies due to the adjustment variation of the laser or the beam optics from time to time.

Quartz

Single crystal α-quartz showed a splashy structure from the center to the periphery of the crater. The regions splattered from the irradiated area are occasionally reaching outward at an appreciable distance. Thus, the indistinct crater boundary makes it challenging to determine the real damage region on quartz. The D^2 method in quartz gives higher uncertainty in the measurements. As shown in Figure 2-12, the diameter of the crater was measured at the $1/e^2$ of the fluence distribution. If the beam profile is very circular, the crater will also be very circular too.

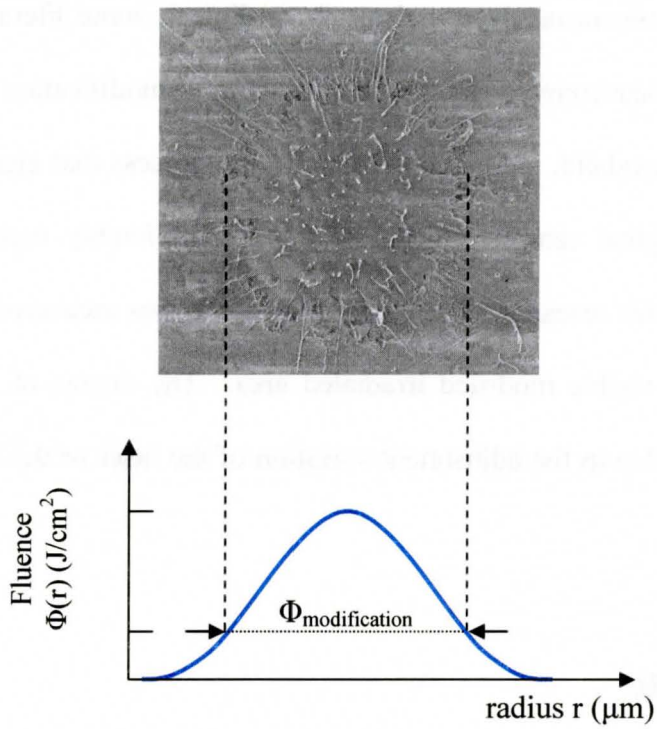

Figure 2-12: The determination of crater diameter on quartz.

Sapphire

Sapphire with the hardness of 9 Mohs, showed the different behavior from quartz. Splashed form of material was observed at the outermost crater Some cracks appear across the crater The measurement of the crater diameter was taken from end to end of the crater periphery and not necessarily included the splashed structure due to a more distinct boundary between damaged and undamaged regions. In the experiments, we obtained surface craters with an elliptical shape. In order to determine the diameter of each crater, we took the

average of the major axis ($2D_M$) and minor axis ($2D_m$) of the elliptical shaped crater.

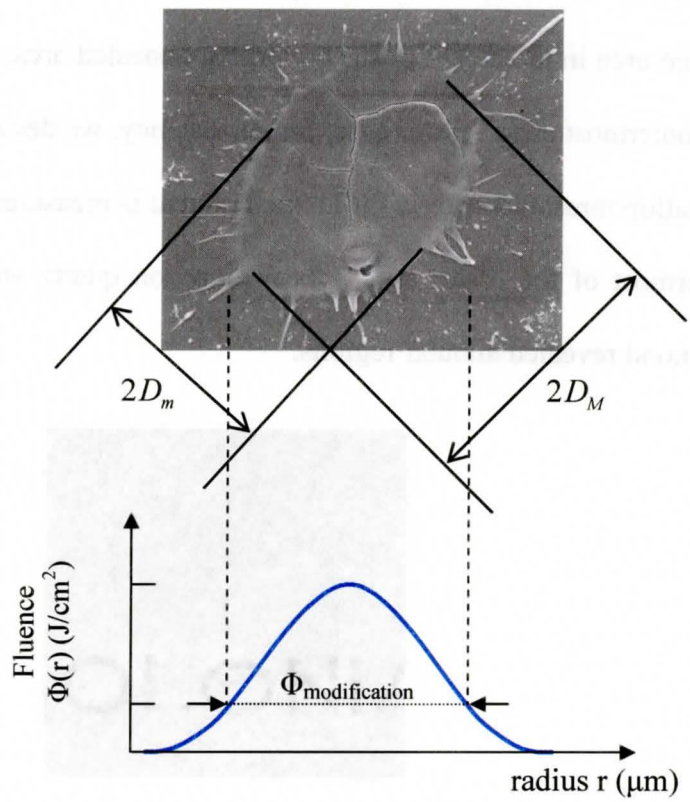

Figure 2-13: The determination of crater diameter on sapphire.

Diamond

Diamond, as the hardest natural material with 10 Mohs also revealed the specific behaviors under femtosecond laser irradiation in a single pulse ablation experiment. As presented in Figure 2-14, the crater introduced by a single pulse has a very clear boundary between the irradiated and not irradiated areas. The concentric areas on the crater are due to the different degree of the damage

introduced by the Gaussian laser beam. Bonse et al [29] and Tran et al [82] classified the irradiated area on silicon according to the physical processes during the modification with femtosecond laser pulses and their threshold fluences, such as the ablated area in the center of the crater, the annealed area, and the modified area at the outermost area. In our case, for consistency, we decided to keep using the modification threshold criteria for D^2 method that is measured from end to end of the outermost of the crater as had been done on quartz and sapphire, even though diamond revealed annular regions.

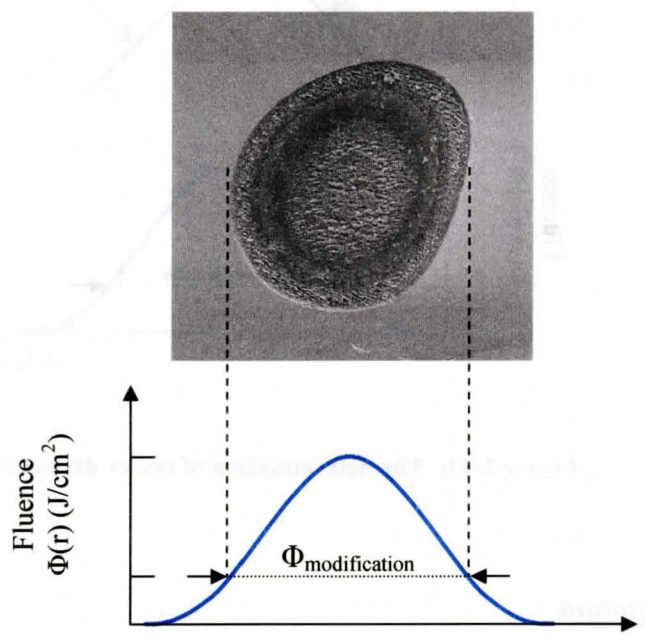

Figure 2-14: The determination of crater diameter on diamond.

2.5.6 Material Patterning and Damage

Femtosecond-pulse laser micromachining has been proved to be a powerful technique that offers precise and reproducible means of material patterning and processing. An optimum energy deposition in minimized volume and heat affected zone are made possible by a pulse duration that is shorter than the thermal diffusion time scale. Generally, the femtosecond-pulse laser induces modification or damage on materials that can be seen through the physical effects in the form of [17]:

1. Laser crater forms with single pulse and multiple pulses ablations on the same location. Typically a defined crater will develop after a single pulse ablation with fluence above the ablation threshold. A further increased number of pulses lead to different characteristic surface morphologies of the crater. The feature of the crater will vary from one material to another.
2. Laser Induced Periodic Surface Structures (LIPSS), also termed as ripple, occur from the interference of scattered light from a rough surface with the incident laser beam [83]. LIPPS will form after a number of pulses. It was firstly reported by Birnbaum on germanium sample [84]. As LIPSS is an interference phenomenon, the structures have a definite period related to the wavelength of the incident light. The spatial period of the interference pattern for reflected waves from the material surface is described as follows [71]:

$$\Lambda = \frac{\lambda}{1 \pm \sin(\theta)}$$ **Equation 2-9**

And the spatial period of the interference pattern for transmitted waves is then:

$$\Lambda = \frac{\lambda}{n \pm \sin(\theta)}$$ **Equation 2-10**

Where Λ is the spatial period of surface ripples, θ is the angle of incidence between the laser and the surface normal of the sample, n is the refractive index of the material and λ is the laser wavelength in the air.

Ripples formation can be also formed from surface electromagnetic waves (SEW), especially if one of the scattered waves is in resonance with an SEW. Simple calculations result in equations similar to Equation 2-9 and 2-10, except that n has to be substituted by refractive index of the SEW (n_{SEW}) where $n_{SEW} \approx 1$. The period of the ripples due to SEW for the incident electric field parallel to incident laser light can be written as [71]:

$$\Lambda \approx \frac{\lambda}{1 \pm \sin(\theta)}$$ **Equation 2-11**

And for the incident electric field perpendicular to incident laser light is given by

$$\Lambda = \frac{\lambda}{\cos(\theta)}$$ **Equation 2-12**

2.5.7 Self-focusing

Self-focusing of light occurs where an intense beam of light propagates through a nonlinear medium. For a Gaussian beam propagating in a medium with an index of refraction $n(I) = n_0 + n_2 I$, here we have taken an assumption that nonlinear refractive index n_2 is positive, and I is the incident light intensity As a result, the intense laser beam induces a refractive index variation within the material with a larger refractive index at the center of the beam than at its periphery The material behaves as if it were a positive lens, causing the beam to come to a focus within the material. Self-focusing of light is illustrated in Figure 2-15. Generally, one refers to self-action effects as effects in which a beam of light modifies its own propagation by means of the nonlinear response of a material medium.

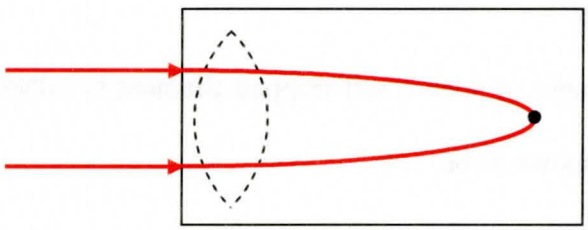

Figure 2-15: Schematic diagram of self-focusing of light [80].

Another self-action effect is the self-trapping of light, which is illustrated in Figure 2-16. In this process a beam of light propagates with a constant

diameter as a consequence of an exact balance between self-focussing and diffraction effects.

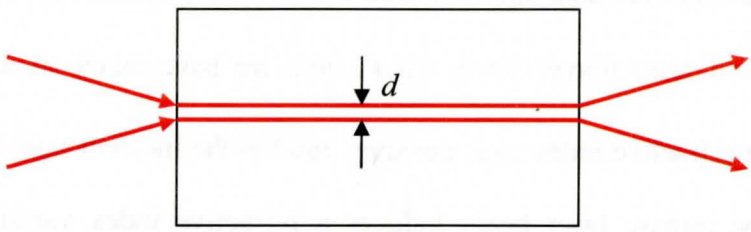

Figure 2-16: Schematic diagram of self-trapping of light [80].

Optical materials like quartz or sapphire have non-linear refractive indexes when sufficiently high intensity light is passing through. Self trapping will occur only if the intensity of the light within the filament is given by [80]

$$I = \frac{(0.61)^2 \lambda^2}{2n_2 n_0 d^2}$$ **Equation 2-13**

The diameter of such a self-trapped filament is related to the intensity of the light can be shown to be

$$d = \frac{0.61\lambda}{\sqrt{2n_0 n_2 I}}$$ **Equation 2-14**

The laser power contained in such a self-trapped filament in effect defines the critical power for self-focusing to occur, and is given by [80]

$$P_{crit} = \frac{\pi}{4} d^2 I = \frac{\pi (0.61)^2 \lambda^2}{8 n_0 n_2}$$ **Equation 2-15**

independent of the filament diameter. Note that the power, not the intensity, of the laser beam is crucial in determining whether self-focusing will occur. When the power P greatly exceeds the critical power P_{crit} and self-focusing does occur, the beam will usually break up into several filaments, each of which contains power P_{crit}.

2.5.8 Incubation effects

Defects generated by the laser radiation itself are commonly denoted as incubation centers. Among those are color center in ionic crystals, vacancies, broken bonds, molecular fragments, etc. Radiation-induced defects are of particular importance for the ablation behavior of wide bandgap materials and photon energies hv>Eg. Here, successive laser pulses increase the number of defects and thereby the absorption within the irradiated volume. The increase in energy absorption causes a decrease in Φ_{th}. Thus, Φ_{th} for multiple-pulse ablation is lower than for single-pulse ablation. In other words, if Φ is just below Φ_{th} for single-pulse ablation, ablation starts after a certain number of pulses. With further pulses, stationary conditions are obtained. Φ_{th} can also be reduced via defects generated by electron- or ion-beam irradiation [71].

Another characteristic feature is the decrease in Φ_{th} with pulse duration. With shorter pulses, the spatial dissipation of the excitation energy is reduced and Φ_{th} is reached at lower fluences. This observation can be related to a decrease in heat penetration depth and/or an increase in absorption coefficient due to

multiphoton excitation. Nonlinear excitations become important in particular for wide bandgap materials and/or optically strongly nonlinear materials exposed to picosecond or femtosecond laser pulses.

2.6 Characterization Methods

2.6.1 Optical Microscopy

Optical microscopy is used as a preliminary tool to observe the features of femtosecond laser machining work on each material, e.g. quartz, sapphire, and diamond. A general result of laser micromachining can be investigated in this step. Optical microscopy is found to be very useful, prompt, versatile and straightforward in sample preparation for further examination, such as Scanning Electron Microscopy (SEM) and Atomic Force Microscopy (AFM).

By examining the sample under the optical microscope, we have a better idea and expectation to see more details structure in particular region with SEM. Some dust or debris from the laser machining process can be cleaned before applying a conductive coating and examining under an SEM. The advantages of this light microscope are the Nomarski prism that is useful for imaging surface relief and the flexibility to select either reflective or transmission mode in order to see the features on the surface and in the sub-surface of transparent materials that sometimes are not possible with SEM.

2.6.2 Scanning Electron Microscopy

The Scanning Electron Microscope (SEM) is very widely used in industry and research to see surface structure or topography in almost all kinds of materials due to its wide range of magnification. The focused primary electron beam (PE) and specimen interaction is summarized in Figure 2-17 (a). The primary electron beam with energy range of 1-30 keV scans the specimen surface and creates an interaction volume. This interaction volume produces specific signals that are captured by different kinds of detectors. In Figure 2-17 (b), it is illustrated that there are two kinds of signals that are emitted from the sample. The first signal is from the electron and the second one is from the photon. The electron signals are classified into primary backscattered electrons and secondary electrons, specimen current and transmitted electron, while the photon signals are cathodoluminescence and X-ray photons. Characteristic X-rays give composition information; Auger electrons give composition information and are surface sensitive; primary backscattered electrons (BSE) give atomic number and topographical information; secondary electrons (SE) also give topographical information; cathodoluminescence (CL) give electrical information; the electric current flux on the sample or specimen current (SC) is used for the generation of an image, and in few occasions if the sample is thin enough, transmitted electrons (TE) can also be used for imaging.

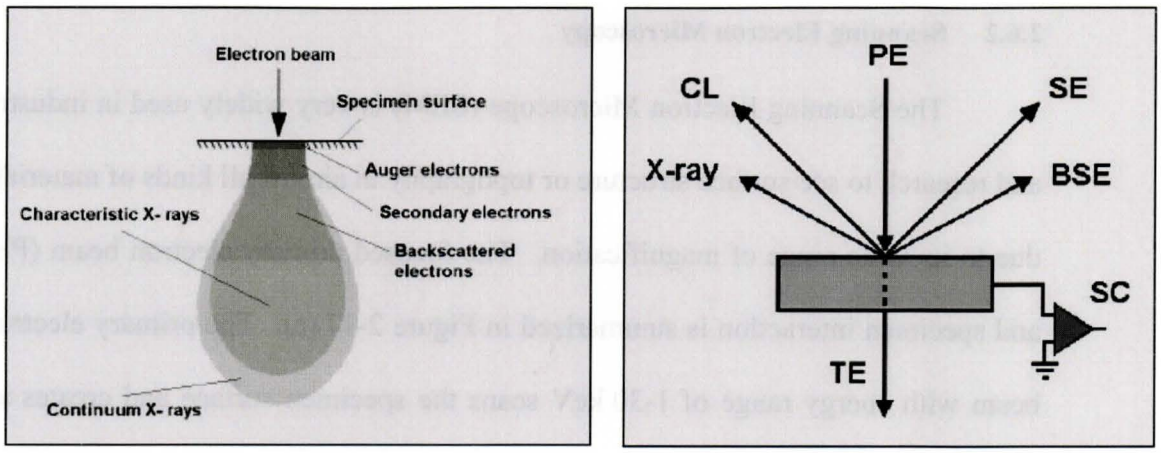

(a) (b)

Figure 2-17: Symbolic diagrams of (a) Interaction volume (b) Electron beam and specimen interaction (Diagrams from [85]).

In the characterization of the features from femtosecond laser machining, the main objective of using SEM is to obtain topographical information of specimen surface. So, secondary electron imaging was employed. Secondary electrons have low energy (less than 50 eV). They are generated by inelastic scattering of the primary electron beam on the core of the atom or on the electrons of the atomic shell of specimen. The signals from secondary electrons were collected by a secondary electron detector. Subsequently, the signals are converted to a voltage and amplified. The final image we recognize it as a topographical image, which is built from the number of electrons emitted from each spot on the sample.

Quartz, sapphire and diamond are insulators. The insulators should be coated with an ultrathin layer of conductive material to ground them. This was

performed to prevent the accumulation of electrons on the specimen surface during imaging. Platinum and carbon coatings are suitable for insulator specimens. Superior contrast can be obtained with these coatings.

In this project, most of the features introduced by laser were imaged with a SEM JEOL 7000F and the remainder with a SEM+FIB Zeiss NVision-40 Dual beam. In chapter 4, some micrographs were taken with two different detectors to image the laser features, i.e. In-Lens detector and Secondary Electron 2 (SE2) detector. For routine investigations, the SE2 or Everhardt-Thornley detector was extensively used. With the aim of imaging the surface structures on insulators, special procedures must be performed. Employing low acceleration voltage (about 2 keV) is the optimum way to view the surface topography with much less electron built-up effect.

In the following section, the advantages of the Everhardt-Thornley and In-lens detector will be discussed.

Everhardt-Thornley Detector

The SE2 or Everhardt-Thornley detector is mounted on the wall of the specimen chamber. Based on that reason it is also called the chamber detector. Its position cause lateral viewing of the specimen. The SE2 detector collects the signals from secondary electrons, including SE1, SE2, and SE3 and backscattered electrons.

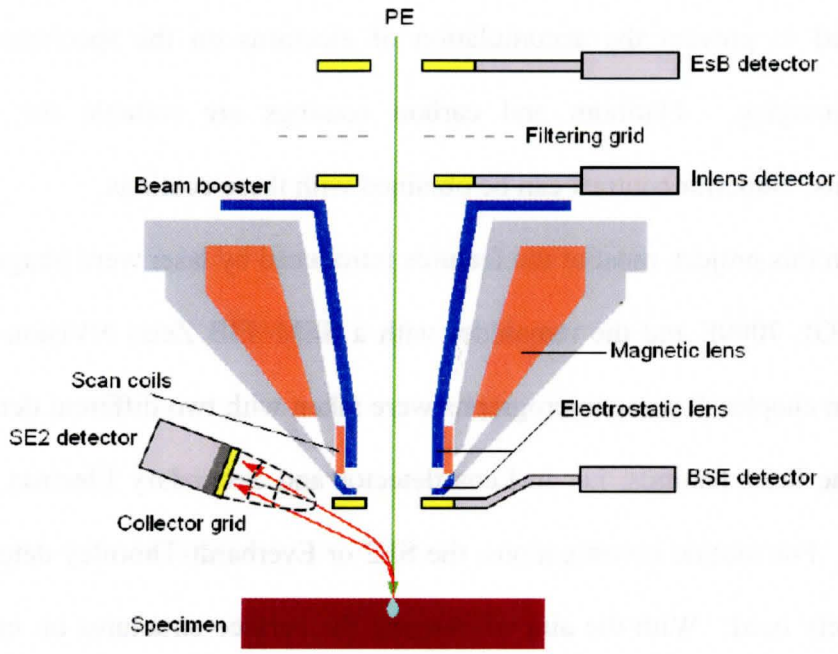

Figure 2-18: Symbolic diagram of SE2 or Everhardt-Thornley detector in SEM chamber (Diagram from [85]).

Secondary electrons are classified into three groups:

- SE1 are generated/leave the specimen surface directly in the spot centre
- SE2. are generated after multiple scattering and leave the surface at a greater distance from the spot centre
- SE3 are generated by BSE at places distant from the spot centre and do not contribute to indispensable image information

In-lens Detector

In-lens imaging using low acceleration voltage is capable of better surface structure visualization than the Everhardt-Thornley detector. Firstly, this is due to the higher efficiency of pure SE detection. The In-lens detector only collects signals from SE1 and SE2 electrons, while SE3 and backscattered electrons are insignificant. As a result, much more surface information can be obtained with the In-lens detector than the Everhardt-Thornley detector. A lower acceleration voltage gives a smaller interaction volume and penetration depth of electrons. Due to the smaller penetration depth of electrons, a higher portion of SE electrons produced in the top layers of the specimen surface contribute to the contrast.

A favorable reason to use low acceleration voltage is the minimization of electron charges on the sample surface. The In-lens detector lies inside the beam path of electrons and views the specimen right from above. The images generated from the In-lens detector appear flat due to the viewing direction which contains smaller topographic contrast [85].

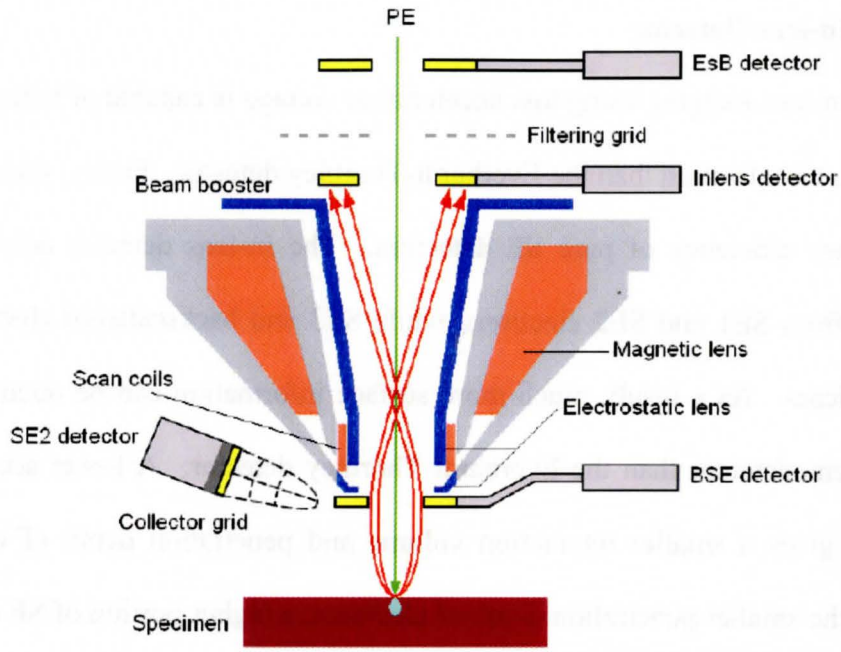

Figure 2-19: Symbolic diagram of In-lens detector in SEM chamber (Diagram from [85]).

Scanning Electron Microscopy (SEM) was used heavily to investigate all the detailed features of the laser machining. For single pulse ablation experiments, every single crater was imaged to get qualitative and quantitative information. Qualitative information was obtained from the topography of single pulse ablation, while quantitative information was obtained for the diameter of each crater to verify the spot size ω_0 and the single pulse threshold from from D^2 method. We also imaged and measured craters from multiple pulses ablations experiments. The continuous lines created by translated laser beam on the surface of materials were imaged to acquire the width and specific structure. The sub-surface lines cannot be imaged from the top with the SEM because of the depth

limitation of electrons. The only information that can be obtained is from the cross-section of the continuous lines; whereby we can find the position of irradiated area with respect to the focus of laser beam.

2.6.3 Atomic Force Microscopy

Atomic Force Microscopy (AFM) is one of the non-destructive essential instruments for surface imaging and characterizations. The AFM can profile any rigid surfaces. In this research, the AFM is employed to examine rough surfaces produced by a laser beam, such as craters and Laser Induced Periodic Surface Structures. The ability of AFM to provide topographic contrast and quantitative height information, places AFM different from SEM. In addition, AFM is able to work on non-conductive materials. The sample preparation method becomes relatively easy because a conductive coating is not required. Compared to cross-sectional Transmission Electron Microscopy, 3D AFM images gives more surface information without expensive sample preparation [86]. Figure 2-20 shows symbolic diagram of Atomic Force Microscope.

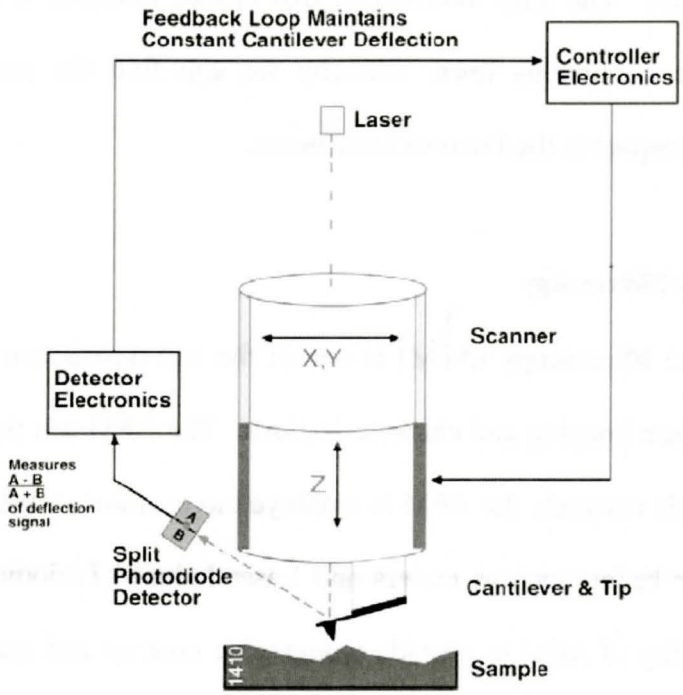

Figure 2-20: Symbolic diagram of Atomic Force Microscope (Diagram from [87]).

Contact mode AFM operates by scanning a tip mounted at almost the very end of a small V-shaped cantilever over the sample surface. The change in cantilever deflection is recorded with a split photodiode detector. The tip contacts the surface through its force interaction with sample surface. A feedback loop adjusts the height of the sample to maintain a constant deflection between the cantilever and the sample by vertically moving the piezoelectric scanner at each (x,y) data point. By maintaining a constant cantilever deflection, the force between the tip and the sample remains constant [87, 88]

The force is calculated from Hooke's Law : $F = -kx$ where: F=force, k=spring constant, x=cantilever deflection. Spring constants usually range from 0.01 to 1.0 N/m, resulting in forces ranging from nN to μN in an ambient atmosphere. The distance the scanner moves vertically at each (x,y) data point is stored by the computer to form the topographic image of the sample surface. Operation can occur in ambient and liquid environments [87]

The advantages of contact mode AFM are :

- High speed scanning [87].
- The only AFM technique with lower mechanical noise that yield atomic resolution images [86, 87].
- Rough surface samples with significant changes in vertical topography can occasionally be scanned more straightforwardly in contact mode. [87].

The drawbacks of AFM contact mode are [87]:

- Lateral forces can misrepresent features in the image.
- The forces perpendicular to the tip-sample interaction can be high in air due to capillary forces from the adsorbed fluid layer on the sample surface.
- The combination of lateral forces and high normal forces can result in reduced spatial resolution and may damage soft samples as a result of scraping between the tip and sample.

2.6.4 Focused Ion Beam

Focused Ion Beam (FIB) is a technique to investigate very specific site of the sample. At the Canadian Center Electron Microscopy laboratory, we have the NVision-40 Dual Beam console. Dual beam refers to an ion beam and an electron beam.

Gallium ions (Ga^+) originate from a liquid Gallium metal in contact with heated Tungsten needle (Wo). Liquid Ga wets the Wo needle, the high electric field induced by the Wo needle (greater than 10^8 volts per cm) will cause ionization and emission from Ga atom. Ga^+ accelerated at 30 keV and focused by electrostatic lenses in FIB etches the sample [89]. This is used to mill away the defined area of sample surface in order to make a clean hole or cross section. Besides milling, the FIB can also deposit particular material onto a sample surface. The precision of milling and depositing is in the micron scale. The FIB machine is equipped with gases such as H_2O and XeF_2. These gases are used to enhance the milling or depositing rate [90, 91].

When investigating a sample, the electron beam is used to image and the ion beam is used to mill or deposit onto specific area. The benefit of the FIB is the capability to prepare a very specific location of the sample without damaging the remaining area. The FIB is already extensively useful to prepare cross-section TEM samples for ultrahard materials that are impossible to prepare by conventional methods. The drawback of FIB is surface damage [91] and

implantation of Ga^+ onto the specimen. The ions can amorphize a few tens nanometers thickness of the specimen [91].

3 Experimental Techniques and Procedures

This chapter provides details on the experimental techniques which have been used in this work. The experiments are divided into three main activities, firstly those related to sample preparation; secondly, the various femtosecond laser machining on the three different materials, quartz, sapphire and diamond; and finally the characterization of features induced by the femtosecond laser machining.

Five different experiments were performed with femtosecond laser machining. These were single pulse ablation used for spot size and single pulse modification threshold determination, plural pulse ablation surfaces ($2 \leq N \leq 10$), multiple pulse ablation on surfaces ($10 < N \leq 100$), continuous surface lines and sub-surface continuous lines irradiation.

The entire femtosecond laser machining experiments were performed at the Brockhouse Institute for Materials Research (BIMR) while all the investigations and characterizations activities of laser machining were completed at Canadian Center for Electron Microscopy (CCEM). Both laboratories are at McMaster University.

From one experiment to another, the conditions of the laser were not exactly the same. In the pulse compression, we could not achieve the exact pulse duration. It will be noticed that the pulse duration will change from time to time in the range of 140-200 fs. Such pulse duration differences will not cause significant differences to the feature of laser ablation. All the experiments were performed with a Ti:Sapphire at 1 kHz repetition rate, centered at 800 nm in every experiment. The variable parameter was the average power to machine the samples that directly contributed to the pulse energy. These experiments used a 5× microscope objective for micromachining on the surface and a 50× microscope objective for irradiation inside the bulk.

The beam parameter was also not perfectly constant. The laser beam has a Gaussian distribution, however it will be noticed in the feature of craters which imperfectly symmetrical along x- and y-axis profile. The laser and transport optics should be adjusted to achieve the ideal beam profile and the flatness of the sample itself or mounting should be taken into consideration. The humidity and temperature of the laboratory, day to day positioning variations also affect to the stability of the laser.

3.1 Sample Preparation

3.1.1 Prior Femtosecond Laser Micromachining

Some samples were a few centimeters in size. In order to make a smaller sample, some steps of mechanical machining and surface preparation were performed. These preparations were done for quartz and sapphire. The quartz specimen was received in a hollow cylinder shape and a part of sapphire sample was received in 1 inch diameter window. Diamond samples were received in 2 mm diameter windows which did not need surface preparations.

Quartz

The pure quartz used here was provided by ComDev with hollow cylinder shape 1 inch in diameter. In order to carry out the micromachining experiment, the bulk quartz sample needed to be cut into thinner slices perpendicular to cylinder axis and some sequences of surface preparations. The sample preparation method included the following:

1. The sample cutting process into slices was done with the diamond saw at low speed. Water is employed as a lubricant and to release the heat introduced by friction of the diamond saw and the quartz sample. Quartz has 7 Mohs hardness and it is very brittle, therefore it is easy to induce crack in mechanical machining. One slice of quartz sample has thickness approximately 1.5 mm.

2. Course grinding was carried out with an Accutom Struers to prepare thinning section. The cutting process will result very rough and not flat surface. This machine is semi-automatic hence we can control the thickness of material that has been ground away and maintain the flatness of the sample.
3. Polishing the thin sample surfaces was performed with Techprep™ ALLIED (Multi-Prep) machine. The Multi-Prep machine is also semi-automatic where we can introduce specific pressure required to polish the sample. 8 inches diamond lapping films with particle size of 30, 15, 9, 6, and 3 μm together with water were used to polish the sample surfaces, continued with 1 and 0.5 μm particle sized diamond lapping film with Green Lube™ Diamond extender as a lubricant. The Multi-Prep machine has two micrometers on the left- and right-hand side to adjust the horizontal flatness of the surface that will be polished. In this case, the flatness is the main concern of preparing micromachining and cross-section SEM sample.
4. Final polishing was carried out also with Multi-Prep machine. For this step, the diamond lapping film is replaced with final polishing carpet. This process is using silica powder with particle size of 0.02 μm and water to get rid fine scratches from previous polishing step.

5. Surface preparation was performed for both side of thin sample. After the smooth surfaces are achieved, the sample is ready for micromachining and SEM characterization.

Sapphire

C-oriented sapphire window specimens were provided by Crystal System with dimensions of 500 μm thickness and 1 inch diameter. Sapphire with 9 Mohs is harder than quartz and was challenging to cut. The diamond saw that was used to cut quartz could not reproduce flat and relatively free-crack surfaces. Sapphire cutting was done with the automatic cutting machine Struers Accutom-50, at pre-set feed speed and actual feed speed of 0.005 mm/s.

In a certain series of experiments, the cross-sectional investigation was performed, such as surface lines micromachining and micromachining inside the bulk. Such investigation required a flat and a defect-free surface that usually can be obtained by cleaving. Sapphire has rhombohedral crystal structure which does not have a slip or cleaving plane [20, 92, 93]. However, Sink in his thesis [93] cleaved sapphire along the a-plane $<11\bar{2}0>$ successfully which needed a prior the a-plane thinning process until 70-100 μm to give reliable cleaving plane. The dimension and geometry of the sapphire sample used in this experiment is not possible to be thinned down into such a thickness. Based on the facts above, cleaving sapphire could not be achieved. Thus, a cross-sectional plane was

prepared with cutting using a diamond saw. Cracking was not avoidable even with low speed cutting.

3.1.2 Prior Scanning Electron Microscopy

Quartz, sapphire and diamond are dielectric materials. Under Scanning Electron Microscopy (SEM), electron beam charging of these samples is unavoidable. In order to be able to examine the samples with electron microscopy, coating surface with conductive materials is important. Gold coating is not suitable because the size of gold particles is too big. The gold particles can be seen under high magnification and may cover the original fine features that are induced by femtosecond laser machining. In addition, the gold sputtering machine cannot control the thickness of the gold coating on sample surface. Different material coatings have also been used; platinum and carbon performed well in this case. They have smaller structure and the sputtering process can be controlled precisely in term of thickness and uniformity with the Gatan Precision Etching Coating System (PECS) Model-682 console.

Some specimens were not coated at all because of the need to examine them under Nomarski microscopy and SEM simultaneously. Particularly in the Nomarski microscope, the feature on and inside transparent or translucent materials can be easily investigated. Carbon tape was not used due to the difficulty to remove its residue from the sample after investigation with SEM.

Copper tape was grounding the dielectric materials better than carbon tape and easier to remove.

Some cleaning procedures were also performed. For AFM and SEM sample preparation, cleaning with acetone and ethanol in an ultrasonic bath was employed to get rid of dust or debris from micromachining. Subsequently, specimens were dried by leaving in the air and cleaned with plasma cleaning. Plasma cleaning was performed with a Solarus Model-950 from Gatan to get rid of hydrocarbon contamination on the surface. If it is necessary, plasma cleaning is also able to remove carbon coating.

3.1.3 Prior Transmission Electron Microscopy

Quartz is prone to amorphize under the beam in a Transmission Electron Microscope (TEM). The TEM CM-12 has an acceleration voltage of 120 keV. The surface coating with carbon was carried out with Gatan Precision Etching Coating System (PECS) Model-682 console on both sides of FIB-TEM sample with 1 nm thickness. The PECS stage was operated with 6 keV, 250 μA, 10°rocking, 12°/ second and 5 rpm rotation. After TEM investigation was performed, the carbon coated quartz TEM sample did not amorphize. It is evident that carbon coating is reliable protection for the quartz TEM sample.

3.2 Femtosecond Laser Machining Experiments

A series of femtosecond laser machining experiments were performed on the three different materials. The three different materials showed some conditional unique behaviors. Some of laser parameters for all series of experiments are the same, for example the repetition rate, the laser wavelength and the pulse duration range; some of them are different, such as the usage of 5× and 50× microscope objectives for surface and sub-surface micromachining works respectively. We introduced different energy levels to the three materials to create features in the range below to above the materials threshold. The laser experiments were classified based on the micromachining procedure. Each classification was coded with an X for experiment and is followed by number.

3.2.1 Single Pulse Ablation Experiment

Procedure of single pulse ablation experiment:

1. Single pulse ablation experiments [X1] were done on quartz sample with 20 different energy levels by changing optical density filter in order to introduce damage near and above the material threshold. The single pulse ablation experiment map is illustrated in Figure 3-1 and the calibration of the output energy to corresponding optical density is described in Figure 3-2.
2. The preliminary investigation for single pulse ablation feature was carried out with the Nomarski microscope.

3. The second investigation was performed with Scanning Electron Microscopy (SEM) to acquire detailed images of the features and the morphology of the crater.
4. The average diameters of the craters were measured from SEM micrographs. If the crater has elliptical shape, the diameter is the average of minor and major axis of ellipse.
5. The data of squared diameter D^2 of modified craters were plotted as a function of logarithm of laser energy Hence we can extrapolate the least square fit line of the plot to D^2 equals to zero value, and then find the single ablation threshold.

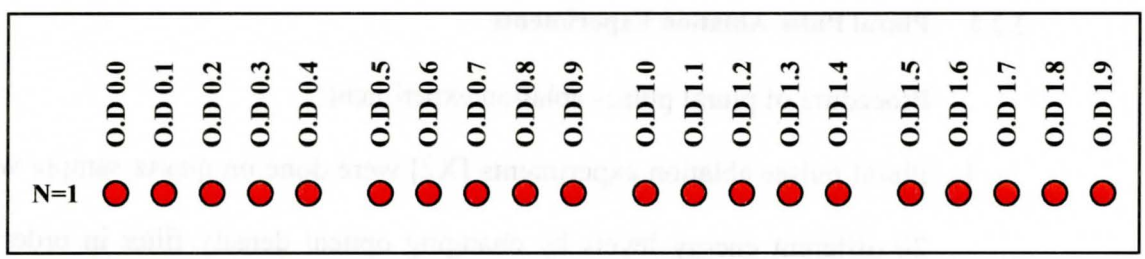

Figure 3-1: The pulse map of single pulse ablation experiment [X1] with 20 different energy levels.

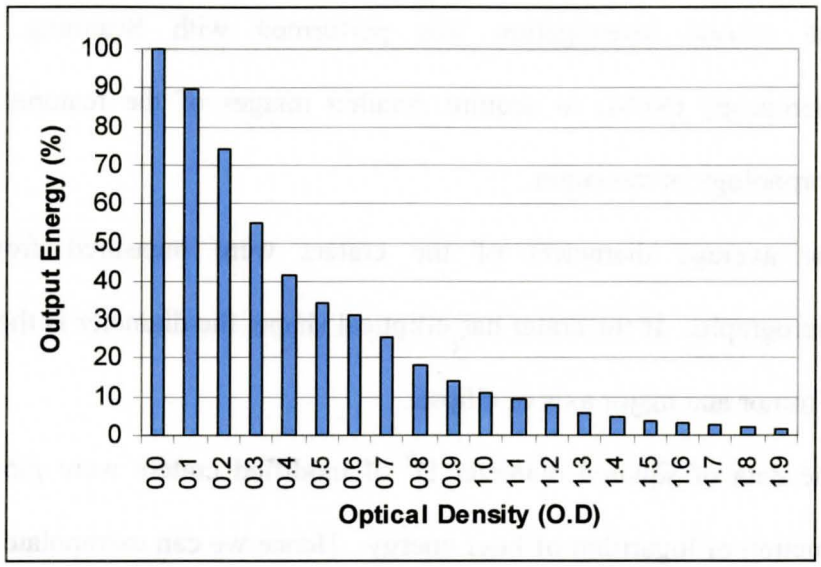

Figure 3-2: The output laser energy by using different optical density.

3.2.2 Plural Pulse Ablation Experiments

Procedure of plural pulses ablation experiment:

1 Plural pulses ablation experiments [X2] were done on quartz sample with 20 different energy levels by changing optical density filter in order to introduce damage below and above material threshold upon to laser energy Plural pulses means the laser beam hits the same spot in consecutive pulses less than and equal to 10 pulses, i.e. 2, 3, 4, 5, 7, and 10 pulses. This series of experiments is mapped in Figure 3-3.

2. The preliminary investigations of plural pulses ablation on the sample surface were carried out with Nomarski microscopy

3. The second investigations of plural pulses ablations were conducted with Scanning Electron Microscopy method to get detail features and morphology Imaging process was done on individual crater
4. SEM micrographs of the craters were then analyzed qualitatively and quantitatively from SEM micrographs. The qualitative analysis related to the additional feature that might appear, such as ripples and their orientations relative to the laser polarization, the final state and the shape of the crater The quantitative analysis related to dimension measurement of the craters.

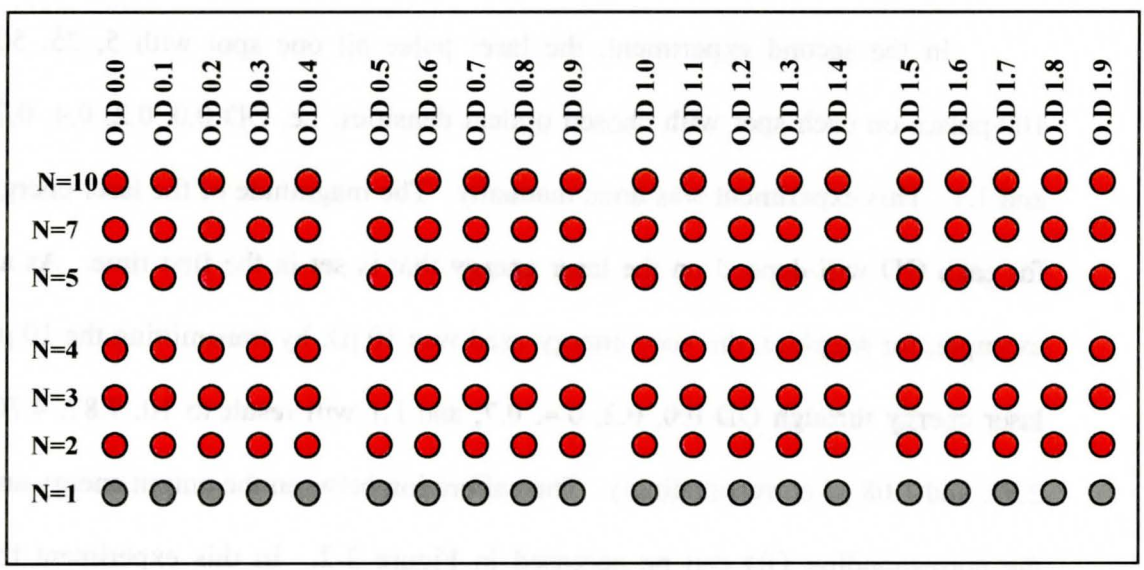

Figure 3-3: The pulse map of plural pulses ablation experiments [X2] ($2 \leq N \leq 10$) with 20 different energy levels.

3.2.3 Multiple Pulses Ablation Experiments

There were two kinds of experiment performed for multiple pulse ablations. In the first experiment, laser pulses with particular energy hit each spot with 20 consecutive pulses [X3]. This experiment is illustrated in Figure 3-4.

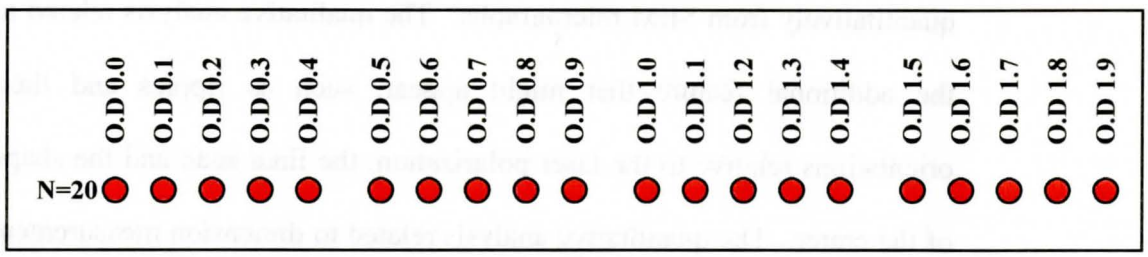

Figure 3-4: The pulse map of multiple pulses ablations experiments [X3] (N=20) with 20 different energy levels.

In the second experiment, the laser pulse hit one spot with 5, 25, 50, 100 pulses on each spot with chosen optical densities, i.e. OD 0.0, 0.2, 0.4, 0.7, and 1 1 This experiment was done manually The magnitude of the laser energy for each OD will depend on the laser energy that is set in the first time. As an example, for sapphire, the laser energy used was 10 μJ, by transmitting the 10 μJ laser energy through OD 0.0, 0.2, 0.4, 0.7, and 1 1 will result to 10, 7.87, 4.70, 2.91, and 1.08 μJ correspondingly The calibration between the output energy and the corresponding OD can be accessed in Figure 3-2. In this experiment the optical density was changed manually The spacing between two craters is made by using stepping button in the micromachining program, while number of pulses is controlled by the shutter time. For example to deliver 1 pulse, we open the

shutter for 20 ms; 5 pulses for 100 ms; 25 pulses for 500 ms; 50 pulses for 1000 ms and 100 pulses for 2000 ms.

The pulse map for multiple pulses ablation experiment [X4] is shown in Figure 3-5.

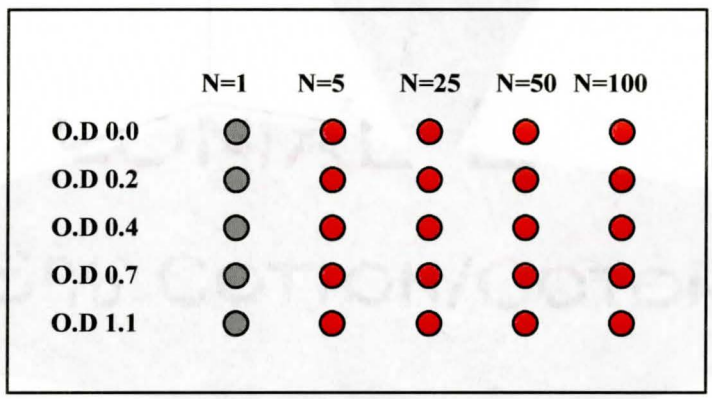

Figure 3-5: The pulse map of multiple pulses ablation experiment [X4] with N = 5, 25, 50, and 100 with the output laser energy set by OD 0.0, 0.2, 0.4, 0.7, and 1.1.

3.2.4 Surface Line Experiments

Continuous lines experiments [X5] on the surface of quartz, sapphire, and diamond were performed using Ti:Sapphire with a wavelength centered at about 800 nm, 500 μm/s feed rate and with different microscope objectives, Newport– 5× and 50×. The scheme of the surface line experiment is illustrated in Figure 3-6. The scanning direction is along the x-axis, the electric field polarization is along the y-axis and the red lines on the specimen in Figure 3-6 represent lines on the surface introduced by translated laser beam relative to the specimen on the stage.

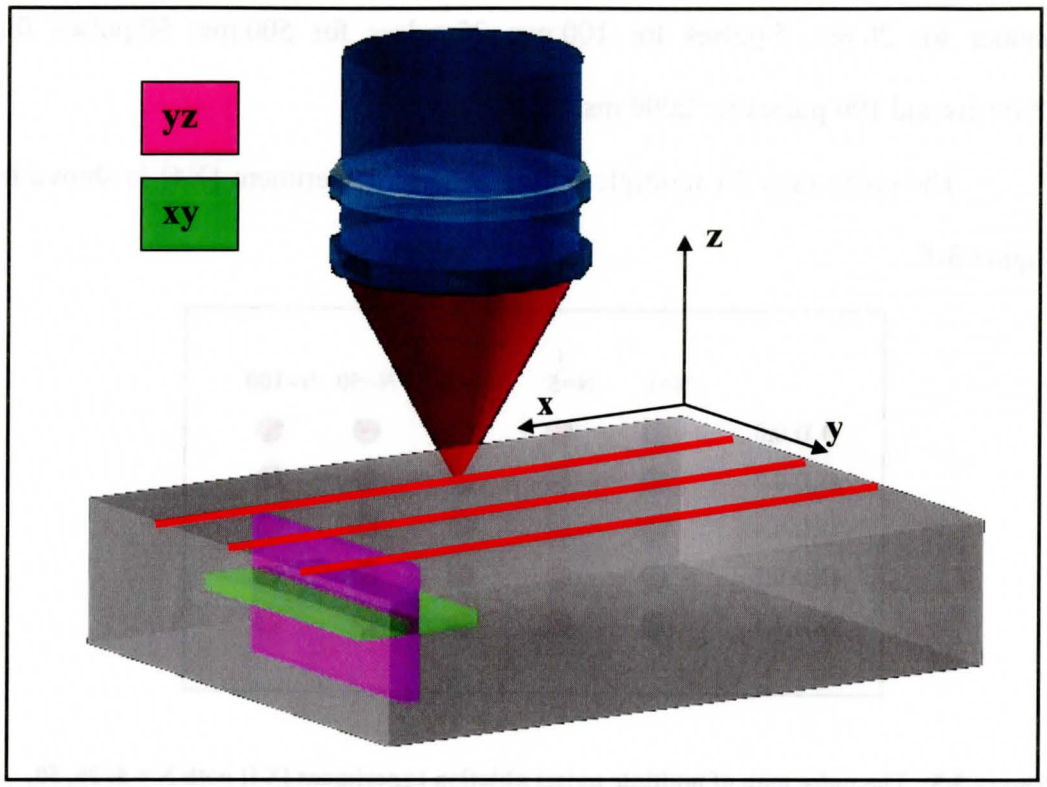

Figure 3-6: The schematic diagram of surface line experiments [X5], the scanning direction is along x-axis, the electric field polarization is along the y-axis.

3.2.5 Sub-surface Lines Experiments

There are two kinds of sub-surface surface lines experiments performed in this thesis. Firstly, the sub-surface lines were made by focusing laser beam with 50× microscope objective at the same depth into the bulk specimen. There are 15 lines with different energy The first kind of sub-surface lines experiment [X6] is described in Figure 3-7

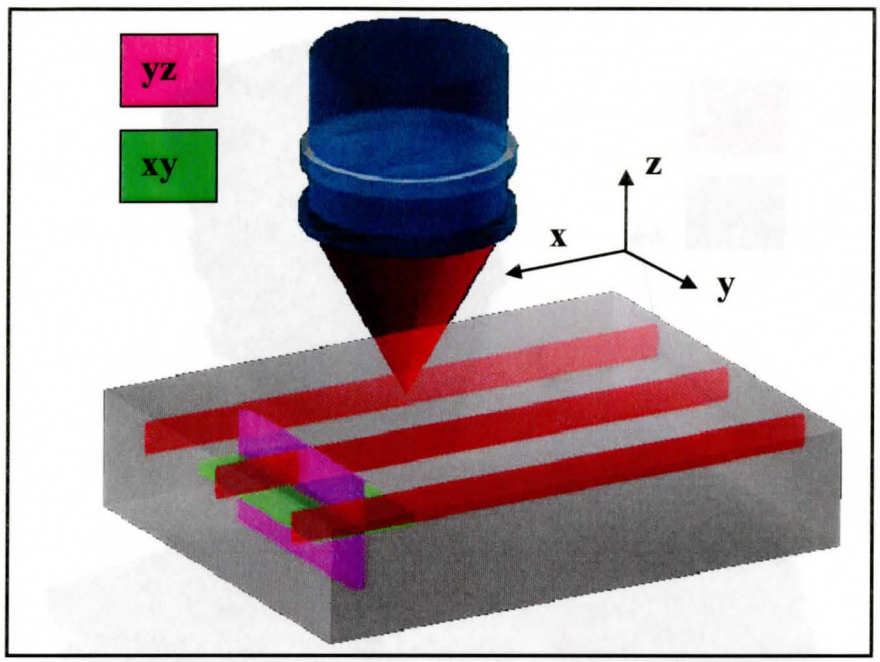

Figure 3-7: The schematic diagram of sub-surface lines experiment [X6] with different laser energy at the same depth level.

Secondly, the 14 lines sub-surface line experiments with gradual depth of 40 μm step (for quartz and sapphire) and 30 μm step (for diamond) were carried out. These experiments were performed 50× microscope objective, feed rate of 500 μm/s, with different pulse energy for each material. The scheme of sub-surface lines at different height levels [X7] is illustrated in Figure 3-8.

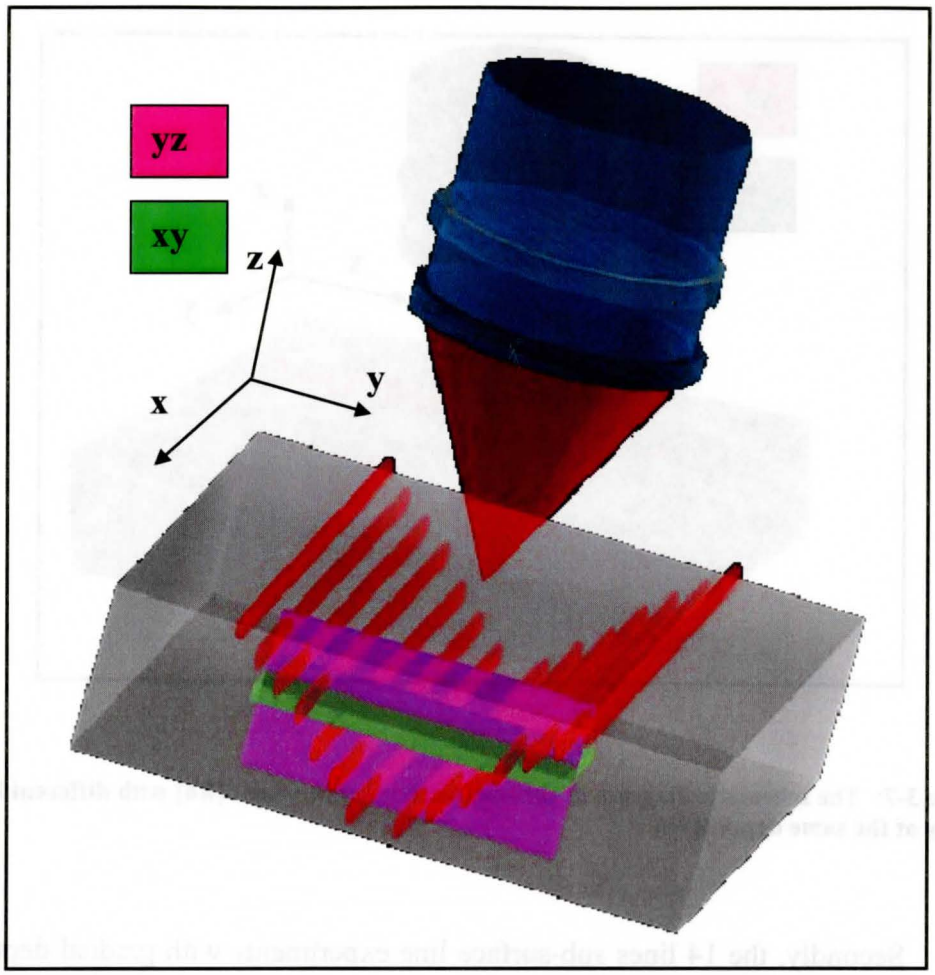

Figure 3-8: The schematic diagram of sub-surface lines experiment with the same laser energy at different height level [X7].

4 Results and Discussions

This chapter contains the laser and characterization parameters and also results of each experiment described in Chapter 3. All the results here will be referred to the corresponding experiment code mentioned in detail laser parameter in the previous chapter. X refers to experiment X1 to X7.

4.1 Analysis on Quartz

4.1.1 Single Pulse Experiment

It is important to note that the entire series of experiments were performed on different days and hence there are small variations in the laser output over the experimental timeframe. We observed minute to significant discrepancy in the spot size measurement from experiment to experiment. One source of change in the spot size may come from the uncertainty of the specimen upon the laser focus. Figure 4-1 shows SEM JEOL 7000F images of single pulse ablation experiments [X1] on quartz that were performed with the Ti:Sapphire laser with wavelength centered at λ=800 nm, laser energy E_p=10 μJ, pulse duration τ_l=165-177 fs in a rough vacuum of 40 mTorr and using (a) 5× microscope objective, ω_0=3.7 μm,

Φ=47 J/cm^2 and (b) 50× microscope objective, ω_0=2.8 μm, Φ=79 J/cm^2 . As we can see, all the laser parameters are the same, except the different microscope objectives yield two different spot sizes between the experiments (a) and (b). The 5× objective with ω_0=3.7 μm and the 50× objective with ω_0=2.8 μm will make the same laser energy of 10 μJ yield two different laser fluences, Φ=47 J/cm^2 and 79 J/cm^2 respectively. Note that the spot size of the 5× objective is smaller whereas the spot size of the 50× objective is larger than the expected value. So, with the same pulse energy and the smaller area, the material is exposed with higher pulse energy density. Both craters have a fiber-like structure splattered from the center to the edge. In Figure 4-1 (a) the crater produced by the larger spot size has a larger diameter of approximately 8.3 μm and more uniform structure from the center to periphery, whereas in (b) the crater produced by the smaller spot size has smaller diameter of approximately 6.7 μm and is strongly ablated as indicated by the hole in the center and a deep trench between a hole and its periphery.

From the micrographs in Figure 4-1 we can see the effect of different spot size on the final feature of the irradiated area. As expected, the tighter focus will give more severe and deeper damage to specimens due to the higher energy fluence.

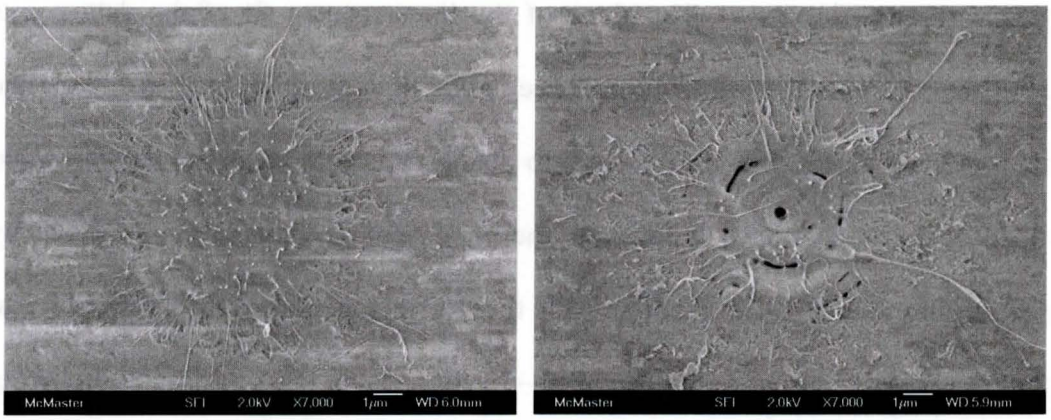

(a) (b)

Figure 4-1: SEM JEOL 7000F showed plan view of single pulse ablation crater on quartz performed with Ti:Sapphire centered around λ=800 nm, E=10 μJ, τ_p=165-177 fs using (a) Newport-5× microscope objective, ω_0=3.7 μm, Φ=47 J/cm^2 and (b) 50× microscope objective, ω_0=2.8 μm, Φ=79 J/cm^2.

The method used to measure the diameter of single pulse ablation for one material can not be applied directly to the other materials because each material may behave differently with respect to the laser beam. So, there is no absolute procedure to measure the crater diameter The crater in each material were handled and measured specifically

The single pulse ablation craters are used practically to determine spot size and single modification threshold. This method is known as the D^2 method, developed by J.M. Liu [81] and has been applied successfully to different materials [3, 4, 94, 95]. This technique is for pulsed Gaussian-beam spot sizes.

From the complete series of X1 experiments, we have data of the squared diameter D^2 and the laser energy By plotting the squared diameter D^2 on the y-axis and the logarithm of laser energy on the x-axis, the data points will form a

line with specific slope. The slope of the linear square fit of the data points represents the spot size of the beam. The next step in the analysis is to extrapolate the linear square fit line of D^2 to zero to obtain the single ablation laser threshold fluence Φ_{th}. We have calculated the modification threshold of quartz by performing single pulse ablation with the 1 kHz repetition rate Ti:Sapphire at 800 nm wavelength, using the Newport–5× microscope objective, and employing 20 different laser energies with maximum laser energy of 10 μJ. At the lower laser energies, the result will be undamaged regions. So the region between undamaged and damaged craters indicates where the threshold lies. Figure 4-2 shows the graph of squared diameter as a function of the logarithm of laser fluence. The slope indicates a spot size ω_0 of ≈3.7 μm for a Newport–5× microscope objective, which is smaller than the expected value (≈5 μm) and the extrapolation of the slope indicates a single pulse modification threshold of 3 J/cm^2 for quartz. From a separate experiment, the same result for the modification threshold is given by single pulse ablation experiment using 50× microscope objective. The 50× microscope objective yields a ≈2.8 μm spot size. As shown in Figure 4-2, it was challenging to find the right slope for a Newport–5× microscope objective. We observed three regimes on the plot with different slopes. However we did not observe distinct features among the three regimes. In addition, the existence of the three regimes was not reproducible in different experiments of single pulse ablation on quartz. For that reason, we took all the observable single pulse ablation craters into account to determine the spot

size. The single pulse ablation on quartz created "splashy" features with poorly defined boundaries which made the measurement of diameter quite subjective. However, we managed to track the common feature consistently throughout the diameter measurement process.

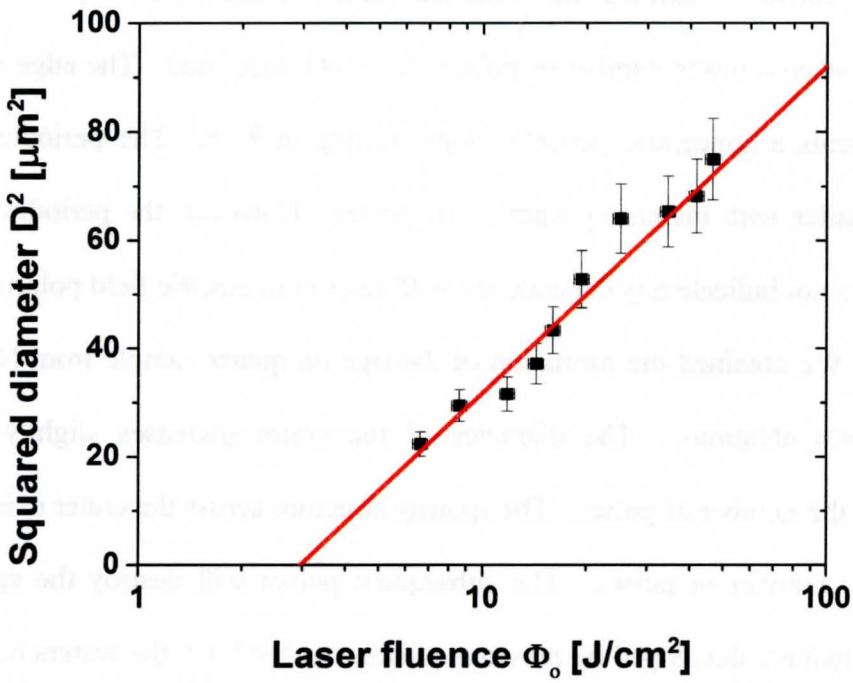

Figure 4-2: Squared diameter as a function of laser fluence where solid line showed linear square fit of the data points and extrapolation to $D^2=0$ to obtain single pulse ablation threshold fluence. This experiment was performed using a 5× microscope objective and a laser energy of 10 μJ. It yields a spot size of ω_0 of ≈3.7 μm and hence threshold fluence, Φ_{th}, of 3 J/cm^2 for quartz.

4.1.2 Plural Pulses Ablation Experiment

Figure 4-3 shows the SEM images of the craters with increasing number of low consecutive pulses, (a) N=1 (b) N=2 (c) N=3 (d) N=4 (e) N=5 (f) N=7

(g) N=10 hitting the same spot using 800 nm wavelength, 165-177 fs pulse duration, 10 μJ laser energy, 5× microscope objective with spot size $\omega_0 \approx 3.7$ μm, and energy fluence $\Phi = 46.5$ J/cm^2. Quartz shows similar behavior in the plural pulse ablation experiment [X2] as in the single pulse ablation experiment. A fiber-like structure splattered out from the center of the crater was observed, especially when a lower number of pulses (N = 1-4) were used. The edge of the craters reveals a concentric periodic rings starting at N=5. The periodicity is getting smaller with increasing number of pulses. However, the periodic rings structure do not indicate any dependency with respect to electric field polarization direction. We obtained the formation of damage on quartz sample from N=1 to N=10 pulses ablations. The diameter of the crater increases slightly with increasing the number of pulses. The splashy structure across the crater exists for a very low number of pulses. The subsequent pulses will destroy the splashy structures that are developed by previous pulses. At N=7–10, the craters become deeper because the splashy structure in the center does not exist anymore.

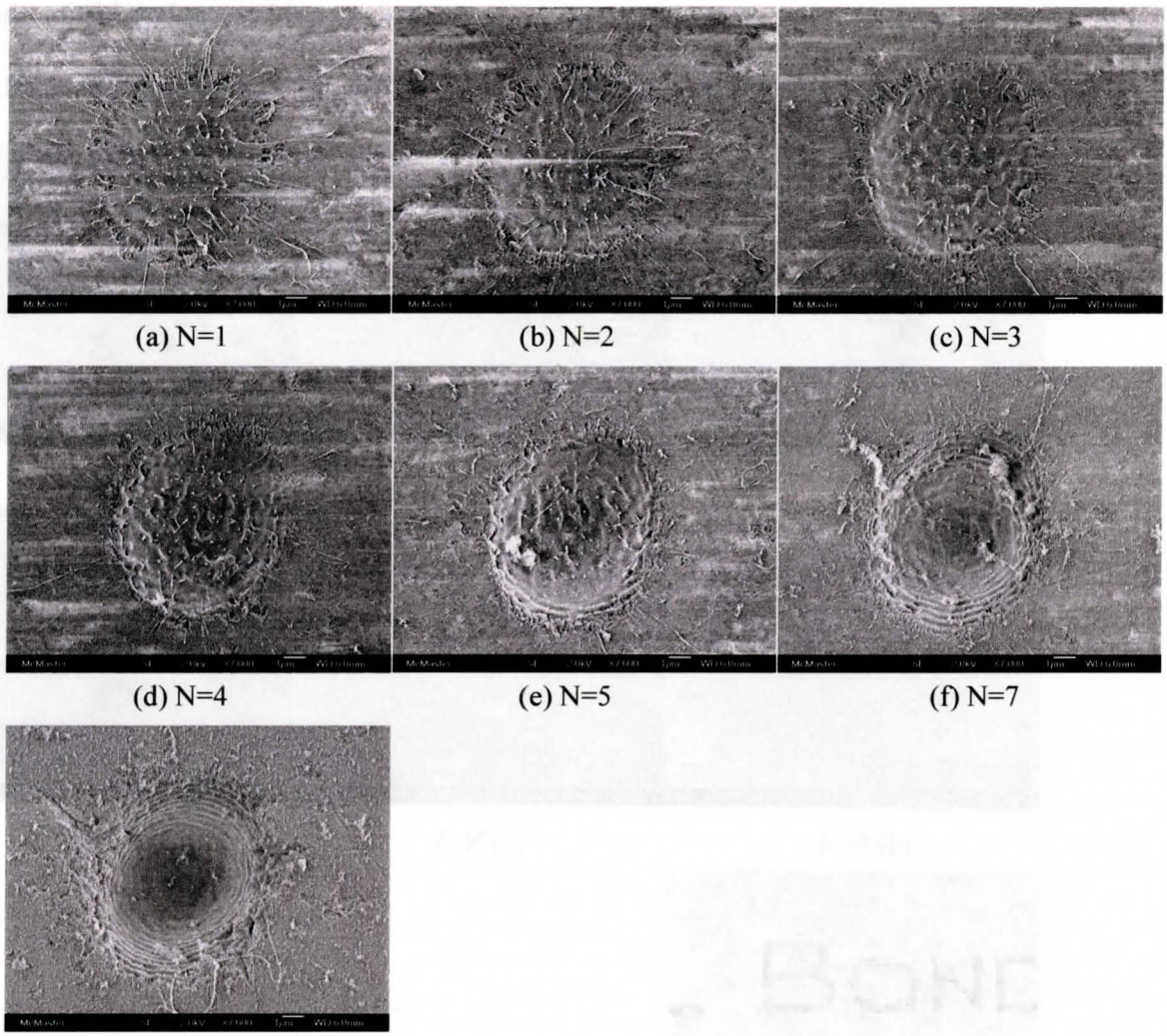

(a) N=1 (b) N=2 (c) N=3

(d) N=4 (e) N=5 (f) N=7

(g) N=10

Figure 4-3: SEM images show the craters created with increasing number of pulses, (a) N=1 (b) N=2 (c) N=3 (d) N=4 (e) N=5 (f) N=7 (g) N=10 hitting the same spot using an 800 nm laser wavelength, 165-177 fs pulse duration, 10 μJ laser energy, 5× microscope objective, with spot size $\omega_0 \approx 3.7$ μm, and energy fluence $\Phi = 46.5$ J/cm^2

Figure 4-4 shows SEM images of a different set of plural pulse ablation experiments on quartz. The experiments were performed at an 800 nm wavelength, 165-177 fs pulse duration, 20 μJ laser energy, using a Newport-5× microscope objective, with spot size $\omega_0 \approx 3.5$ μm, energy fluence $\Phi = 104.3$ J/cm^2,

and (a) N=1 (b) N=2 (c) N=3 (d) N=4 (e) N=5 (f) N=7 (g) N=10 pulses hitting the same location. At a higher numbers of pulses, chipping phenomenon is observed.

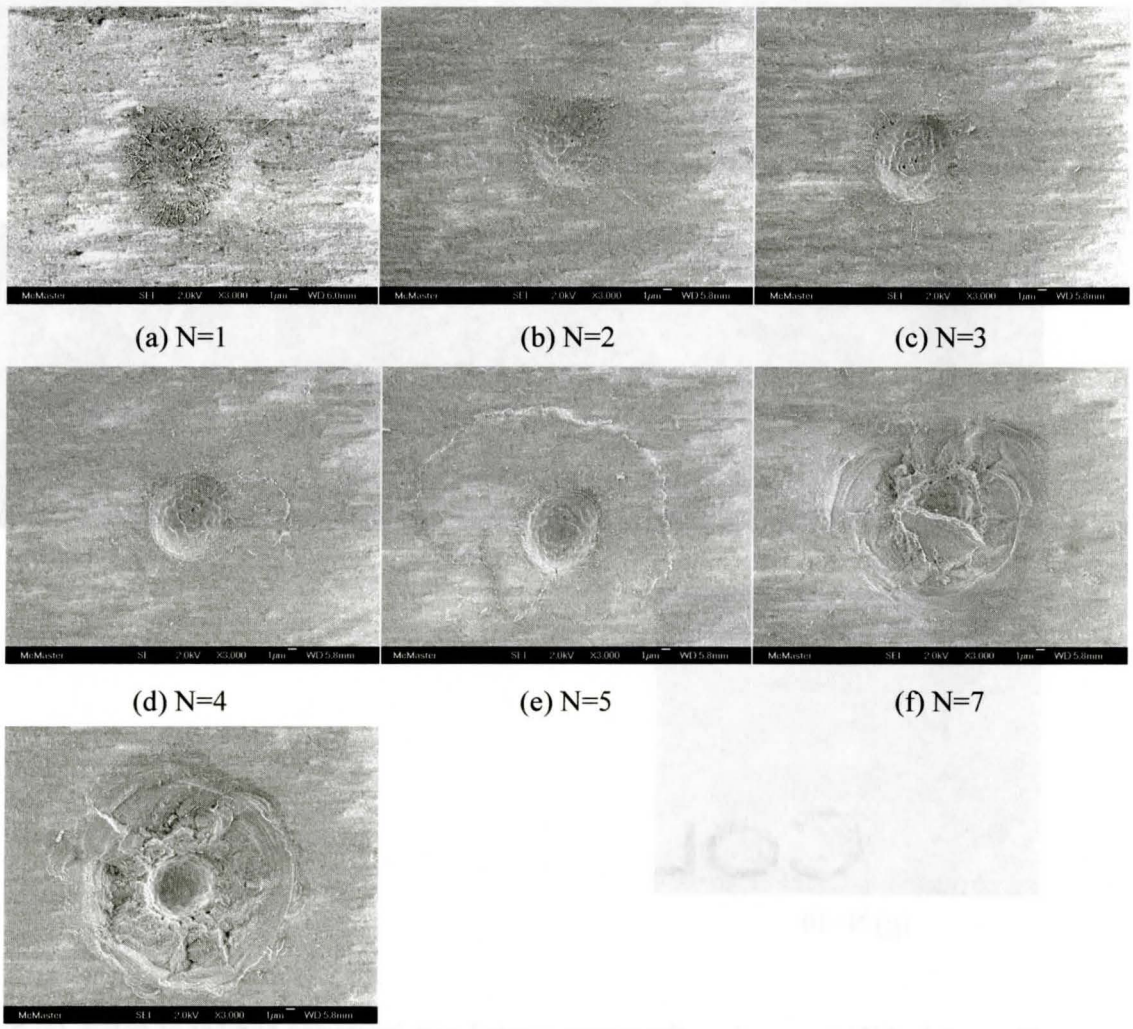

(a) N=1 (b) N=2 (c) N=3

(d) N=4 (e) N=5 (f) N=7

(g) N=10

Figure 4-4: SEM images shows craters with increasing number of pulses, (a) N=1 (b) N=2 (c) N=3 (d) N=4 (e) N=5 (f) N=7 (g) N=10 hitting the same location using an 800 nm wavelength, 165-177 fs pulse duration, 20 μJ laser energy, 5× microscope objective with spot size $\omega_0 \approx 3.5$ μm, and energy fluence $\Phi = 104.3$ J/cm^2.

Figure 4-3 and Figure 4-4 allow comparison the micromachining done with laser energy of 10 μJ and 20 μJ respectively The chipping mechanism is

more severe in the higher pulse energy and with higher number of pulses. The damage builds up within the first few pulses. When the material reaches a critical condition where the lattice bonding cannot stand further energized pulses, chipping happens.

4.1.3 Surface Line Experiment

Surface line experiments [X5] on the quartz sample produce droplet-like structures as shown in Figure 4-5. These surface lines were prepared with an 800 nm wavelength, 150 fs pulse duration, 5.0 μJ and 4.6 μJ laser energy, using 50× microscope objective, with spot size $\omega_0 \approx 2.8$ μm and 500 μm/s feed rate. The electric field polarization is perpendicular to the groove length. The droplet-like structure does not indicate a preferred orientation with respect to the electric field polarization direction. Cracks appear almost perpendicular to the groove surface. Figure 4-5 (a) shows the cross-section of the two grooves after milling with the FIB. The coarse FIB milling was performed with a 30 keV:3nA probe which produced a smooth surface, and then followed by fine milling with 30 keV:300 pA probe. Figure 4-5 shows a flat cross-section of the groove where the cracks lie beneath the grooves and propagate away perpendicularly from the groove. Another investigation about bursts of femtosecond laser pulses with different repetition rates and number of pulses have been done [96]. The burst micromachining provides control the heat diffusion so that the optimum

morphology of the structures can be achieved. The cracking phenomenon in micromachining of quartz may be reduced with this pulse burst method.

The 50× microscope objective used to prepare the grooves has short confocal parameter and small spot size, making the groove quite deep due to higher laser fluence. In addition, as the pulse moves over the surface, the sample is exposed to multiple pulses in the same location. That number of pulses can be calculated from the effective number of pulses, N_{eff}, equation.

$$N_{eff} = \sqrt{\frac{\pi}{2}} \frac{\omega_0 f}{v} \qquad \textbf{Equation 4-1}$$

With a feed rate v=500 μm/s, repetition rate f = 1 kHz, and spot size $\omega_0 \approx 2.8$ μm, we will have $N_{eff} \approx 7$ (meaning 7 pulses per location). Next, Figure 4-5 (b) and (c) are the plan view images of the grooves created with energy fluence Φ = 39 J/cm^2 and 36 J/cm^2 respectively.

The SEM micrographs in Figure 4-5 were taken with Secondary Electron 2 (SE2) detector at acceleration voltage of 3 keV [Figure 4-5(a)] and 2 keV [Figure 4-5 (b) and (c)]. The sample surface was coated with a platinum layer about 25 Å thick to avoid electron charging of the sample.

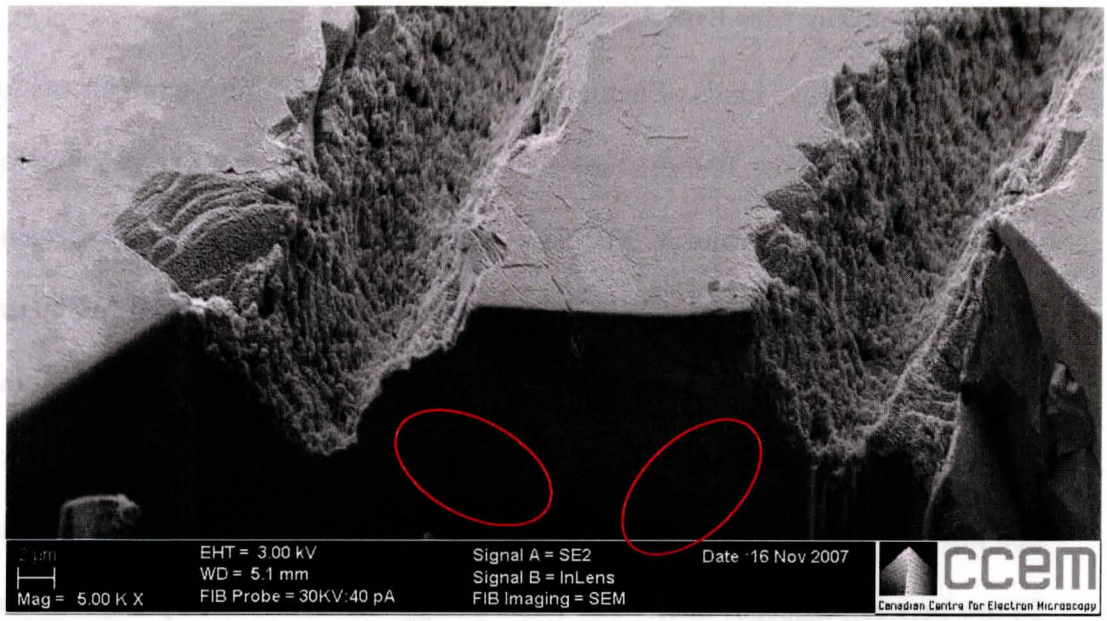

(a)

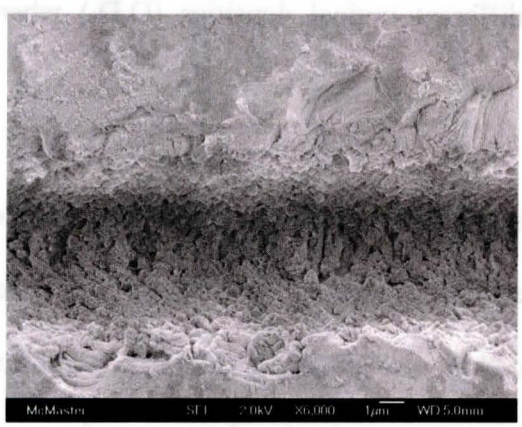

(b)

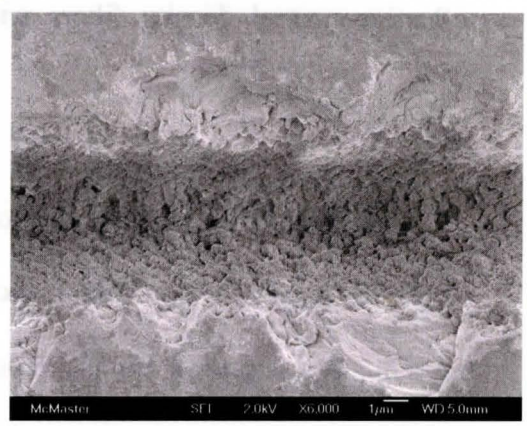

(c)

Figure 4-5: (a) SEM+FIB image shows the cross section of surface linear gratings on quartz using an 800 nm wavelength, 150 fs pulse duration, 50× microscope objective, with spot size $\omega_0 \approx 2.8$ μm, and laser energies of 5 μJ and 4.6 μJ, for left and right-hand side groove respectively. Plan views of the (b) 5 μJ and (c) 4.6 μJ grooves are shown in (b) and (c) respectively.

4.1.4 Sub-surface Line Experiment

There are two kinds of femtosecond laser micromachining experiments for sub-surface continuous line irradiation in bulk quartz. The first one is following the experimental procedure of X6. This experiment was performed by focusing the 15 different laser energies with a 50× microscope objective down to 200 μm with a maximum laser energy of 5 μJ. The sub-surface micromachining processing was conducted with a pulse duration of 165-177 fs and a feed rate of 500 μm/s in rough vacuum of 40 mTorr. We produced 15 lines with a spacing of 25 μm between adjacent lines. The pulse energy was controlled by a set of thin, reflective neutral density filters with different optical densities (O.D.) where $\frac{P_{out}}{P_{in}} = 10^{-O.D.}$.

Figure 4-6(a) provides a cross-sectional (yz-plane) view of the sample. The SEM image was not clear due to electron charging effects. We could not see the sub-surface groove on the cross-section plane using a 2 keV acceleration voltage, despite increasing the acceleration voltage and using faster scanning rates in order to be able to investigate the lines. Finally, we were able to see the feature on the cross-section (yz-plane) at an acceleration voltage of 5 keV using the In-Lens detector. The length (in the z–direction) of the set of lines on the cross-section (yz-plane) were almost similar due to the small difference in pulse energy between sequential spots, so they do not reveal the obvious difference in lengths

of sub-surface damage observed in fused silica where two sequential spots are shot with pulse energies differing by a factor of two [97, 98].

Further characterization of this cross-section of sub-surface lines was performed with a FIB+SEM NVision-40 dual beam. Figure 4-6(b) is an image captured with the In-Lens detector. We milled the quartz sample with Ga^+ ions perpendicular to the cross section plane (xy-plane) in order to be able to see sub-surface feature. The process to make a milled box of the cross-section was performed with a 30 keV:3 nA probe. The alternating fringes lie along the sub-surface line that is seen from the bottom (xy-plane). Figure 4-6(c) shows the experimental set-up in which the direction of the electric field polarization is along the y-axis and the laser irradiation direction is along the x-axis.

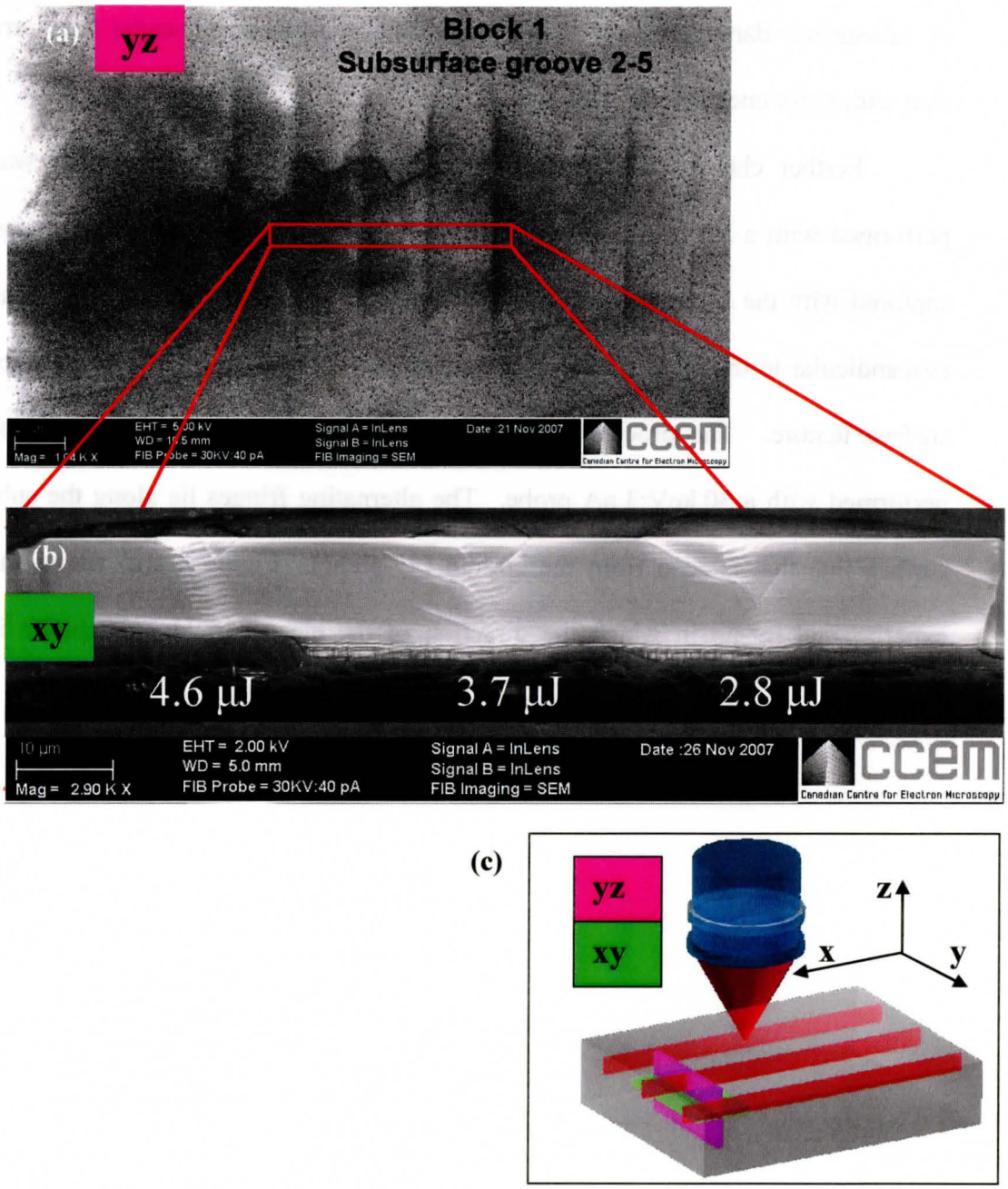

Figure 4-6: SEM+FIB images show (a) the cross-section (yz-plane) of decreasing energy sub-surface grooves from left to right (b) alternating fringes that were obtained after milling the laser irradiated area on the cross section of some grooves in (a) with Ga^+ ions. Three different areas are indicated which were irradiated with pulse energies of 4.6 µJ, 3.7 µJ, and 2.8 µJ (c) Experimental diagram shows the xy- and yz-planes. The scanning direction is along x-axis while the electric field polarization is along y-axis.

Figure 4-7 shows higher magnification micrographs of the sub-surface continuous lines on quartz shown in previous figure [Figure 4-6(b)]. We can see the cracks spread from the core of the fringes. The images were taken with the In-Lens detector in NVision-40 FIB+SEM machine at 3 keV acceleration voltage. The sample was grounded with copper tape to reduce charging effects. The spacing of the alternating structure is on the order of the laser wavelength (800 nm). It is consistent with the fundamental spacing of the laser induced periodic surface structures (LIPSS) [17] as mentioned in Chapter 2, which is surprising for sub-surface laser irradiation work. With the pulse energies of 4.6 μJ, 3.7 μJ, and 2.8 μJ, the alternating structures' spacings are approximately 725 nm, 785 nm, and 806 nm respectively. This measurement was performed perpendicularly to the alternating structures direction. The tracks of the alternating structures on the xy-plane [Figure 4-6 or Figure 4-7] do not run parallel to the yz-plane because the scanning direction was not exactly perpendicular to the edge of the specimen. The dependency of the spacing on the local fluence has been observed by Bonse et al [29] and Yasumaru et al [99]. However, even though the trend in this experiment is not significant (because of all the spacings observed are still in the near-wavelength regime), the measurement shows that the spacing increases slightly with decreasing fluence.

In similar experiments, Hnatovsky et al and Bhardwaj et al [30, 100] observed alternating structures in fused silica with spacing close to 242 nm ($\approx\lambda/2n$, where n is refractive index of fused silica) and with an orientation

perpendicular to the electric field polarization. Overlap of the beam while it is translated relative to the sample results in consecutive pulses irradiation of the sample for a given region. Despite Hnatovsky et al and Bhardwaj et al employed an objective with a higher Numerical Aperture of 0.65, higher repetition rate of 100 kHz and having a much lower feed rate of 30 μm/s than in our experiment, the effective number of pulses for a given region N_{eff}, in our experiment, where a 1 kHz repetition rate and feed rate of 500 μm/s were used. It may be interesting to try other much slower speeds in the future.

In the micromachining process of continuous lines, the material is exposed to consecutive pulses while being translated at a feed rate of v. The feed rate can be expressed to the effective number of pulses in order to compare the micromachining process of multiple pulse ablation in stationary micromachining. Hsu et al [28]observed in periodic surface structures that high numbers of pulses tend to generate closely-spaced LIPSS (High Spatial Frequency LIPSS, HSFL), while LIPSS with spacing on the order of the irradiation wavelength (Low Spatial Frequency LIPSS, LSFL) tend to dominate for a location irradiated with a low number of pulses. So, the LIPSS spacing is influenced by the wavelength, the effective number of pulses of the incident laser, and the fluence.

We also observed in our results that the orientation of this alternating sub-structure with respect to the polarization direction differs from Hnatovsky et al and Taylor et al [30, 101-103] in fused silica. The fact that the orientation of alternating structures is parallel with respect to electric field polarization has also

been found in surface modification work in some materials, for example diamond in this thesis and [24] and ZnSe [26]. Nonetheless, the reason for perpendicular or parallel ripples orientation with respect to electric field polarization is still under discussion.

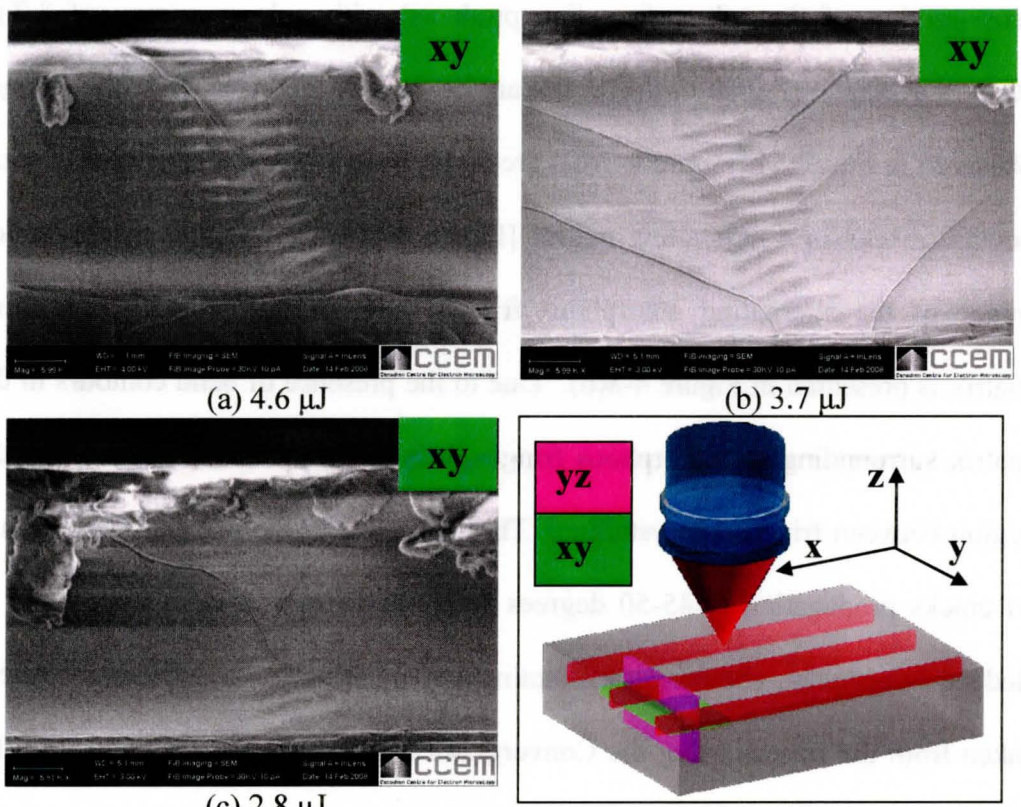

(a) 4.6 μJ (b) 3.7 μJ

(c) 2.8 μJ

Figure 4-7: SEM+FIB images with 3 keV acceleration voltage show the higher magnification of sub-structure linear grating on quartz. It can be seen that cracks grow from the area of the fringes. The fringes spacings are close to the laser wavelength of 800 nm and parallel to the electric field polarization direction.

In order to understand the structure of the observed features, further investigations were carried out by TEM. One selected region was prepared using the lift-out method by extracting a thin electron transparent lamella using focused ion beam [89]. From bright-field imaging and electron diffraction patterns of the cross-section of the sub-surface line produced with a laser energy of 3.7 μJ ($\Phi = 29.4$ J/cm^2) [Figure 4-8(a)], it can be readily deduced that the fringes observed in the SEM [Figure 4-7(b)] are amorphous while the surrounding areas contain cracks in a crystalline matrix [Figure 4-8(a)]. A higher magnification image of the alternating amorphous fringes core surrounded with crystalline matrix is presented in Figure 4-8(b). Due to the presence of bend contours in the matrix surrounding the amorphous fringes, it is also possible to deduce that the region between fringes is crystalline. The relaxation in the foil and the presence of cracks propagating at 45-50 degrees from the fringes make it impossible to deduce information about residual strain between fringes. A diffraction pattern taken from the fringes using the Convergent Beam Electron Diffraction (CBED) method demonstrates an amorphous structure [Figure 4-8(e)], while the patterns from the surrounding area are consistent with the quartz crystal structure [Figure 4-8(c)]. The quartz crystal structure simulated using Java based on Electron Microscopy Software (JEMS) indicates the $P3_221$ space group [Figure 4-8(d)]. This observation proves that there is no crystal structure change after femtosecond laser irradiation outside the fringes region on quartz.

Gorelik et al [104] investigated sub-surface laser irradiated quartz and observed the structure from a side viewpoint with TEM, parallel to the laser propagation (which is perpendicular to our TEM investigation [Figure 4-8]). We observed comparable results where a relatively sharp interface between the amorphous core and the crystalline matrix exists. They observed the material inside the irradiated ellipse was found to be amorphous surrounded by a highly defective crystalline matrix and that the defective area does not arise from thickness variation inside the specimen. The amorphous region is caused by the high viscosity of quartz that makes the recrystallization of pure quartz very slow [105]. Another condition that leads to the presence of the amorphous region is the high-pressure occurs around the fast-expanding plasma. For that reason, amorphization is expected to happen [106]. When lower feed rates (100 and 400 μm/s) were used, they observed a similar shape for the irradiated region but surprisingly the material inside was no longer amorphous.

Another cross-section TEM investigation on sapphire was performed by Juodkazis et al [107]. First, they investigated a region made by a single pulse inside sapphire with 30 nJ pulse energy, NA 1.35 objective, 0.14 μm^2 and 0.25 μm^2 focal volume and with 220 fs pulse duration. The crystalline region was transformed to amorphous with abrupt boundary and at higher pulse energies, void formation was observed at the center of amorphous area. Next, they investigated a region modified by multiple pulse irradiation inside sapphire. The amorphous region was transformed to polycrystalline. Multiple pulse deposits

enough energy to form the more thermodynamically stable polycrystalline phase and also the amorphous material has higher absorption coefficient to trigger precipitation of the polycrystalline phase. In their femtosecond pulse experiments inside sapphire, no crack formation and compositional changes (from crystalline to amorphous, from amorphous to polycrystalline state) were observed.

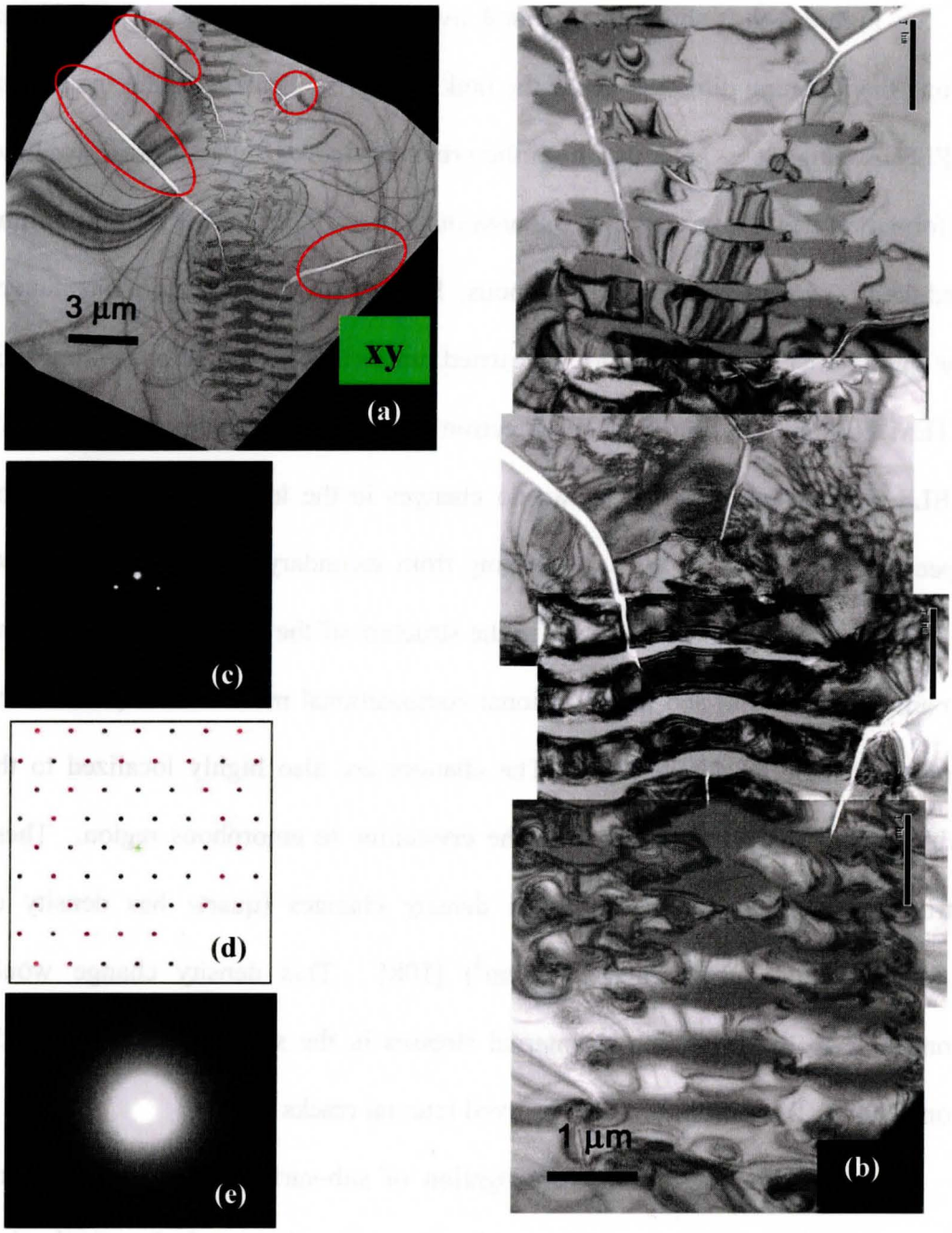

Figure 4-8: (a) The general overview of the FIB-TEM sample of the sub-surface continuous line with laser energy of 3.7 µJ (Φ = 29.4 J/cm^2) (b) The higher magnification of the fringes (c) The diffraction pattern of crystalline area (d) The simulated diffraction pattern of quartz structure using JEMS (e) The diffraction pattern of the darker fringes.

Figure 4-9(a) shows the general overview of the interior of the fringes along the scanning direction inside the bulk of quartz. Dots represent the area of EELS investigation. Note that from the previous figure [Figure 4-8(a)], we have information that the structure of the area outside of the fringes is still crystalline and the fringes themselves are amorphous. In order to confirm the composition of the quartz after laser irradiation, we carried out further investigations with a VG-STEM HB-601 UX 100 keV for Electron Energy Loss Spectroscopy (EELS). EELS work [Figure 4-9(b)] shows no changes in the low loss structure of the spectrum and no additional peaks arising from secondary phases. This suggests that the changes are only observed in the structure of the quartz (from crystalline to amorphous silica) and that additional compositional modification (such as the presence of Si) is not detected. The changes are also highly localized to the fringes with sharp transitions from the crystalline to amorphous region. These structural changes accompany local density changes (quartz has density of 2.65 g/cm^3 and fused silica 2.2 g/cm^3) [108]. This density change would contribute to the formation of internal stresses in the sample and subsequently contribute to the presence of the observed internal cracks [108].

In our high resolution investigation of sub-surface laser irradiation on quartz, we did not observe voids resulting from the micro explosion mechanism [16, 109-112]. In microexplosion theory, when femtosecond laser pulses are focused tightly inside transparent materials, the damage will be confined inside the materials. A very high fluence near the focus can result in nonlinear

multiphoton absorption and subsequent avalanche ionization of the materials. An increase in temperature at constant volume induces a hot plasma formation and expansion with a shock wave, yielding a micro explosion. This explosion may permanently damage the materials and induce voids in the centre of the damage region. Glezer et al [16] investigated voids by polishing down the sample until the surface level reached the internal structure and viewed under an SEM. The sample was tilted to reveal the morphology in order to distinguish a protrusion or a cavity. The protrusions imply the creation of denser, harder material, which is more resistant to the mechanical polishing, whereas the cavities imply the opposite properties. However, we need to consider our observations above where by doing laser irradiation inside the transparent materials, we modified materials from crystalline state to amorphous state, from denser to less dense materials, without necessarily forming any voids.

Glezer et al [16] created the sub-surface structure with a laser energy of 0.5 μJ (the threshold value is 0.3 μJ), pulse duration of 100 fs, wavelength of 780 nm, focused by a 0.65 NA microscope objectives with a spot size of 1 μm. Assuming we can trust that our spot size is 2.8 μm, the laser energy of 3.7 μJ, pulse duration of 170 fs, wavelength of 800 nm, and focused by a 0.42 NA. From the fluence calculation, we get 32 μJ and 30 μJ for the experiment performed by Glezer et al and our experiment respectively. From the intensity calculation, we get 16 W/cm^2 and 9 W/cm^2 for the experiment of Glezer et al and ours respectively. So the fluences for these two cases above are comparable, but due

to the shorter pulse duration, the laser intensity used by Glezer et al is almost twice higher than ours.

The voids may not be necessarily observed in tightly focused femtosecond laser pulses in bulk transparent materials. Schaffer et al [113] investigated a transition in morphology from structures produced by single pulses focused with 1.4 NA. Three different structures were observed with increasing energy: from 36 nJ, to 140 nJ and to 500 nJ created from small surface relief, to a void, and to extensive cracking inside the materials respectively. Our experiment above was in the regime of cracking instead of voids formation. The voids formation may depend on the focusing condition.

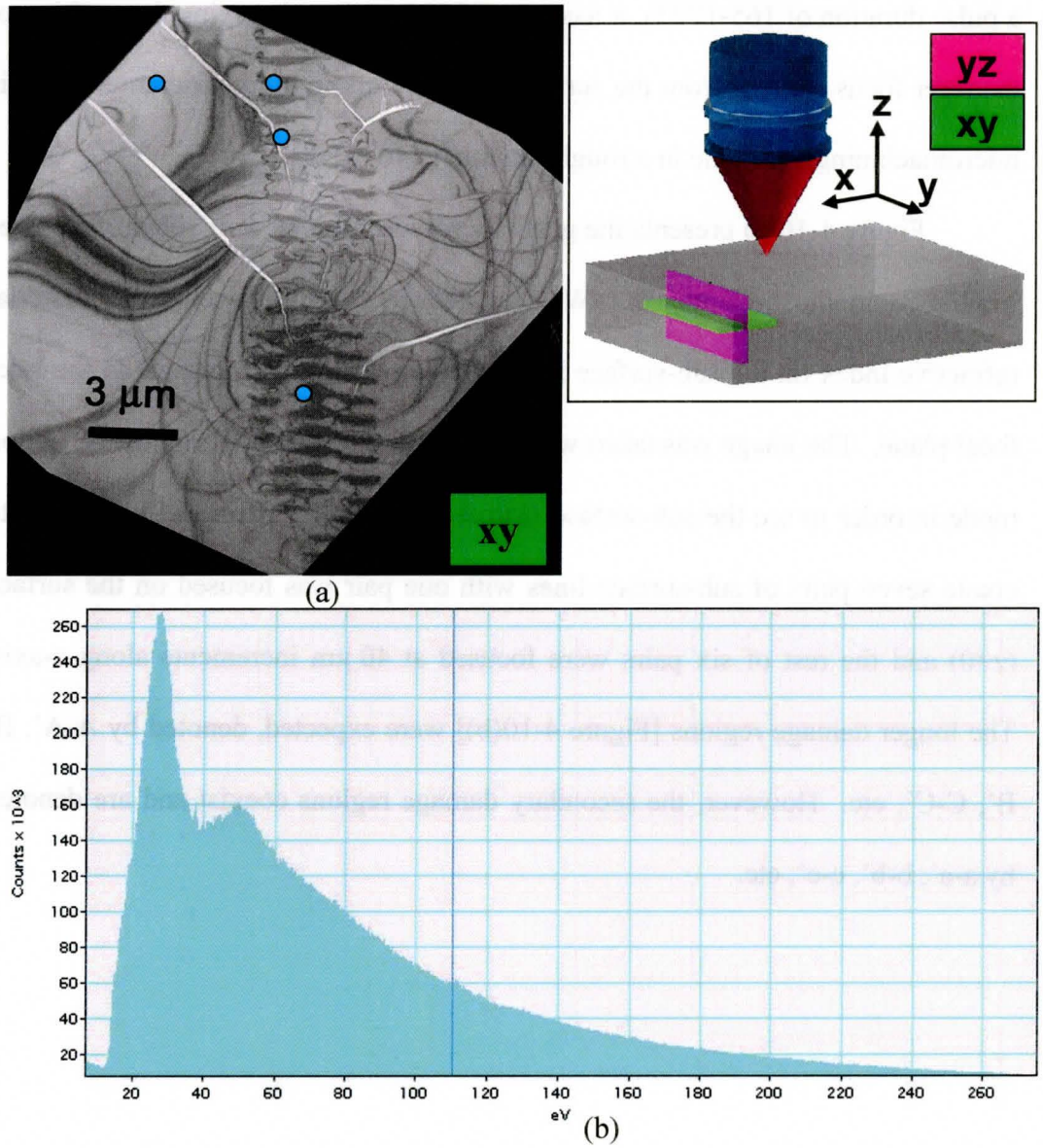

Figure 4-9: (a) The general overview of the alternating structure along the scanning direction inside the bulk of quartz. The dots represent the area of EELS investigation. (b) The EELS spectrum shows that the crystalline area and amorphous area have the same composition. There is no composition change after femtosecond laser irradiation.

The second type of sub-surface continuous line grating experiment [X7] was performed by using a laser energy of 10 µJ with a 50× microscope objective,

a pulse duration of 165-177 fs, a feed rate of 500 μm/s and varying the position of the laser focus starting from the surface into the bulk in 40 μm increments. This micromachining was done in a rough vacuum at 46 mTorr.

Figure 4-10(a) presents the general cross-section view of sub-surface lines irradiation in the bulk quartz. We can deduce the influence of the material refractive index on the sub-surface line damage position with respect to the laser focal plane. The image was taken with Nomarski microscopy using the reflection mode in order to see the sub-surface features in quartz. Intentionally we tried to create seven pairs of sub-surface lines with one pair was focused on the surface (z=0) and the rest of six pairs were focused at 40 μm increments along z-axis. The longer damage regions [Figure 4-10(b)] were expected, denoted by A-A', B-B', C-C', etc. However, the secondary damage regions coexist and are denoted by a-a', b-b', c-c', etc.

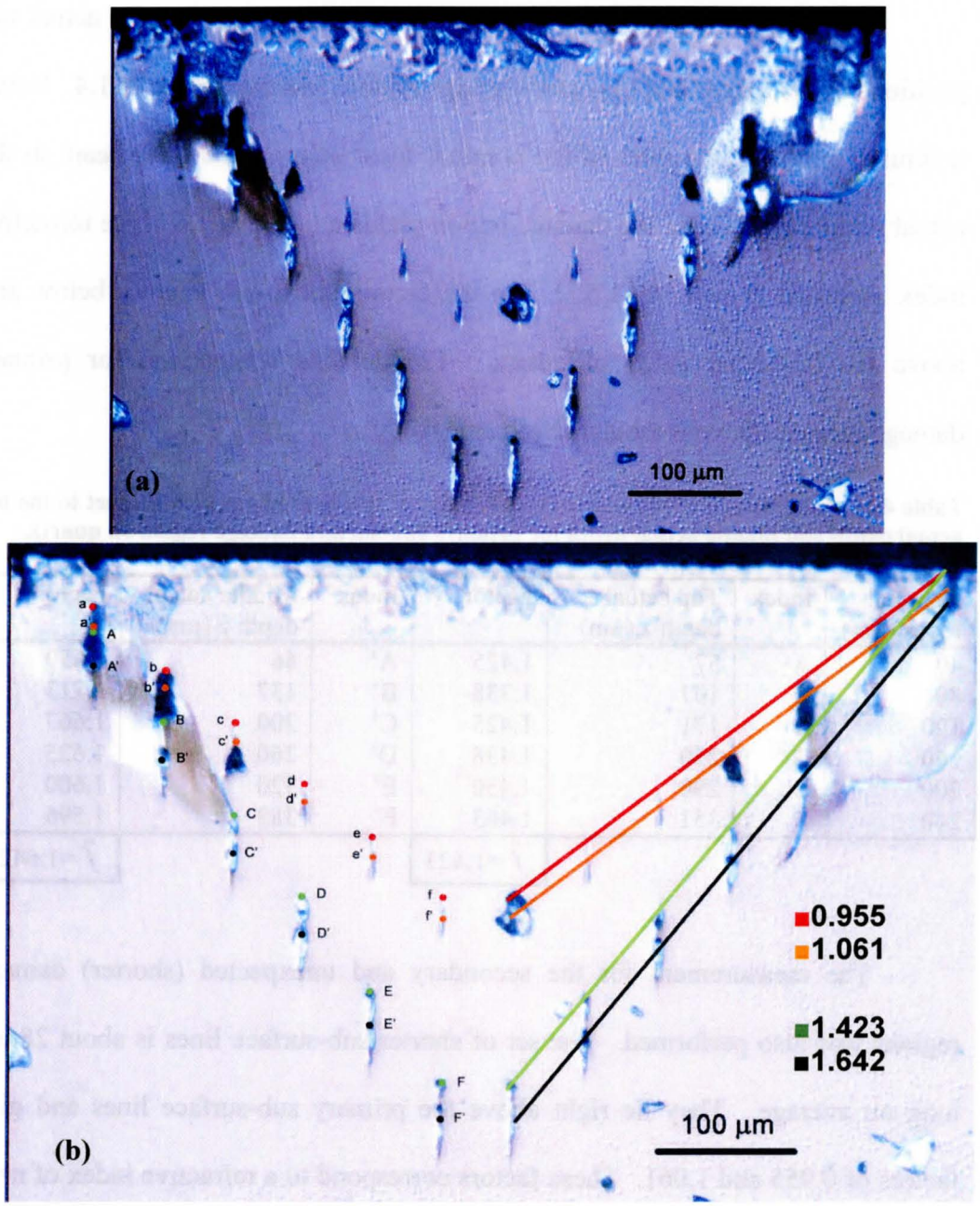

Figure 4-10: Image taken with a Nomarski microscopy shows the position of the sub-surface linear grating with a 50× microscope objective, 10 µJ laser energy, and 78.7 J/cm^2 energy fluence, gradually moving the laser focus down in 40 µm steps relative to the surface. The ratio of the nominal focal point to the actual top position and the ratio of the nominal focal point to the middle position of the longer damage region are 1.4 and 1.6 respectively; the ratio of the nominal focal point to the actual top position and the ratio of the nominal focal point to the middle position of the shorter damage region are 0.95 and 1.1 respectively.

The ratio of the nominal focal point of the laser beam to the actual top positions of the longer and expected damage regions yields a factor of 1.4. Using a similar approach, the ratio of the nominal focal point of the laser beam to the actual middle position of the damage region yields a factor of 1.6. The refractive index of quartz is n=1.543-1.552. So the factors above are slightly below and above the refractive index of quartz. The detailed comparison for primary damage regions above is tabulated in Table 4-1.

Table 4-1: Comparison of the nominal focal point of the laser beam with respect to the top actual depth and middle actual depth for primary sub-surface damage region on quartz.

Nominal focus (μm)	Index	Top actual depth z (μm)	Factor	Index	Middle actual depth z (μm)	Factor
40	A	57	1.425	A'	66	1.650
80	B	107	1.338	B'	137	1.713
120	C	171	1.425	C'	200	1.667
160	D	230	1.438	D'	260	1.625
200	E	290	1.450	E'	320	1.600
240	F	351	1.463	F'	383	1.596
			$\bar{f}$ =1.423			$\bar{f}$ =1.642

The measurement for the secondary and unexpected (shorter) damage regions was also performed. The set of shorter sub-surface lines is about 28 μm long on average. They lie right above the primary sub-surface lines and give factors of 0.955 and 1.061. These factors correspond to a refractive index of n=1. The detailed comparison for primary damage regions above is tabulated in Table 4-2. The lengths of the longer damaged structures are about 64 μm. The calculated Rayleigh range z_r is about 32 μm or in other words the confocal parameter is about 64 μm. The length of modified area is very close to the

confocal parameter value. We speculate that the secondary (shorter) sub-surface lines were coming from the fact that the laser beam interacted with air/vacuum while the specimen inside the chamber was translated relative to the laser beam at the quartz-air interface, so there is the effect of the refractive index of air focused to quartz cross-section plane.

Despite the length of the modified area and the confocal parameter are very close, we should consider about the self-focusing since the laser was focused inside the transparent material in this case. The ablation threshold obtained from single pulse experiment on the surface can not be used since the bulk threshold is higher than the surface threshold. However, bulk threshold measurements are not easily determined due to the complications associated with self-focusing, aberration, dispersion, and self-phase modulation [114].

From observable modified and/or damaged region in the bulk of quartz, the laser peak power in this experiment must exceed the bulk threshold for quartz. However we should have further experiments and investigations to determine the magnitude of the fluence with respect to the bulk threshold. The femtosecond pulses employed in this experiment (a pulse energy of 10 μJ and a pulse duration of 165-177 fs) has a peak power of about 60 MW, which is above the P_{cr} on quartz of about 2 MW. Thus, self-focusing mechanism needs to be taken into account. The value of the factors in Table 4-1 and Table 4-2 depict consistent value with refractive index. The discrepancy between the refractive index and the factors may indicate the self-focusing effect.

Table 4-2: Comparison of the nominal focal point of the laser beam with respect to the top actual depth and middle actual depth for secondary sub-surface damage region on quartz.

Nominal focus (μm)	Index	Top actual depth z (μm)	Factor	Index	Middle actual depth z (μm)	Factor
40	a	38	0.950	a'	43	1.075
80	b	77	0.963	b'	91	1.138
120	c	118	0.983	c'	132	1.100
160	d	151	0.944	d'	164	1.025
200	e	188	0.940	e'	204	1.020
240	f	228	0.950	f'	242	1.008
			$\bar{f}$=0.955			$\bar{f}$=1.061

4.1.5 Other Findings on Quartz

It is worth noting there is a tendency of cracks to form on quartz after laser irradiation. After some sets of laser experiments on quartz, we observed a particular crack growth direction. The micromachining project on quartz was started by Tom Snyder for his undergraduate thesis and it is worth showing a part of his results to show the reproducibility of this current research.

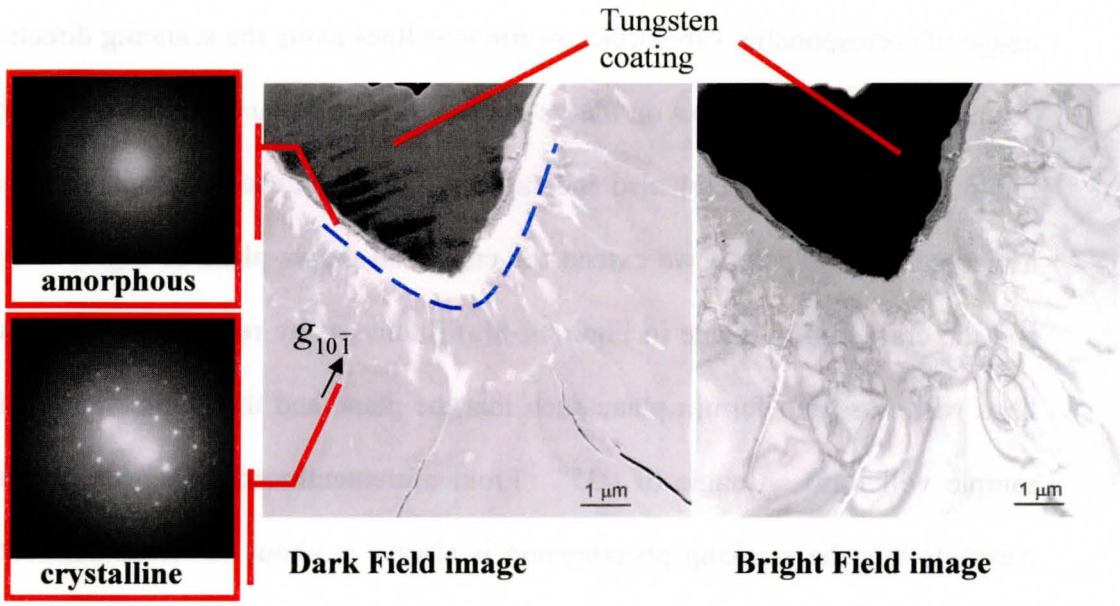

Figure 4-11: TEM images with dark field and bright field methods are showing the cross-section of surface continuous line created using a 5× microscope objective, 400 nm laser wavelength, 170 fs pulse duration, 5 μJ pulse energy, and 1 kHz repetition rate (Undergraduate thesis of Tom Snyder).

Figure 4-5(a) is a cross-section image of surface continuous lines that we produced in our current research (conducted with 800 nm laser wavelength) and investigated with the FIB method. Figure 4-11 shows TEM images of a cross-section of a surface continuous line from Tom Snyder's work (conducted with 400 nm laser wavelength). Both of the laser wavelengths are below the quartz bandgap. Thus we expect the surface of irradiated area to be similar except for the spatial periods of the observable surface features will change. Both cross-section images [Figure 4-5(a), indicated with red circles, and Figure 4-11] show the cracks at about 45° from horizontal axis. Figure 4-6(a) is a cross-section SEM

image of sub-surface continuous lines (yz-plane) and Figure 4-8(a) is a TEM image of corresponding sub-surface continuous lines along the scanning direction (xy-plane). Both the cracks on the yz-plane and the xy-plane [Figure 4-6(a) and Figure 4-8(a) respectively] also indicate the cracks extend at about 45° from horizontal axis. Then, if we extend the cracks on the yz-plane in Figure 4-6(a) and the cracks on xy-plane in Figure 4-8(a) (indicated by red circles), the crack lines will cross and form a plane such that the plane and the C-direction of the sample will form an angle of ≈35°. From aforementioned evidences, we can conclude that the cracking phenomenon is always at about 45° from horizontal axis in experiments performed with the same sample with the C-direction parallel to the laser propagation with respect to the sample. In order to understand the following hypothesis about the cracks existence on particular planes, Figure 4-12 is presented to illustrate the quartz crystal.

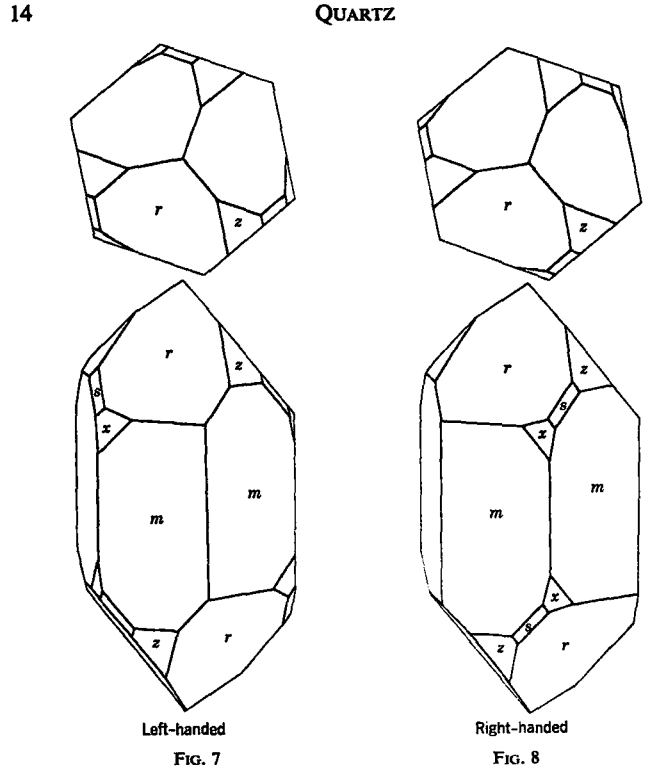

Figure 4-12: The view of quartz crystal (Diagram from [92]).

One publication has stated that there is no cleavage plane in quartz [20]. However, another publication not only concluded that there is a cleavage plane in quartz, but there are several cleavage planes [92]. The cleavage plane is not ordinarily observed in quartz and is not easily obtained by fracturing crystals through mechanical impact. However, the cleavage plane will appear when there is thermal shock and/or highly localized or confined pressure, especially the cleavage plane on $m\{10\bar{1}0\}$. It has been observed on the following seven planes:

$r\{10\bar{1}1\}$, $z\{01\bar{1}1\}$, $m\{10\bar{1}0\}$, $c\{0001\}$, $a\{11\bar{2}0\}$, $s\{11\bar{2}1\}$, and $x\{51\bar{6}1\}$ that the smoothest cleavage planes are those on r, z, and m planes. Of these three forms, the rhombohedral cleavage planes are smoother and easier to produce than that on the prismatic planes. The cleaving plane on r is smoother and apparently more readily produced than that on z. However, r and z cleavage planes have sometimes been described as equivalent with rather rough and interrupted feature [92]. Our earlier investigations show that the cracks on the cross-section of the surface line and sub-surface line appeared at approximately 45° from the horizontal axis (the specimens were oriented with the C-axis of the quartz crystal parallel to the laser propagation direction). This cracking phenomenon on quartz shows an agreement with the literature [92] that the cracks will most likely propagate along the r, z, and m cleavage planes. The angle between $C[0001]\text{-}r\{10\bar{1}1\}$ and $C[0001]\text{-}z\{01\bar{1}1\}$ is ≈35° and between $C[0001]\text{-}m\{10\bar{1}0\}$ is 0°. These calculated angles (r and z cleavage planes with C-axis) are in agreement with the 35° angle in our experiment investigations. We can deduce that the cracks mostly prefer to propagate on the r and z cleavage planes in quartz.

The cracking phenomena induced by laser irradiation are very pronounced in quartz compared to other materials in this thesis (sapphire and diamond). Based on Molecular Dynamics (MD) simulations [17], laser irradiation of materials with femtosecond pulses leads to a very high pressure in the interaction volume. This pressure drives a strong compression wave into the cold part of the

material and in the opposite direction, causing ablation and strong acceleration of product species [17].

In the femtosecond regime, the laser will introduce very high energy intensity that can knock out free electrons from their parent atoms. This high intensity leads to the multiphoton absorption (MPA) phenomenon in materials. Additionally the laser energy will induce electron-phonon coupling, generating local strain to the lattice and hence cause distortion in the lattice [19]. As a consequence, the local structure will be disturbed and result in some localized energy states within the band gaps. The free electrons in the conduction band can be trapped in such localized states and leave a hole in the conduction band. Such a trapped electron with a weakly interacting hole forms a quasi-particle, called self-trapped exciton (STE). The STE formation is accompanied by a strong distortion of the SiO_2 lattice [115]. This strong distortion weakens the lattice bonding and thus induces severe fracture in the remaining material [17]. The STE phenomenon has been used to explain the fracture mechanism on wide bandgap materials or insulators [116], such as SiO_2 [115] and CaF_2 [117].

4.2 Analysis on Sapphire

4.2.1 Single Pulse Ablation Experiment

Figure 4-13 shows a single pulse ablation experiment [X1] on sapphire with laser parameters E = 10 μJ, $\Phi = 25$ J/cm^2, τ = 190-200 fs, λ = 800 nm, using

5× microscope objective (a) in vacuum and (b) in air environment. From Figure 4-13 we can see that there is material splattered from the periphery of the crater Some cracks are evident in the middle of the crater that may caused by the pressure that is induced by femtosecond laser or formed during solidification.

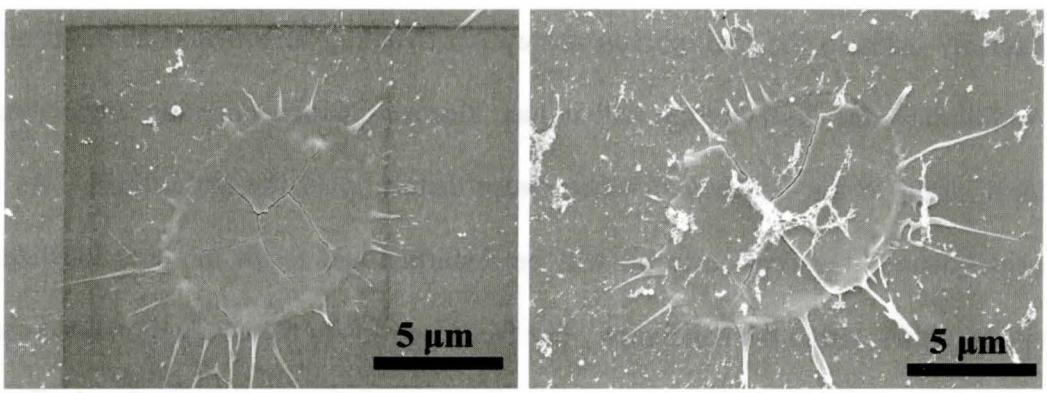

(a) In vacuum (b) In air

Figure 4-13: Single pulse ablation experiment on sapphire shows crater from $\Phi = 25$ J/cm^2, N = 1, $\tau = 190$ fs, $\lambda = 800$ nm, left = in air, right = in vacuum.

The D^2 analysis was performed on the single pulse ablation experiment with different laser energies on sapphire. By plotting squared diameter D^2 as a function of logarithm of laser energy, as shown in Figure 4-14, the slope yields to a spot size ω_0 4.5 µm (in vacuum) and the extrapolation of the slope to zero yields to a modification threshold $\Phi = 4.8$ J/cm^2 The graph in Figure 4-14 shows quite smooth data points in sapphire that contribute to the slope. The expected and experimental measurements of the spot size are in an agreement.

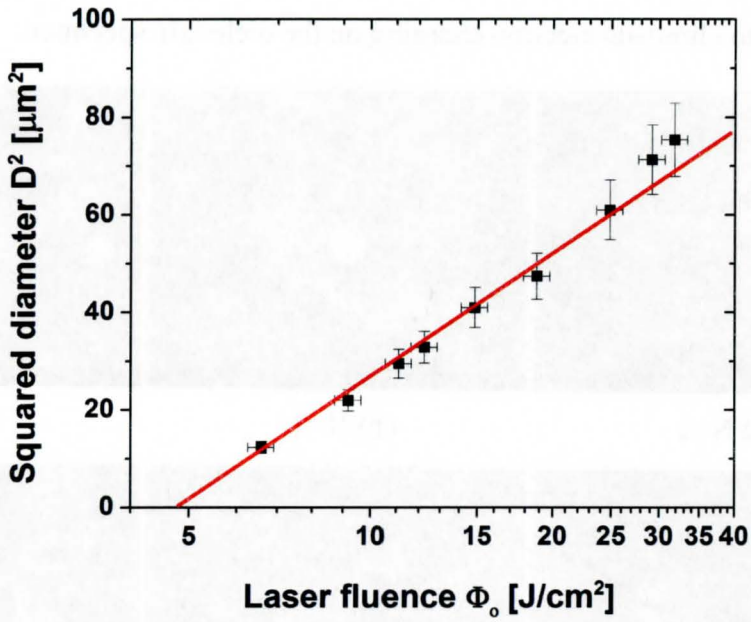

Figure 4-14: Squared diameter of the single pulse crater as a function of laser fluence where solid line shows linear square fit of the data points and is extrapolated to $D^2 = 0$ to obtain single pulse threshold of sapphire, yield to spot size ω_0 of 4.5 μm and 4.8 J/cm^2. This experiment was performed in vacuum using laser energy of 10 μJ and 5× microscope objective.

4.2.2 Plural Pulse Experiment

Plural pulse ablation experiments [X2] were done on 215 μm thickness, 3 mm diameter sapphire windows and investigated with an SEM JEOL 7000F Figure 4-15 shows SEM images of single pulse ablation craters in low vacuum with different number of pulses (a) N=1 (b) N=2 (c) N=3 (d) N=4 (e) N=5 (f) N=7 (g) N=10. This experiment was conducted at 10 μJ laser energy with 190-200 fs pulse duration and $\Phi = 31.2$ J/cm^2 The images below were taken with the secondary electron detector of the SEM JEOL 7000F at higher acceleration

voltage of 5 keV and higher A thin layer of about 25 Å thick platinum coating was applied to eliminate electron charging on the dielectric specimen.

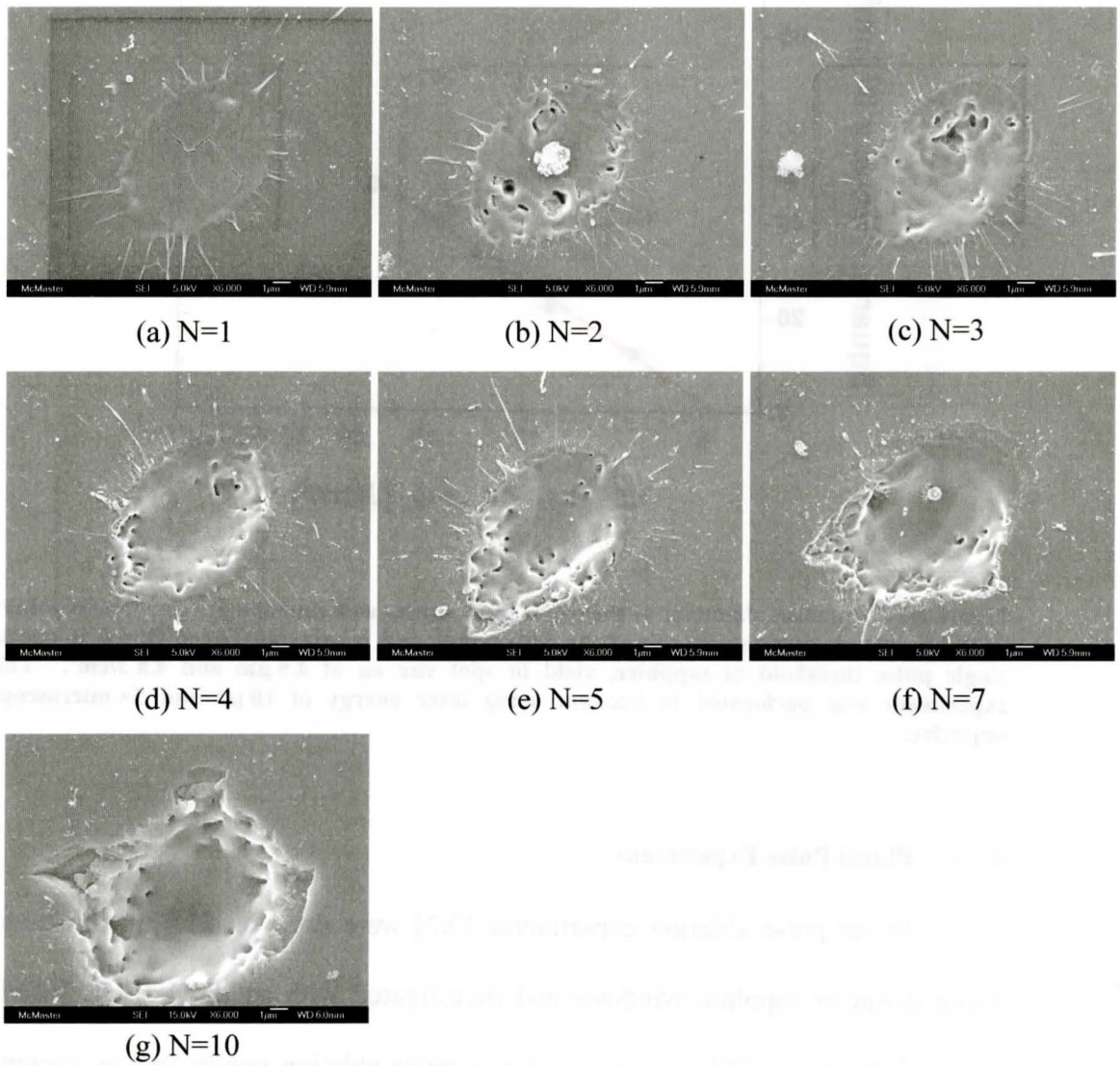

(a) N=1 (b) N=2 (c) N=3

(d) N=4 (e) N=5 (f) N=7

(g) N=10

Figure 4-15: SEM images of single pulse ablation on sapphire in low vacuum (a) N=1 (b) N=2 (c) N=3 (d) N=4 (e) N=5 (f) N=7 (g) N=10 with 10 μJ laser energy, 190-200 fs pulse duration, Φ = 31.2 J/cm^2.

As seen in the SEM images above, sapphire still behaves like a brittle material under femtosecond laser, indicated by cracks on the center of the crater

even with single pulse ablation. The cracks may be due to fast solidification after melting. Material is splashed from the center and redeposited to the edge of the crater. With an increasing number of pulses, the crater becomes deeper and the damage is more severe at the edge of the crater. After the first pulse, holes formed in the craters. The edge of the crater is chipped away after some subsequent pulses introduced. The crater diameter does not change significantly until 10 consecutive pulses. With increasing number of pulses, shallow craters and splattered forms at the edge of the crater were replaced by deeper craters, larger diameter and more severe damage at the edge due to material chipping.

4.2.3 Multiple Pulses Ablations Experiment

Figure 4-16 shows SEM images of 20 consecutive pulses on the same spot with decreasing laser energy [X3]. Sapphire with hardness of 9 Mohs, behaves as a more brittle material than quartz, indicated by more pronounced chipping and cracking at relatively low energy. The cracks propagate from the edge of the crater outward at higher fluence. The cracks can be growing up to three times the radius of the original crater and also exist at the bottom of the crater as shown in the inset for higher magnification. With decreasing fluence, the laser pulses modify the surface of the material further indicated by ripples formation.

We can see the ripples develop from the edge to the center of the crater with decreasing fluence. The experiment with 20 consecutive laser pulses showed that with high energy, the ablation mechanism is dominant. A tendency to form

ripples with specific spacing on the surface of the material is revealed with decreasing energy and increasing consecutive laser pulses. A lower pulse energy modifies the material further because such pulse energy is not high enough to strongly ablate the materials. When we introduce fluence lower than the single pulse threshold of 4.8 J/cm^2 in consecutive pulses, materials ablation is less pronounced than material modification. The consecutive pulses in this case modify the surface. In sapphire we observed the sub-wavelength ripples with the spacing of about 310 nm, this spacing is slightly larger than $\Lambda = \frac{\lambda}{2n(\lambda/2)} = \frac{800}{2\times 1.787} = 225nm$ [108]. Wortmann et al [31] observed nanostructures in the bulk of sapphire with the spacing about 300 nm with fiber chirped amplifier (FCPA) IMRA μJewel laser operated at a central wavelength of 1045 nm and a pulse duration of 400 fs.

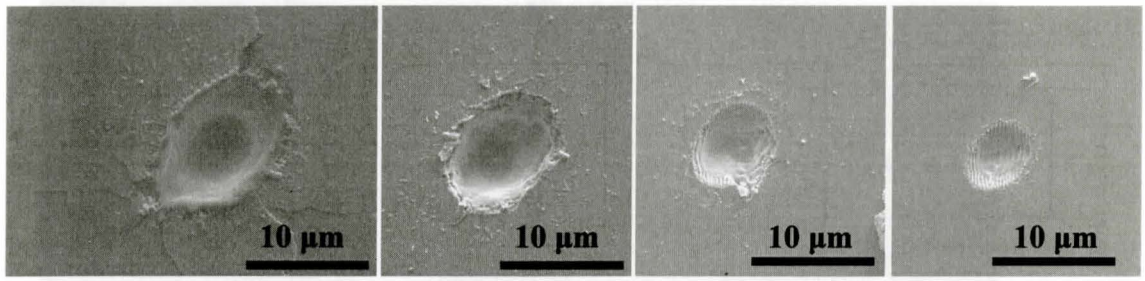

(a) 10 μJ (25.6 J/cm^2) (b) 6 μJ (15.2 J/cm^2) (c) 2.9 μJ (7.4 J/cm^2) (d) 1.6 μJ (4.1 J/cm^2)

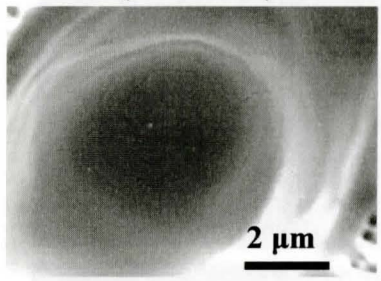

(e) A higher magnification of (a)

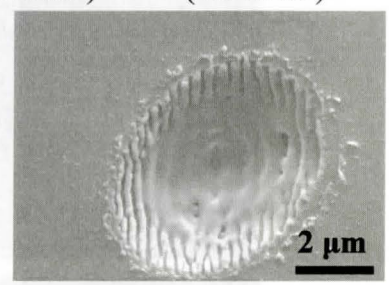

(f) A higher magnification of (d)

Figure 4-16: SEM images of craters introduced by femtosecond laser on sapphire with λ = 800 nm, τ = 190 fs, N=20 on one location.

Figure 4-17 is the matrix of SEM images of the multiple pulses ablation experiment [X4]. The laser processing was performed with specific laser energy of 10.0, 7.87, 4.70, 2.91 μJ and 5, 25, 50, and 100 consecutive pulses by changing the optical density filter manually

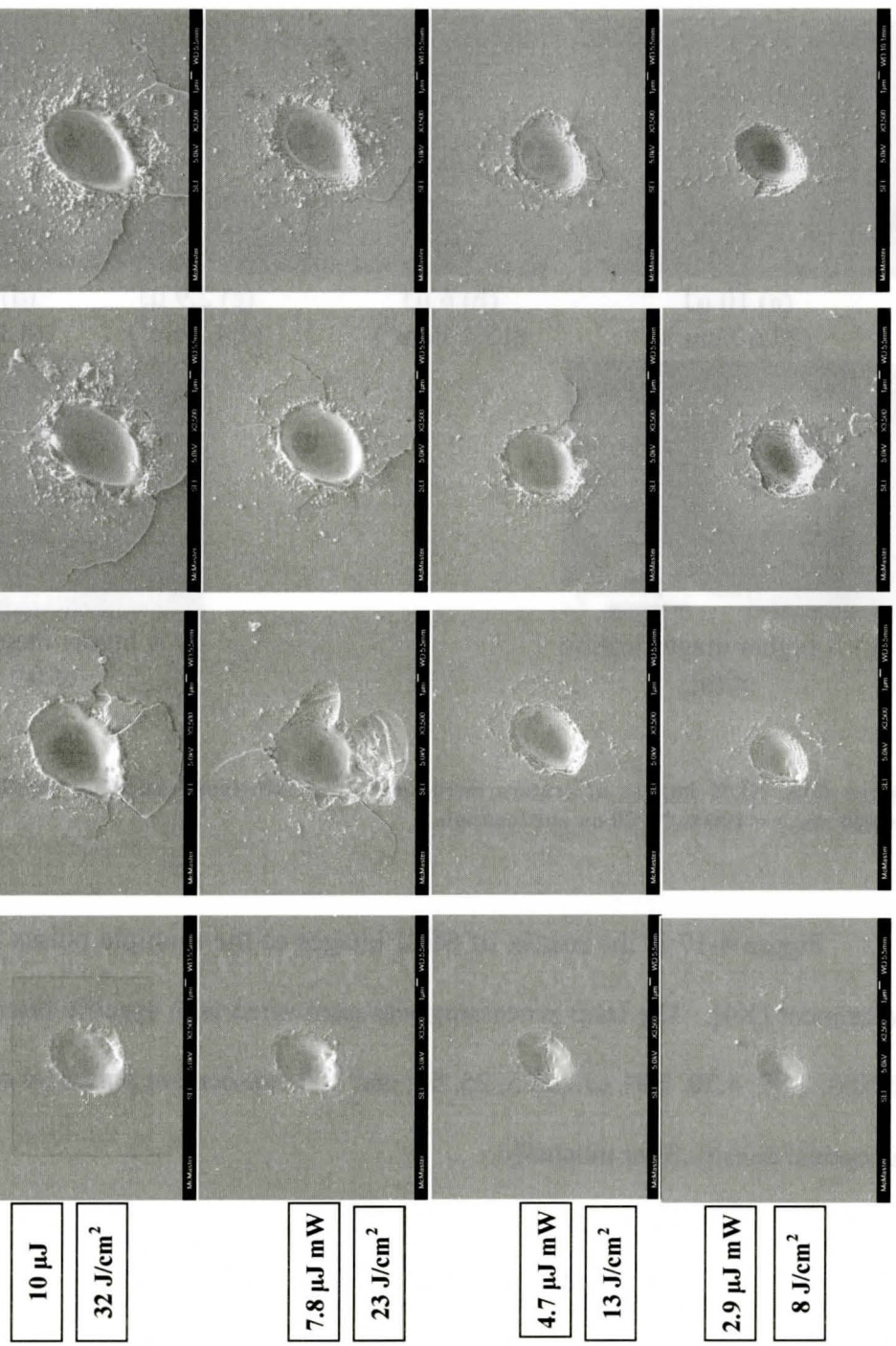

Figure 4-17: SEM images of multiple pulses ablation matrix on sapphire performed with 5, 25, 50, and 100 consecutive pulses.

The diameter of the crater increases with increasing laser energy. Higher numbers of consecutive pulses and energy that are introduced to the material make the crater deeper as indicated by more debris in the surrounding craters. Also, with higher laser energy, chipping & cracking become increasingly significant. The cracks can propagate far away from the crater. Just above the single pulse threshold fluence, minimal collateral cracking or chipping were observed while the surrounding surface remains in the original condition.

The modification threshold fluence for multiple pulses for sapphire can be explained with an incubation model [118]. The modification threshold fluence $\Phi_{mod}(N)$ for N pulses is related to the $\Phi_{mod}(1)$ for $N=1$ by a power law

$$\Phi_{mod}(N) = \Phi_{mod}(1)N^{\xi-1} \qquad \textbf{Equation 4-2}$$

ξ represents the degree of incubation in the material. For $\xi=1$, the modification threshold fluence is independent of the number of pulses, in other words the incubation is absent. From our measurements, the incubation coefficient of sapphire is $\xi = 0.84$. As depicted in Figure 4-18 the modification threshold decreases with increasing number of pulses.

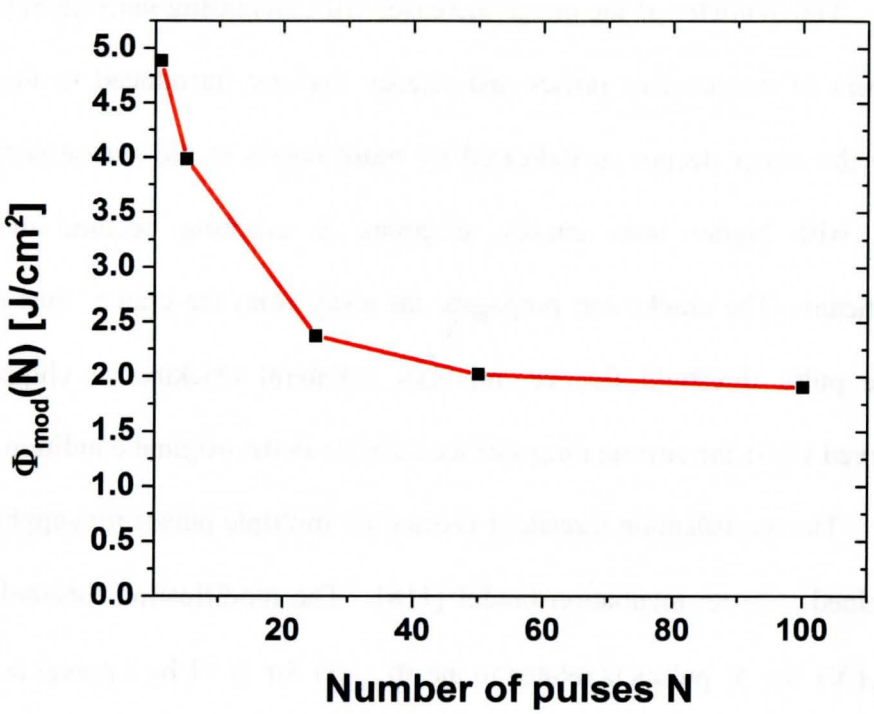

Figure 4-18: Plot of modification threshold fluence of multiple pulses on sapphire as a function of number of pulses.

Figure 4-19 shows the plot of the crater diameter as a function of number of pulses. The plot indicates that the crater diameter does not increase linearly with increasing number of pulses. Within the first 25 consecutive pulses, the increase of the diameter is very significant. That significant change in crater diameter shows the incubation behavior in sapphire. Consecutive laser pulses increase the number of defects and as a result also the absorptivity within the irradiated volume. The increase in energy absorption causes a decrease in Φ_{th} Thus Φ_{th} for multiple pulse ablation is lower than for single-pulse ablation

[Figure 4-18]. Briefly speaking, if Φ is just below Φ_{th} for single pulse ablation, ablation begins after a certain number of pulses. With further pulses, saturated conditions are obtained, indicated by the absence of significant increase in diameter between 25-100 consecutive pulses.

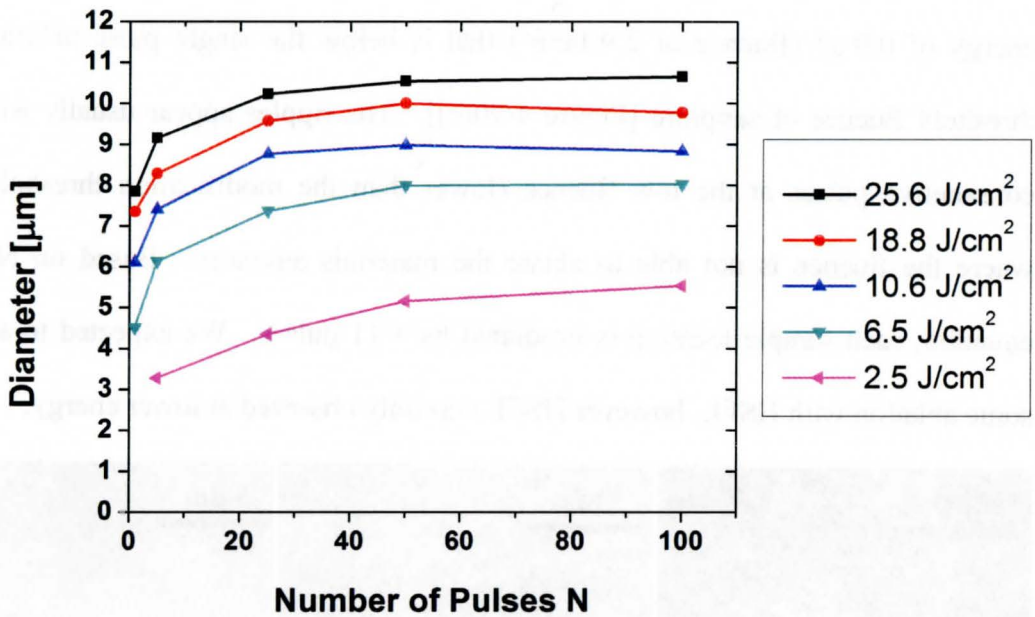

Figure 4-19: Crater diameter versus number of pulses for multiple pulses laser ablation on sapphire.

4.2.4 Surface Line Experiment

Figure 4-20 presents the surface continuous lines grating experiment [X5] that show different features with decreasing energy laser fluence. An energy of 5 µJ (fluence of 15.8 J/cm^2) produced droplet-like structures [Figure 4-20(a)] which did not indicate any preference direction relative to the electric field

polarization. With a lower energy of 2 μJ (fluence of 6.5 J/cm^2), close to the single pulse threshold of sapphire (4.8 J/cm^2), the sapphire develops overlapping path structure with a crosshatch structure at the edge of the groove [Figure 4-20(b)]. The width of the groove is slightly larger than the spot size of the laser beam of ≈4.5 μm as determined from D^2 method. Fine rippless appear with an energy of 0.9 μJ (fluence of 2.9 J/cm^2) that is below the single pulse ablation threshold fluence of sapphire [Figure 4-20(c)]. The ripples appear usually with consecutive pulses at the low fluence (lower than the modification threshold) where the fluence is not able to ablate the materials anymore. Based on N_{eff} equation, each sample location is irradiated by ≈ 11 pulses. We expected to see some ablation with HSFL, however HSFL was only observed at lower energy

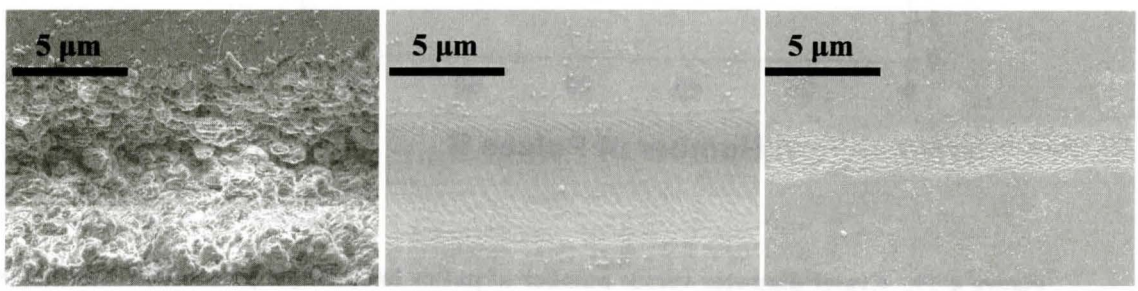

(a) 5 μJ (b) 2 μJ (c) 0.9 μJ

Figure 4-20: Surface line experiment on sapphire produces different structure with decreasing energy fluence (a) droplet-like structure (b) overlap path and cross-hatch structure (c) fine ripples.

A more general investigation of a series of continuous lines micromachining experiment was performed. Irradiation with pulse energies

below and beyond the threshold of sapphire leads to the formation of three different surface morphologies are listed in Table 4-3. This laser processing was conducted with a Newport-5× microscope objective. A different pulse energy was obtained using a different optical density filter. At higher fluence (≥ 8 J/cm^2), a droplet structure was observed. At the slightly higher and lower fluence than single pulse modification threshold (3 J/cm^2 $\leq \Phi \leq$ 6 J/cm^2), an overlapping path with crosshatch structure on the edge of the groove replaced the droplet-like structure. Lastly, as the fluence decreases even further ($\leq$2.5 J/cm^2), only fine ripples appear on the surface with spacing approximately 130 nm (close to $\Lambda = \frac{\lambda}{3n(\lambda/3)} = \frac{800}{3\times 1.832} = 145nm$ [108]).

Table 4-3: List of different features as a function of fluence.

Energy (μJ)	Line Width (μm)	Energy fluence (J/cm^2)	Feature
5.03	8.69	13.131	Droplets
4.52	8.39	10.789	Droplets
3.70	7.39	9.716	Droplets
2.70	7.03	7.999	Droplets
2.08	5.45	5.833	Overlap path + Crosshatched
1.71	5.15	4.489	Overlap path + Crosshatched
1.54	4.91	3.422	Overlap path + Crosshatched
1.27	4.36	3.081	Overlap path + Crosshatched
0.92	2.06	2.532	Ripple
0.71	Invisible	Invisible	Invisible
0.54	Invisible	Invisible	Invisible

4.2.5 Sub-surface Line Experiment

The sub-surface micromachining experiment [X7] was conducted on a well-polished cross-section sample at laser energy of 10 μJ, feed rate of 500 μm/s, using 50× microscope objective. Seven pairs of lines (fourteen lines) were created from the surface to a certain depth inside the bulk sapphire at seven gradual depth levels. Sub-surface line processing was performed on a 508 μm thick sapphire window. Considering the refractive index of sapphire (n=1.760 at a wavelength of 800 nm), a 40 μm increment will not damage the stage below the bottom of the sample. The horizontal distance between two adjacent sub-surface lines is 50 μm. Note that the previous sub-surface micromachining experiment was performed on an unpolished cross-section sample. After the micromachining process, some polishing steps were employed to prepare the cross-section sample. However, the expected damage region that was observed with the Nomarski microscopy was not observable under SEM on the first sample. Thus, we repeated the same experiment on the well-polished cross-section sample.

Figure 4-21 shows the seven pairs of sub-surface lines on sapphire. Sapphire does not show the double modified region seen in quartz in previous section [Figure 4-10]. However, the damage in sapphire was similar to longer damage in quartz. A comparison between the nominal focal point of the laser beam that has 40 μm step size along z-axis (z=0 is on the surface) and the actual top positions of the damage region yields a factor of 1.6. Similarly, a comparison between the nominal focal point of the laser beam and the actual middle position

of the damage region yields a factor of 2. The refractive index of sapphire is n=1.762-1.778. So the calculated factors are slightly below and above the refractive index of sapphire. The detailed comparison above is tabulated in table Table 4-4.

Table 4-4: Comparison of the nominal focal point of the laser beam with respect to the top actual depth and middle actual depth of sub-surface damage region on sapphire.

Nominal focus (μm)	Index	Top actual depth z (μm)	Factor	Index	Middle actual depth z (μm)	Factor
40	A	46	1.150	A'	93	2.325
80	B	124	1.550	B'	160	2.000
120	C	193	1.608	C'	240	2.000
160	D	270	1.688	D'	323	2.019
200	E	357	1.785	E'	400	2.000
240	F	351	1.463	F'	477	1.988
			$\bar{f}$=1.602			$\bar{f}$=2.001

Based on the cross-sectional SEM image [Figure 4-21], the sub-surface modified regions average in length of ≈88 μm (B-G) whereas the modified region on the surface elongates ≈46 μm (A), which is approximately a half of the average length of sub-surface modified region. The calculated Rayleigh range, z_r, is about 55 μm or, in other words, the confocal parameter is about 110 μm. Compared to calculated confocal parameter of the laser beam, the modified region is 20% shorter. This phenomenon may be caused by self-focusing, spherical aberrations and/or propagation effects [13, 31, 119]. All the modified regions were introduced with a tight laser beam using 50× microscope objective (2.8 μm spot size) at center wavelength of 800 nm, 10 μJ laser energy, 79 J/cm^2 fluence and $N_{eff} \approx 7$.

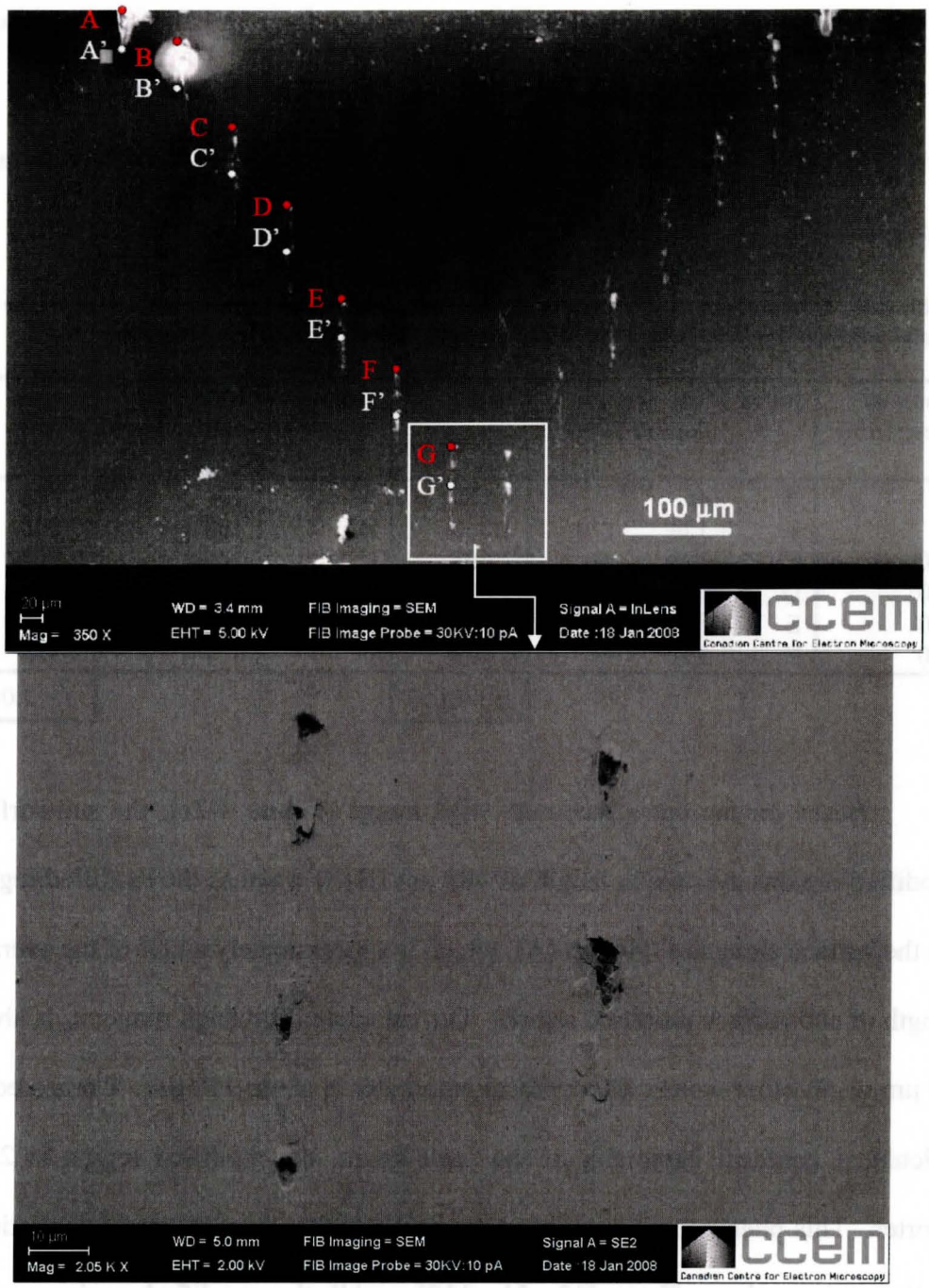

Figure 4-21: SEM image of sub-surface linear grating inside sapphire shows (a) the position of the sub-surface modified regions. The laser processing was conducted with an 800 nm wavelength, 50× microscope objective, 2.8 µm spot size, laser 10 µJ energy and 79 J/cm^2 fluence energy. The image was taken with In-Lens detector to get more pronounced feature (b) the higher magnification of selected modified region in (a).

Further investigation was performed by milling the cross-section of the sapphire with FIB milling. We tried to mill the specimen with different probes of 30 keV ions, in the range of 40 pA-6.5 nA, with and without XeF_2 gas assisted etching. The probe of 30 keV:3 nA had the best performance for coarse milling and 30 keV:40 pA for fine milling. The XeF_2 assisted etching yields smooth side walls and minimum material redeposition, however the milling process was slower. Nevertheless, we could not detect any evidence of phase transformation or sub-surface structure change in sapphire as in quartz. A suitable parameter of FIB milling on sapphire should be further investigated. Similar experiments inside the bulk sapphire observed sharp boundary between original crystalline and amorphous region [31, 35]. Micro- and nanostructures with the spacing about 300 nm inside sapphire by femtosecond laser irradiation were observed after 24 hours etching in HF by Wortmann et al [31]. Such feature was created with fiber chirped amplifier (FCPA) IMRA μJewel laser operated at a central wavelength of 1045 nm and a pulse duration of 400 fs. We were expecting to observe such structures without doing etching so that we could have the original information and feature after irradiation from the materials. However they mentioned that the observed structure was not well-organized. We were wondering if the nanoplanes in the bulk can only be observed after etching.

4.3 Analysis of Diamond

4.3.1 Single Pulse Ablation Experiment

Single pulse ablation processing was carried out with the maximum laser energy at 20 μJ and energy fluence of 78 J/cm^2, using a Newport-5× microscope objective. Figure 4-22 presents some SEM micrographs of single pulse ablation with different laser fluences [X1]. Diamond seems to have a very sensitive surface indicated by a very distinct and well-defined boundary of the crater at very low fluence. The higher laser energies of 20 μJ and 8 μJ (78 J/cm^2 and 33 J/cm^2 fluence) modified the crater into four different annular regions as shown in Figure 4-22 (a) and (b) respectively. For the lower laser fluence, the laser beam introduced relatively uniform damage from the center to the periphery of the craters until the smallest fluence that can damage the diamond surface. The damage areas introduced by lower laser energy of 2 μJ (8.6 J/cm^2) [Figure 4-22(c)] and 1 μJ (4.6 J/cm^2) [Figure 4-22(d)] are shown. The craters are relatively circular without indicating a significant difference in features from the center to the periphery.

The lower laser fluence that induced crater formation with the average diameter close to spot size of 3.9 μm, will be discussed in the next section of D^2 measurement on diamond. As expected, higher laser fluence induced a crater with the larger average diameter.

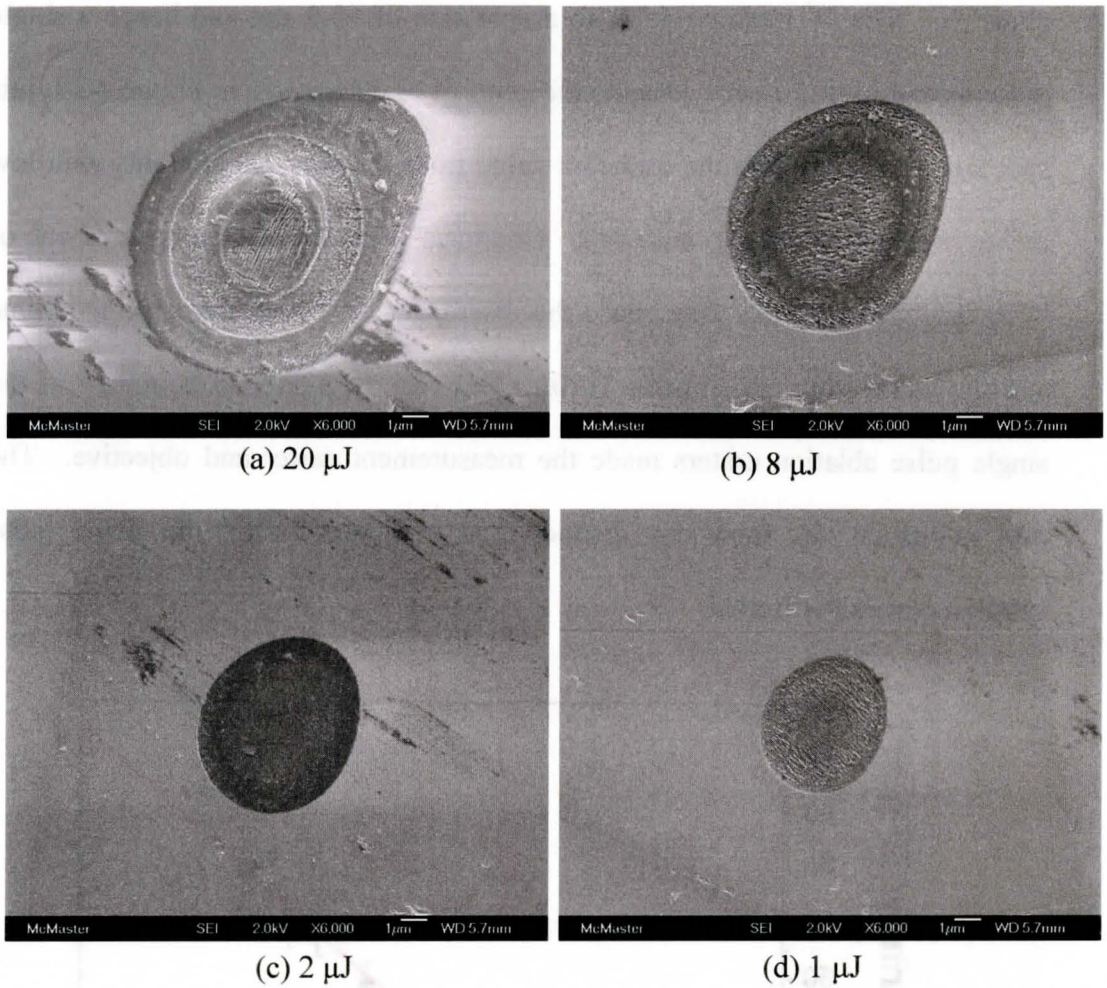

Figure 4-22: SEM images of single pulse ablation in diamond surface with different fluences (a) 20 μJ (b) 8 μJ (c) 2 μJ (d) 1 μJ.

Figure 4-23 presents a plot of squared diameter D^2 as a function of logarithm of laser fluence. The single pulse modification threshold was determined from series of single pulse ablation experiments with different pulse energy [X1]. The different pulse energy was obtained by changing the optical density filter. This laser processing was carried out with maximum laser energy of 20 μJ and a pulse duration of 141-153 fs, using a Newport-5×microscope

objective. The D^2 method yields to a spot size of ≈3.9 μm and hence a single pulse threshold of 2 J/cm^2 Despite the good fit of data points in Figure 4-23, this spot size is smaller than the expected value from previous experiments with low and/or moderate band-gap materials. Nonlinear behavior of diamonds as one of wide bandgap materials may cause the discrepancy between the expected value and the value from experiments [120]. The very well-defined boundary of the single pulse ablation craters made the measurement easier and objective. The data points do not show any distinct regime throughout all the single pulse ablation craters performed.

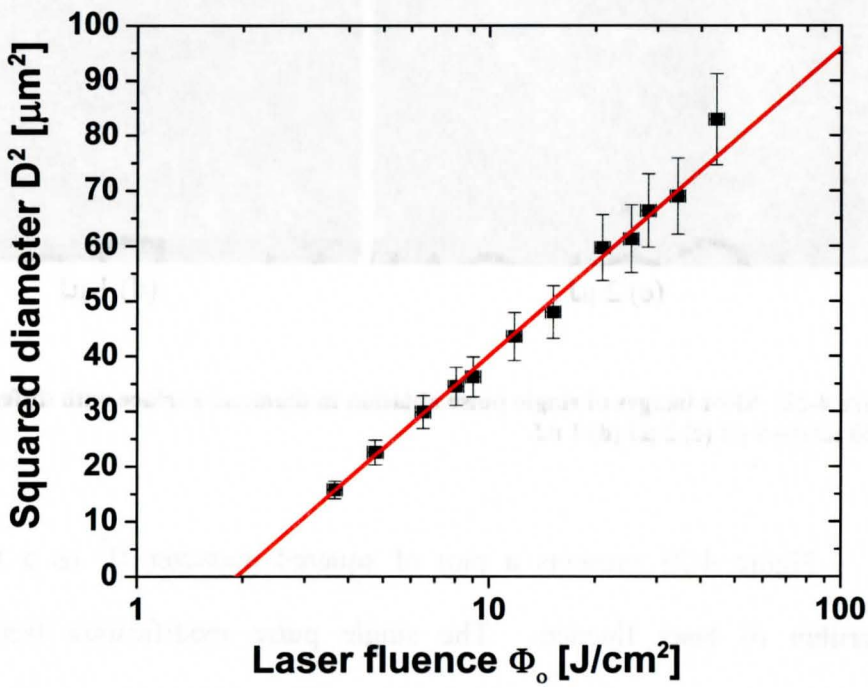

Figure 4-23: Squared diameter D^2 as a function of the logarithm of laser fluence on diamond, yield to spot size of ≈3.9 μm and hence the single pulse modification threshold of 2 J/cm^2

The calculated threshold fluence obtained from this experiment is smaller than Ramanathan et al, i.e. 4 J/cm^2 [121]. In their experiment, they use a smaller and tighter spot size of 3 μm. This discrepancy may be explained by the observation of Martin et al [95] that there is the spot size dependency of the ablation threshold in dielectric materials for femtosecond laser pulses. The threshold fluence was found to increase with decreasing spot size. Also, the discrepancy might be a result of the different experimental conditions and the uncertainty in the respective fluence determinations in the two laboratories.

4.3.2 Plural Pulse Ablation Experiment

Figure 4-24 shows a series of plural pulse ablation craters. The laser micromachining process [X2] was conducted at the maximum laser energy of 20 μJ and fluence of 78 J/cm^2, using a Newport-5× microscope objective. The plural pulse ablation experiment with N=1-10 on diamond represents the gradual damage morphology. As seen on Figure 4-24, the periodic surface structures or ripples start to be clearly identified in terms of spacing at 3 consecutive pulses. The ripples are growing from the center to the edge of the craters. The ripple spacing for each crater from N=3 until N=10, is reasonably consistent with other ultrashort pulse works, i.e. 600 nm on average. The ripples posses relatively uniform spacing from the center to the edge. The orientation of the ripples is perpendicular to laser polarization direction. At the same laser fluence, the

periodicity of the ripples is more pronounced and well-defined with increasing number of pulses.

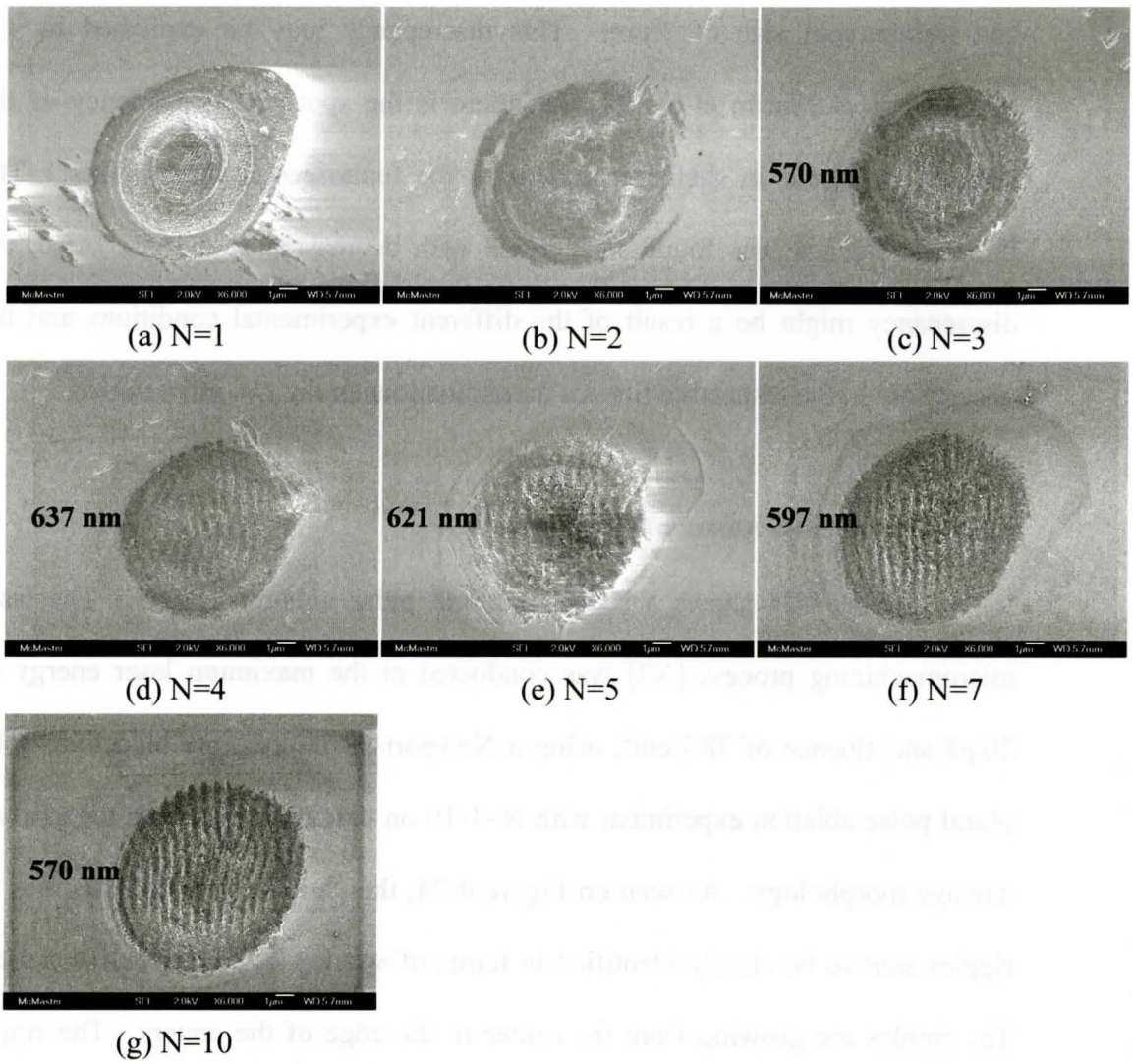

(a) N=1 (b) N=2 (c) N=3

(d) N=4 (e) N=5 (f) N=7

(g) N=10

Figure 4-24: SEM images shows the gradual morphology of the craters from N=1 to N=10 on diamond, the experiment was conducted at laser energy of 20 μJ and laser fluence of 78 J/cm^2, the ripple orientation are perpendicular to the laser polarization and the ripple spacing is ≈600 nm on average (the detail spacing measurement result for each crater is indicated by the bolded number in each image).

Figure 4-25 is the AFM images of the plural pulse ablation experiment. Contact mode AFM was employed because it has better topography recognition considering diamond is very hard so that the AFM tip will not scratch the original features.

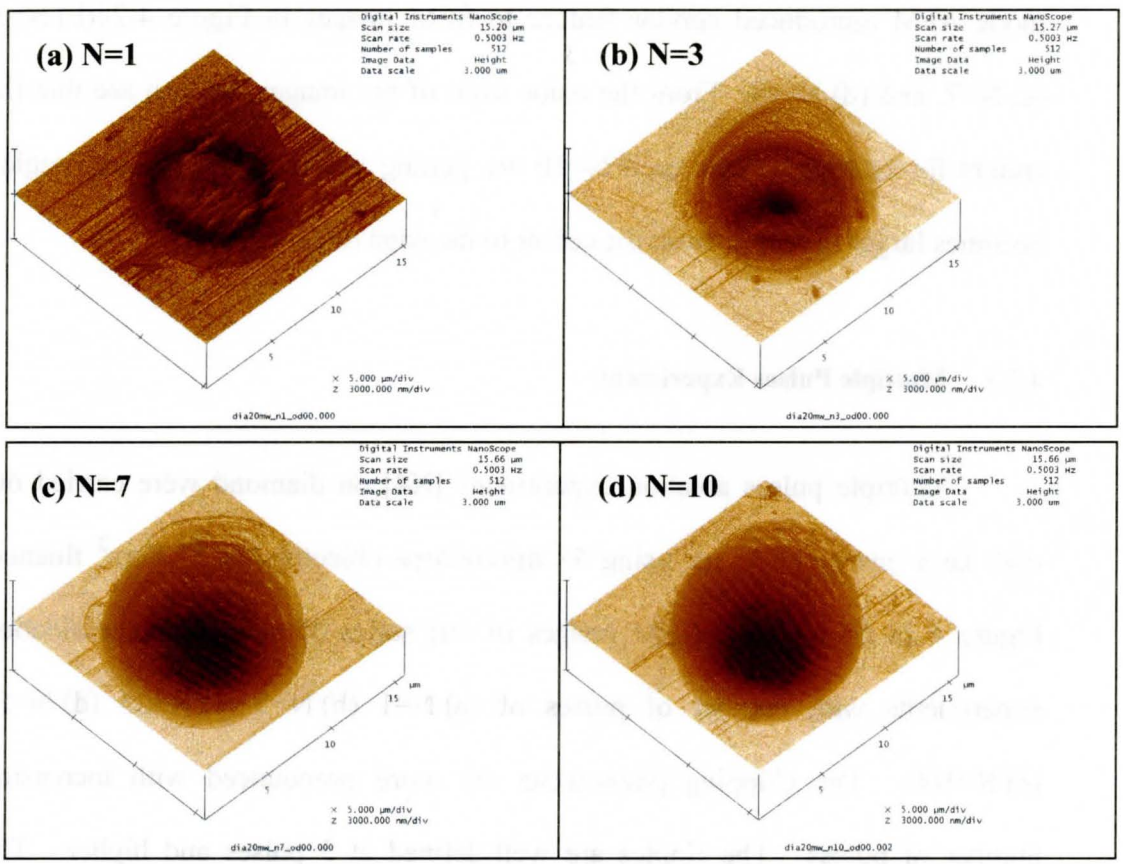

Figure 4-25: 3D AFM images of plural pulses ablation on diamond surface with (a) N=1 (b) N=3 (c) N=7 (d) N=10.

As shown in the Figure 4-25(a) an investigation of single pulse ablation using contact mode AFM is not representative since it has different features to the corresponding SEM image in Figure 4-24(a). The AFM tip dragged the material

on the surface of the crater. The four different rings observed in SEM image for N=1 [Figure 4-24(a)] could not be obtained with AFM investigation. The only information we can get from that AFM image is that single pulse ablation creates relatively flat crater as indicated by very uniform color scale. However, contact mode AFM reproduced similar feature to SEM images in Figure 4-24(b) N=3, (c) N=7, and (d) N=10. From the color scale of the images, we can see that the craters for multiple pulses until N=10 are getting deeper. The periodic region becomes larger in radius, from the center to the edge of the crater.

4.3.3 Multiple Pulses Experiment

Multiple pulses ablation experiments [X4] on diamond were carried out with laser energy of 15 μJ, using 5× microscope objective, at 57 J/cm^2 fluence. Figure 4-26 shows some SEM images of one series of multiple pulse ablation experiments with number of pulses of (a) N=1 (b) N=5 (c) N=25 (d) N=50 (e) N=100. The chipping phenomena are more pronounced with increasing number of pulses. The ripples are well-defined at 5 pulses and higher. The craters look deeper after further subsequent pulses in the center of the crater. Two types of ripple co-exist at pulses of N=25-100. The ripple spacing in the center is about 555 nm (between $\Lambda = \lambda = 800nm$ and $\Lambda = \frac{\lambda}{n(\lambda)} = \frac{800}{2.397} = 335nm$ [122])

on average and on the edge is in the range of 115-215 nm (close to

$$\Lambda = \frac{\lambda}{2n(\lambda/2)} = \frac{800}{2 \times 2.463} = 160nm \text{ [122])}$$

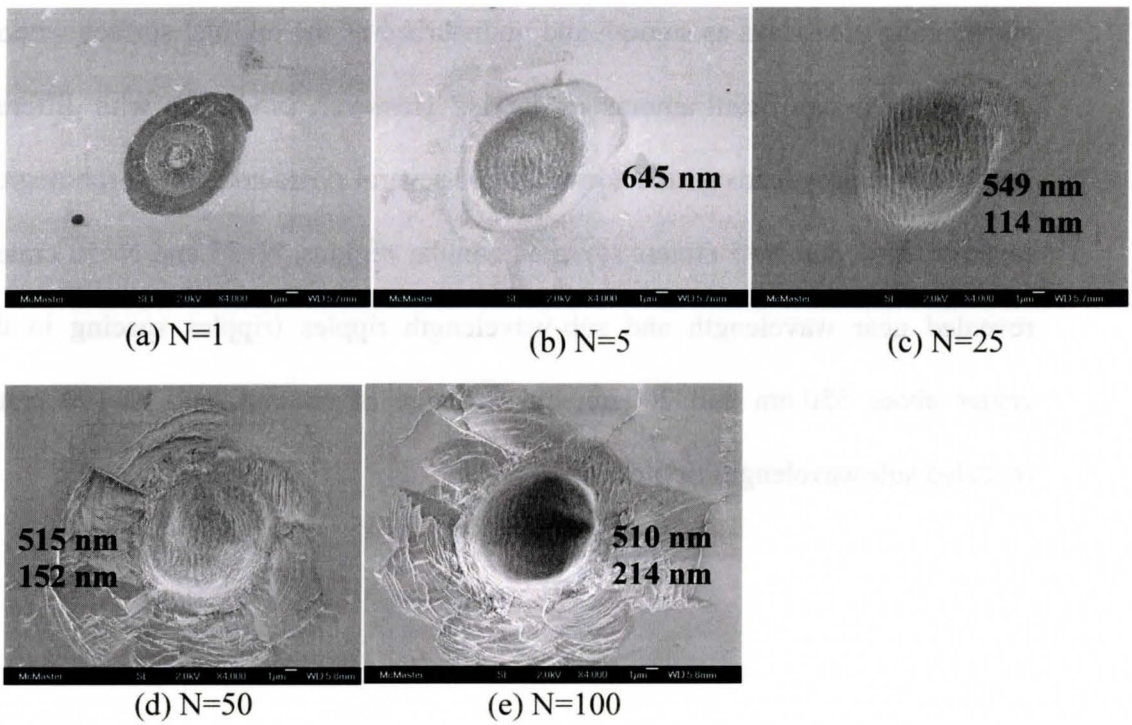

(a) N=1 (b) N=5 (c) N=25

(d) N=50 (e) N=100

Figure 4-26: SEM images of multiple number of pulses on diamond surface using 5× microscope objective, at laser energy of 15 μJ (fluence of 57 J/cm^2) with number of pulses of (a) N=1 (b) N=5 (c) N=25 (d) N=50 (e) N=100 (the detail spacing measurement result for each crater is indicated by the bolded number in each images, the bigger spacing was observed in the middle of the crater and the smaller spacing was observed in the outer part of the crater).

An investigation of the multiple pulse ablations experiment similar to the experiment above but with lower energy fluence was also carried out to understand damage morphology qualitatively Figure 4-27 represents SEM images of multiple number of pulses performed with a 5× microscope objective,

laser energy of 2 μJ (fluence of 7.70 J/cm^2) and (a) N=1 (b) N=5 (c) N=25 (d) N=50 (e) N=100.

The lower energy of 2 μJ caused a very minute ablation area. The surrounding area stays as smooth and undisturbed as the original surface without chipping or a significant amount of debris. However, irradiation with different number of pulses leads to the formation of several characteristic morphological regions. N=1 and N=5 craters revealed annular regions, N=25 and N=50 craters revealed near wavelength and sub-wavelength ripples (ripples spacing in the center about 550 nm and 200 nm on the edge of craters), and N=100 crater revealed sub-wavelength ripples.

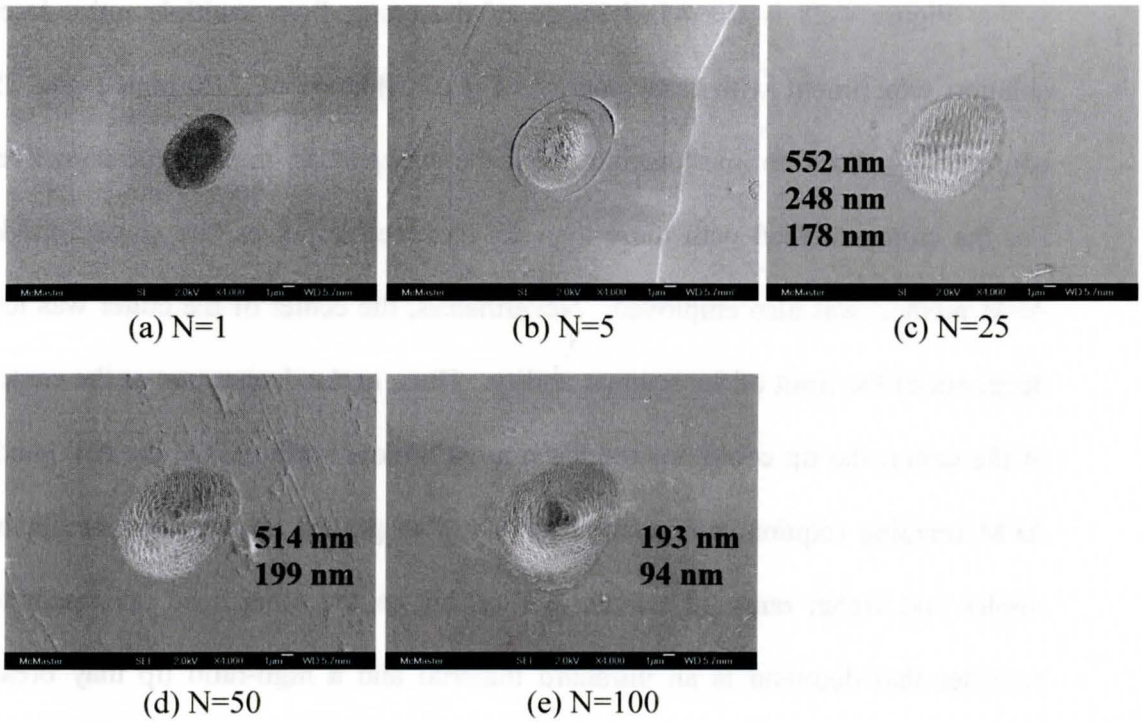

(a) N=1 (b) N=5 (c) N=25

(d) N=50 (e) N=100

Figure 4-27: SEM images shows multiple pulse ablation on diamond surface with a 5× microscope objective and laser energy of 2 μJ (fluence of 7.70 J/cm^2) for number of pulses on one location (a) N=1 (b) N=5 (c) N=25 (d) N=50 (e) N=100 (the detail spacing measurement result for each crater is indicated by the bolded number in each images, the bigger spacing was observed in the middle of the crater and the smaller spacing was observed in the outer part of the crater).

Ozkan et al and Wu et al [22, 24] observed the LIPSS on diamond surface with near wavelength and sub-wavelength spacing. In Ozkan et al [22] observation, it was seen ripples with intermediate spacing due to the out-of-phase superposition of electromagnetic fields from the laser pulses. They hypothesized that the scattered wave is not only produced by the light interference, but also by a thin waveguide etched on the surface.

Figure 4-28 is the AFM image of the crater from multiple pulse laser ablation experiment with laser energy of 2 μJ (fluence of 7.70 J/cm^2) and 25 consecutive pulses on one location using the Newport 5× microscope objective. For the crater induced with more than 25 consecutive pulses, the contact mode AFM method was also employed. Nevertheless, the center of the crater was too deep, out of the limit of the scanner ability. Thus, in the deeper part at the center of the crater, the tip could not reach the most bottom surface. On the one hand, AFM imaging requires a high ratio AFM tip to get the spacing and height of ripples and higher range of scanner ability, but on the other hand one needs to consider that diamond is an ultrahard material and a high-ratio tip may break within a short time.

For contact mode AFM imaging, it is indispensable to have a cantilever which is soft enough to be deflected by very small forces (i.e. small force constant) and has a high enough resonant frequency to not be susceptible to vibrational instabilities. Thus, a short and thin cantilever was selected to provide a high resonant frequency and a small force constant respectively. A smaller cantilever must also be selected when the sample is prone to damage.

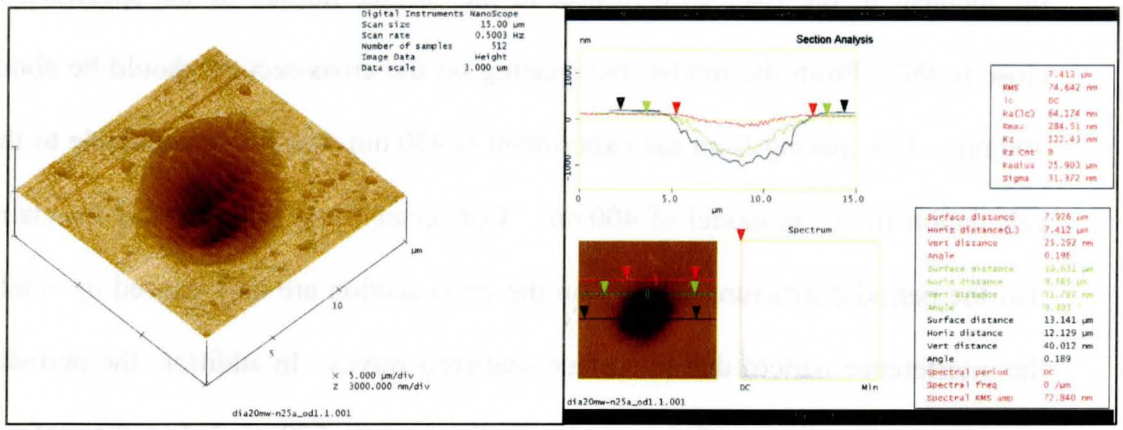

Figure 4-28: AFM images of a crater from a multiple pulse ablation experiment on diamond surface with laser energy of 2 µJ (fluence of 7.7 J/cm^2) and N=25 on one location, using Newport 5× microscope objective.

4.3.4 Surface Line Experiment

Surface line experiments [X5] on a diamond sample were performed with laser energy of 23 µJ, fluence of 62.9 J/cm^2, with Newport-5× microscope objective and a spot size of ≈3.7 µm shown in Figure 4-29 The scanning direction is from the x-positive to the x-negative and the electric field polarization is parallel to the x-axis. We are wondering if femtosecond laser pulses are able to modify the surface as well as the sub-surface as indicated by periodic surface structure perpendicular to the electric field polarization. The average spacing of the periodic surface structure on the surface is 585 nm in the middle of the groove and 140 nm at the edge of the groove while the average spacing of the periodic structure on the cross-section of the sample is 450 nm. If we assume that the periodic structure on the cross-section is caused by the incident beam, the angle of

the incident of the laser with respect to the surface normal of the specimen is close to 90°. From the model, the spacing on the cross-section should be about 400 nm. The spacing from the experiment is 450 nm which is comparable to the calculation from the model of 400 nm. Conversely, it is subjective if we claim that the periodic structure features on the cross-section are only caused by solely the interference pattern due to surface scattered waves. In addition, the periodic structure on the cross-section extends very long, up to 100 μm below the surface, and does not show finer ripples on the edge. The fluence introduced by the laser beam deep below the surface will be very small compared to that at the focal point on the specimen surface and should not give a uniform feature from the top to the bottom of the cross-section. The results of Ozkan et al [22] demonstrate laser writing is not only on the 2D surface but also 3D features. We used 500 μm thick of CVD diamond windows. Due to cutting and/or sectioning difficulty of these samples, we could not investigate the large cross-section from diamond sample. It also considers the lateral dimension of the diamond windows compared to the thickness of cutting tool compensation. From the edge of diamond we can see the edge of the sample was also modified by the laser beam. The question from this case is: Is it possible that laser beam can modify the materials (diamond) far away from the beam focal plane? And is there another possible mechanism that allow laser to modify the materials in such way? The ripples formation and the spacing in this case were not easily explained with the classical ripple theory. We may also take into account harmonics generation and

the materials properties (such as SEW that is propagating inside the material and not above) in the ripples formation mechanism and the spacing [123].

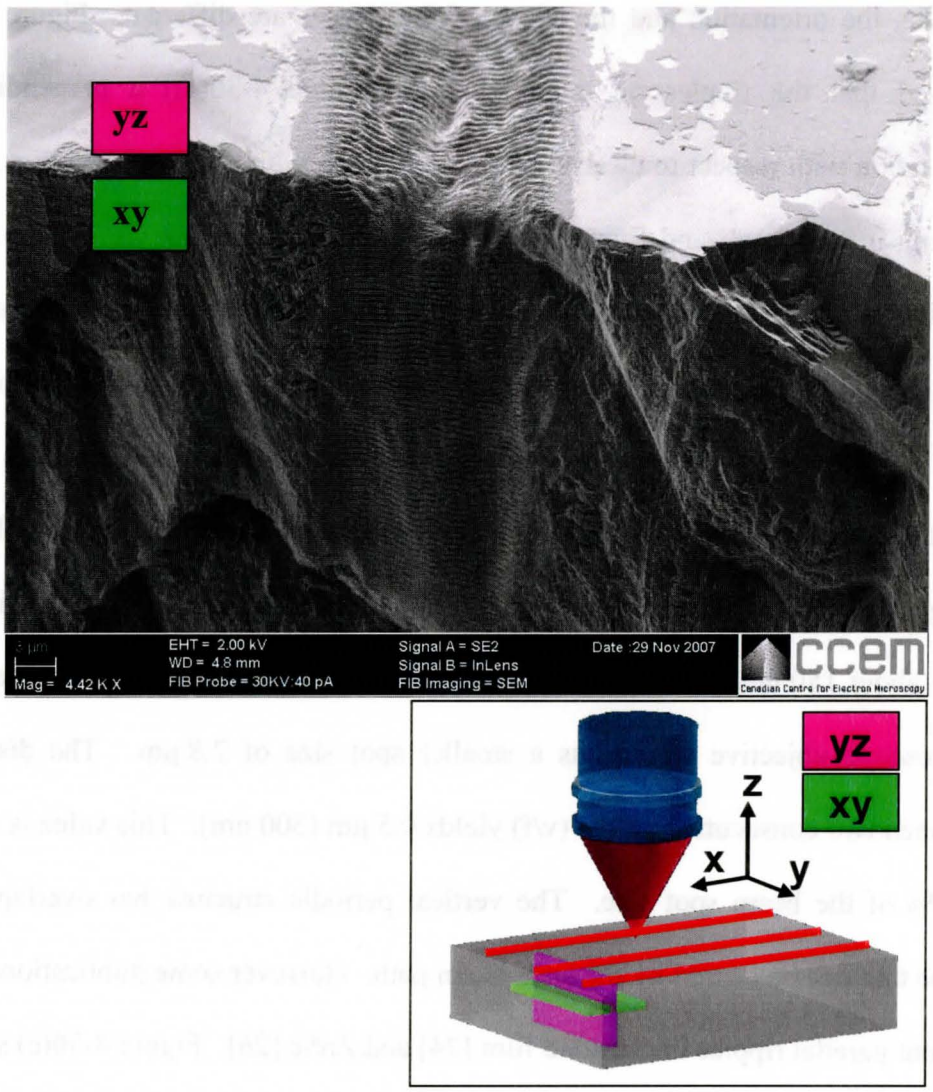

Figure 4-29: Surface continuous line on the diamond surface with laser energy of 23.7 μJ (fluence of 62.9 J/cm^2) with Newport-5× microscope objective. The scanning and electric field polarization is on the x-axis, periodic surface structure on the surface as well as in sub-surface is perpendicular to the electric field polarization. The laser was scanned from the x-positive to the x-negative.

Diamond gives various responses with respect to the electric field polarization and laser irradiation. In Figure 4-30 from left to right, with similar fluence, the orientation and the shape of the ripples are different. Figure 4-30 showed that the ripples on diamond have [Figure 4-30(a)] a perpendicular orientation with respect to electric field polarization with spacing varying coarser spacing in the center and finer spacing on the edge of the groove. The coarser spacing is about 700 nm and 555 nm in the center and the finer spacing at the edge is about 165 nm and 90 nm. This surface line experiment was performed with a Newport-5× microscope objective. Figure 4-30(b) shows ripples with parallel and perpendicular orientation with respect to the laser polarization. In the image, the horizontal ripples have about 460 nm spacing and the vertical ripples have about 150 nm spacing. This second experiment was performed with a 50× microscope objective which has a smaller spot size of 2.8 μm. The distance between two consecutive pulses (v/f) yields 0.5 μm (500 nm). This value is about 17.5% of the beam spot size. The vertical periodic structure has overlap path shape that can be caused by the laser beam path. However some publications also present parallel ripples in diamond film [24] and ZnSe [26]. Figure 4-30(c) shows ripples that are perpendicular with respect to laser polarization with uniform spacing about 600 nm. This third experiment was done with a Newport-5× microscope objective.

From these series of experiment, we observed that polycrystalline diamond revealed varied surface features (spacing, morphology, and orientation)

resulting from similar laser fluence and different electric field polarization direction.

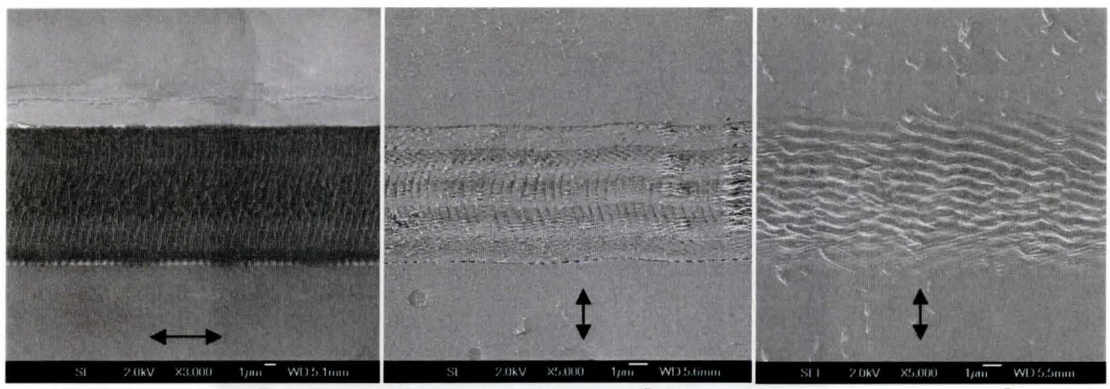

(a) 6.8 J/cm^2 (b) 5.6 J/cm^2 (c) 6.2 J/cm^2

Figure 4-30: SEM images show varied ripples on diamond with almost similar laser fluence, arrows indicate the electric field polarization direction (a) ripples perpendicular orientation with respect to laser polarization with varied spacing from the center to the edge (b) parallel and perpendicular with respect to laser polarization (c) perpendicular with respect to laser polarization and uniform spacing

The tendency to form periodic structures in diamond is very strong. Figure 4-31, Figure 4-32 and Figure 4-33 show broad variation of the surface periodic structure in term of spacing, morphology and orientation. The LIPSS on surface lines on diamond shows coarse and fine spacing. As shown in Figure 4-31, from the center to the edge of the groove indicates classic LIPSS with the spacing of 700 nm and 555 nm that are close to laser wavelength, indicated by $\Lambda = \lambda = 800nm$ and finer spacing near the edge are about 165 nm (close to $\Lambda = \frac{\lambda}{2n(\lambda/2)} = \frac{800}{2 \times 2.463} = 160nm$ [122]), indicating second harmonic generation ripples, and finally, the finest spacing at the very edge 90 nm (close to

$\Lambda = \frac{\lambda}{3n(\lambda/3)} = \frac{800}{3\times 2.599} = 100nm$ [122]), indicating third harmonic generation ripples.

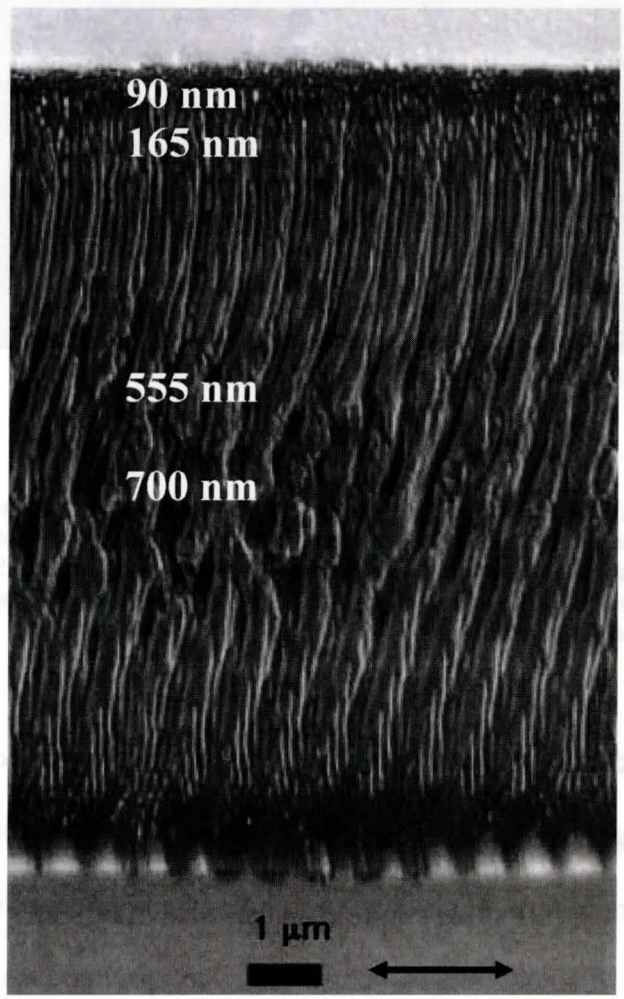

Figure 4-31: SEM image of surface line on diamond with laser energy of 2.6 μJ (≈6.8 J/cm^2) shows ripples with wide variation of spacing; the coarser spacing are about 700 nm and 555 nm in the center that close to laser wavelength λ, the finer spacing near the edge is about 165 nm close to second harmonic generation Λ=λ/2n, and the finest spacing at the very edge is about 90 nm close to third harmonic generation Λ=λ/3n.

Figure 4-32 shows a surface line on diamond with laser energy of 24 μJ (fluence of 63 J/cm^2). It shows ripples with wide variation of spacing; the coarser spacing is about 585 nm in the center that is close to the laser wavelength λ and the finer spacing at the edge is about 140 nm close to second harmonic generation $\Lambda = \frac{\lambda}{2n}$. In the middle of the groove, finer ripples are superimposed with coarse ripples. Wu et al [24] observed the short periodicity LIPSS (Λ≈210 nm) perpendicular to the laser polarization was superimposed on the long perpendicular LIPSS (Λ≈750 nm).

The periodicity of the ripples is influenced by the surface morphology and roughness [22]. The random orientation of the LIPSS in Figure 4-33 may appear due to the rough surface from previous consecutive pulses. These previous pulses damaged the surface and such damage became an initiator of new orientation LIPSS.

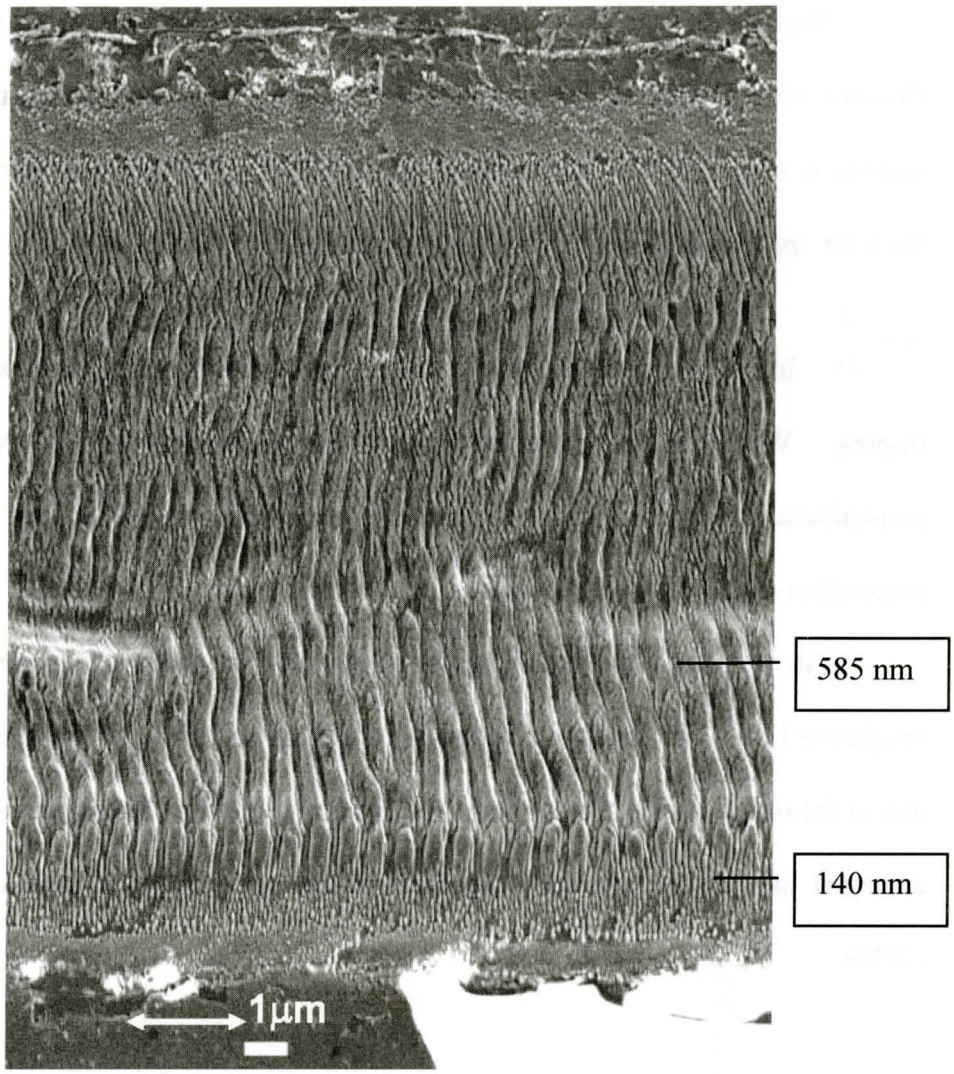

Figure 4-32: SEM image of a surface line on diamond with laser energy of 24 μJ (63 J/cm^2) fluence shows ripples with wide variation of spacing; the coarser spacing is about 585 nm in the center which is consistent to the laser wavelength Λ=λ=800 nm and the finer spacing at the edge is about 140 nm, close to second harmonic generation Λ=λ/2n.

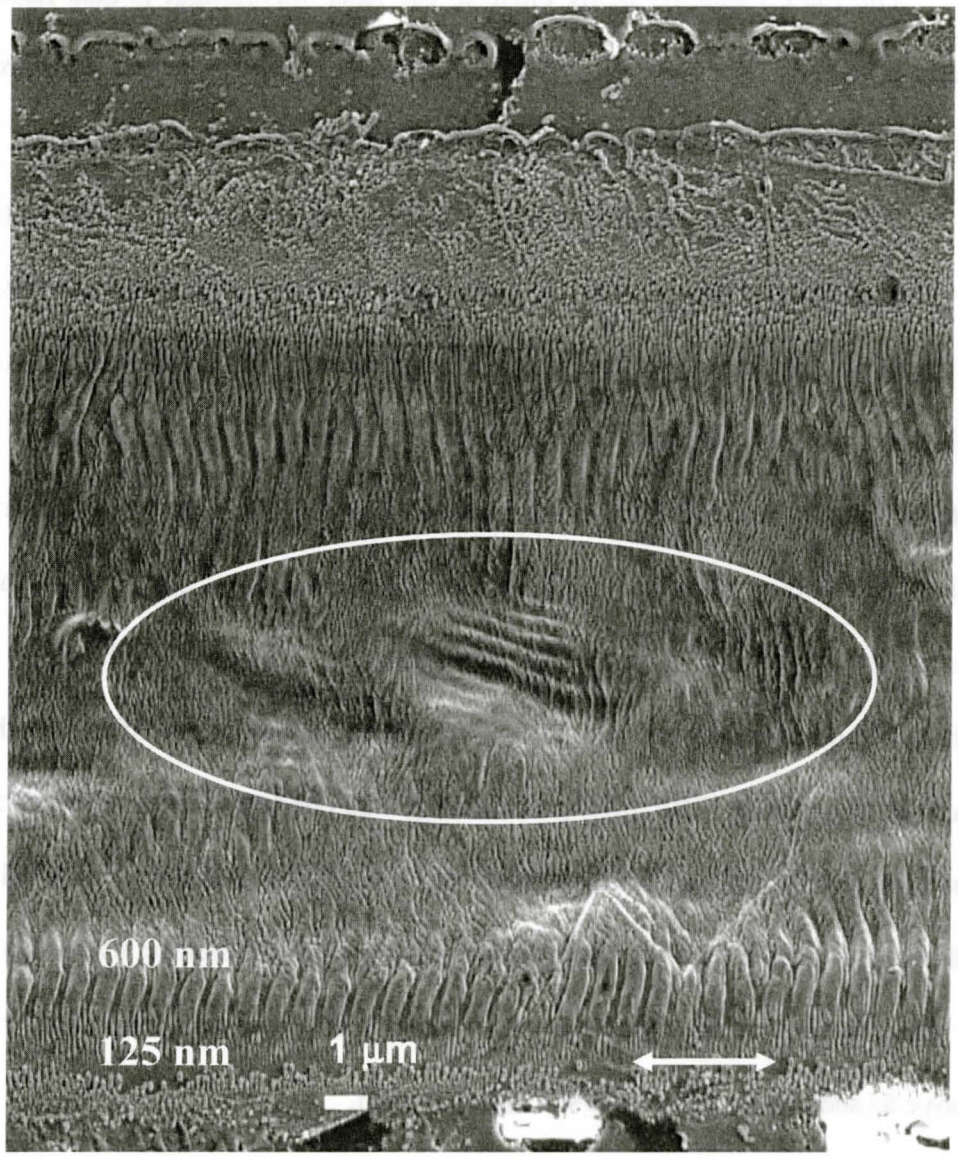

Figure 4-33: SEM image of surface line on diamond with laser energy of 32 μJ (85 J/cm^2) shows very fine ripples at the edge of groove and coarse ripples next to the fine ripples. In the middle of the groove appear random orientations of ripples, superimposed with the existence of fine ripples (in circle).

The LIPPS spacing being close to the laser wavelength is also noted by Ageev et al [65], Dumitru et al [124] and Ozkan et al[22] in the laser treated diamond film with the orientation perpendicular to electric field polarization.

In order to understand the groove profile we need to do sectioning to get the cross-section of the groove. A conventional cutting with diamond saw was not possible due to the dimensions of the sample and limitations of the cutting tools. So we used Focused Ion Beam (FIB) with Ga^+ ions to mill away some material locally perpendicular to the groove. Figure 4-34 is the result of milling with FIB. This groove was made with laser parameter of 32 μJ laser energy, fluence energy of 84.9 J/cm^2 with a Newport-5× microscope objective. By milling the cross-section of the groove, we can get a rough idea of the depth and shape of the groove. The milling processing was conducted with a 30 keV:3 nA probe for coarse milling and then followed by a 30 keV:300 pA for fine milling, without gas assisted etching. Because of redeposition and melting by the Ga^+ ion, the fine features of the cross-section could not be obtained. The depth of the groove as seen in the Figure 4-34 is about 3.4 μm.

To investigate sub-surface structures, different probes sizes ranging from 30 keV:80 pA to 30 keV:6.5 nA and also varying the etching gas between XeF_2 and H_2O were used. The gas-assisted etching produces smooth sidewalls in the milled area. However, the expected sub-surface structure has not been observed. More suitable FIB milling parameters should be further investigated in order to be able to observe sub-surface structures and to prepare TEM sample.

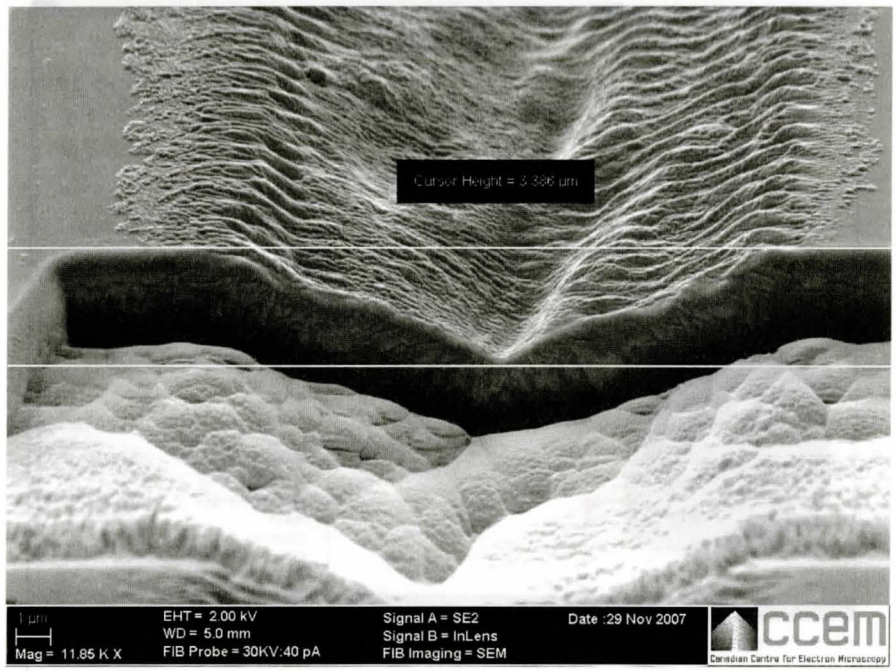

Figure 4-34: SEM+FIB image shows milled cross-section of the groove to get the depth of the groove made by 32 µJ, fluence energy of 84.9 J/cm^2 and a Newport-5× microscope objective.

An AFM investigation was performed to obtain additional information about the topography and geometry of the surface lines on diamond. Figure 4-35 shows AFM images and section analysis of a surface line that was conducted at 2.2 µJ laser energy (9.0 J/cm^2 laser fluence). With such low pulse energy, the depth of the groove reached approximately 660 nm (compare to the depth of the groove with higher laser energy in Figure 4-34), the spacing of the periodic surface structure or ripples is about 700 nm, which close to laser wavelength and the height of a single ripple is about 130 nm.

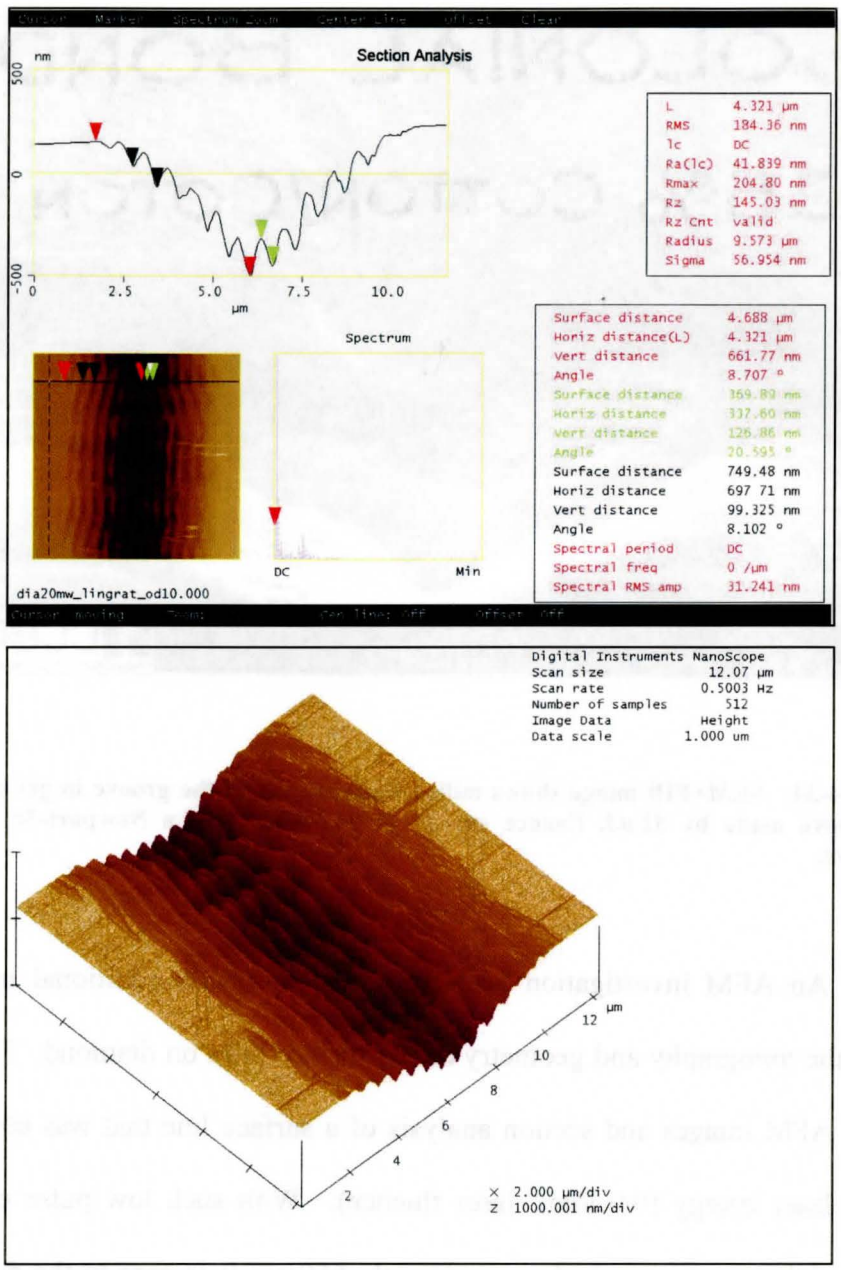

Figure 4-35: AFM images and profile of a surface continuous line created with 2.2 µJ laser energy and 9.0 J/cm^2 fluence. Note the different scale for the z-axis in the groove profile.

4.3.5 Sub-surface Line Experiment

A sub-surface lines irradiation in diamond was created using a laser energy of 3.77 μJ, fluence of 29.7 J/cm^2 and a 50× microscope objective. We created 7 pairs of sub-surface continuous lines with 50 μm horizontal distance between two adjacent lines. Considering the refractive index of diamond is n=2.42, we used 30 μm increments of the laser beam focal point from the surface down into the diamond bulk (z=0 on the surface), in order not to make a damage exceeding the bottom of the sample.

Figure 4-36 is the SEM+FIB images of the sub-surface linear grating on CVD diamond windows. We have not been able to mill the cross-section of overall sample as we have done on quartz and sapphire in the previous sub-section [Figure 4-10 and Figure 4-21] due to the diamond sample dimensions. However we were able to see the first three pairs of continuous lines with the In-Lens detector [Figure 4-36(a) and (c)]. Moreover, we were also able to see the bottom most two pairs of sub-surface continuous lines [Figure 4-36(d)]. We are wondering if tightly focused femtosecond laser pulse can modify the material up to the surface from the evidence of quite long elongated modified areas. In order to obtain more information about the sub-surface continuous lines in the diamond bulk, we performed FIB investigations by milling the specified area. Unfortunately, throughout this study, we have not been able to determine suitable FIB milling parameters for polycrystalline CVD diamond window.

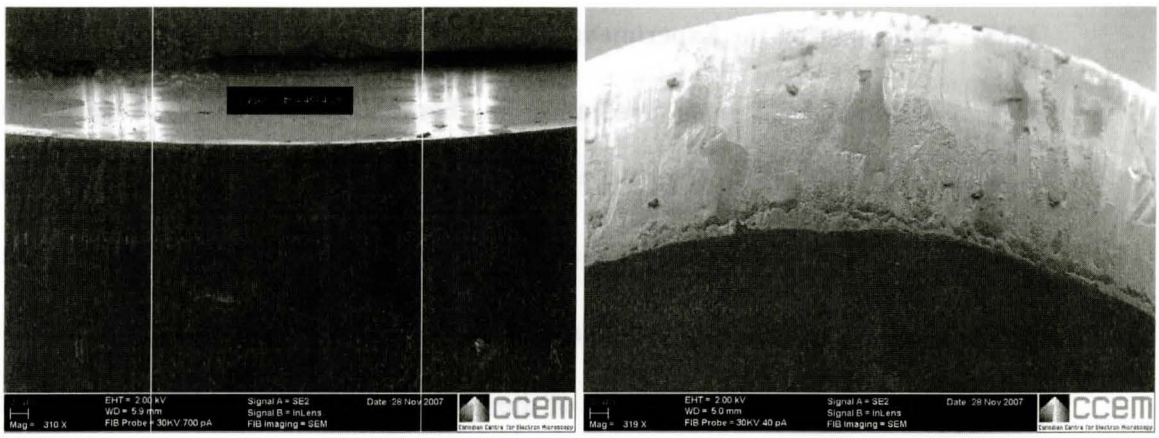

(a) Bird's eye view (b) Worm's eye view

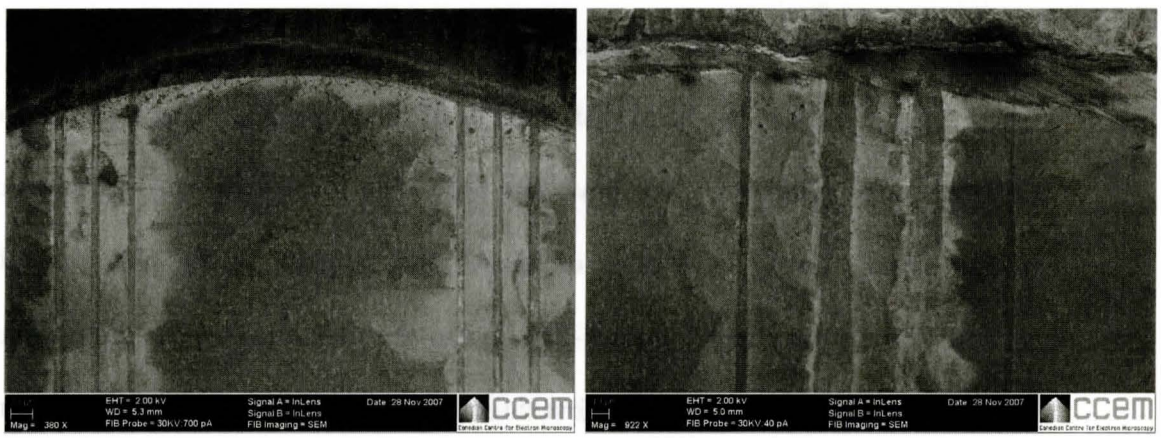

(c) Top view (d) Bottom view

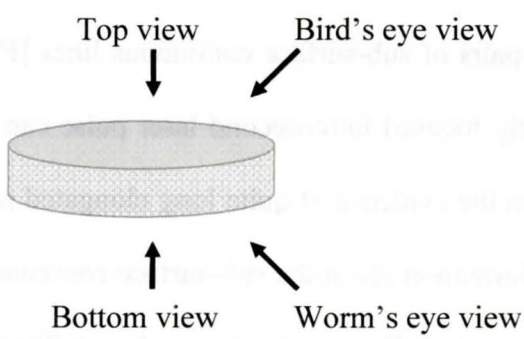

Figure 4-36: SEM+FIB images of the subsurface linear grating on a polycrystalline CVD diamond window (a) three pairs of linear gratings are visible with SE2 detector (b) cross section of CVD diamond windows (c) Three pairs of linear gratings (d) The most bottom two pairs of linear gratings

In order to estimate the length of the modified region along z-axis, first, we can calculate the confocal parameter of the laser beam. The spot size of ≈2.8 μm and the laser wavelength of 800 nm, yields a Rayleigh range of ≈77 μm or confocal parameter of ≈154 μm. Considering the refractive index of diamond, we can predict the focal plane of the beam as indicated with red boxes in Figure 4-37. From Figure 4-36, we have the information of the lines widths and positions at the top and the bottom surfaces. The modified areas are represented as grey boxes with their corresponding width [Figure 4-37]. Hence, the prediction of the length of the elongated modified areas respective to their focus is at least about 290 μm (depicted with blue arrows). The length of the elongated modified are is about twice the calculated confocal parameter.

This simple speculation is just to estimate the length of possible modified region from the focal plane. If this was the case, one should be careful when applying femtosecond laser pulses to machine diamond since the modified area is quite long from the focal plane.

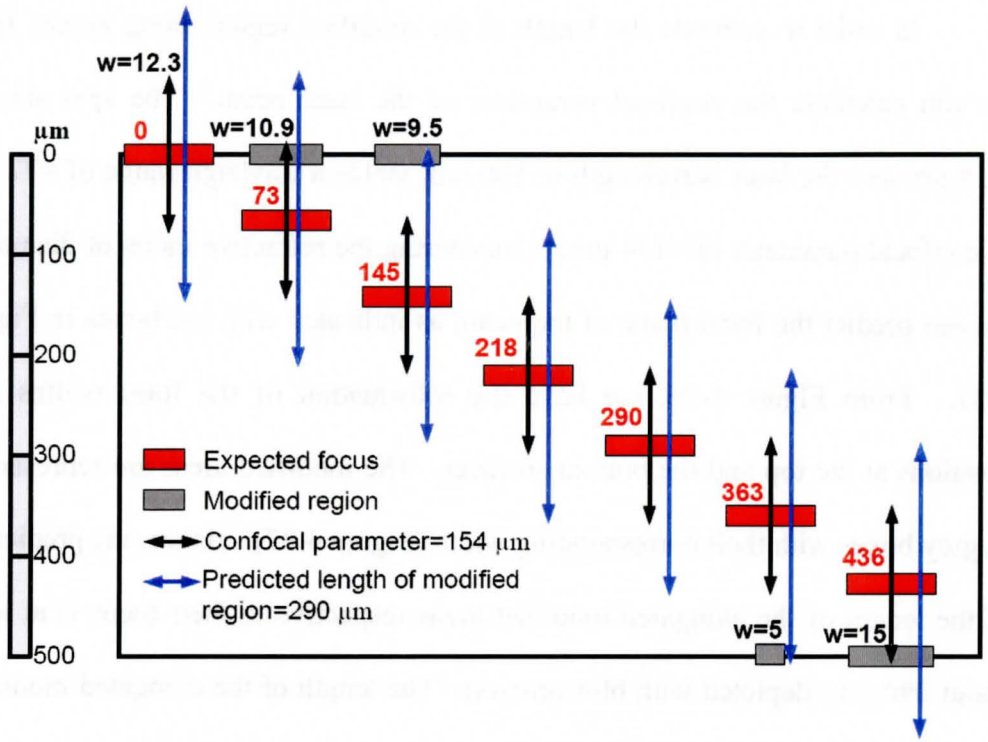

Figure 4-37: The modified length prediction scheme of the sub-surface continuous lines in diamond. Red boxes and numbers depict the positions of expected focal point based on the refractive index of diamond, grey boxes and numbers in black depict the modified region that are seen from top and bottom surfaces, black arrows depict the laser confocal parameter in diamond and blue arrows depict the predicted length of modified region. Note the chart above represents only a half of the diamond sample.

4.4 Comparison on Quartz, Sapphire, and Diamond

After presenting all the detailed results and discussions on each material employed in this study in previous sections (refer to section 4.1 to 4.3), it is worth to compare the results among them.

Firstly, we would like to compare the spot sizes of the Newport-5× microscope objective and modification thresholds of quartz, sapphire, and

diamond that were obtained from D^2 method. We suspected that this method did not work well for wide bandgap materials. An open question about the validity and reproducibility of the D^2 method came up after we obtained the different values of spot size from the different slope of the D^2 measurement of the three materials [Figure 4-38], where spot sizes for quartz, sapphire, and diamond are 3.7 μm, 4.5 μm, and 3.9 μm respectively and the threshold for quartz, sapphire, and diamond are 3 J/cm^2, 4.8 J/cm^2, and 2 J/cm^2 respectively. We confirmed these results by re-measuring the diameter of the single pulse ablation craters. Besides, we found inconsistencies in the spot size determination with this method and also our measurement results yielded a significant deviation from the expected spot size (based on the previous experiments using low bandgap materials, i.e., GaP=2.26 eV, InP=1.35 eV, and Silicon=1.11 eV). Since being proposed by Liu in 1982 [81], the D^2 analysis has been used as a practical way to determine the spot size and the modification threshold. However this technique is empirical due to a lack of information on the material properties (refer to sub-section 2.5.4). As materials have specific properties, they will behave distinctively. Also the fact that the laser beam parameters also changed over time due to positioning variations, the atmosphere of the laser laboratory, and the other possible technical reasons that may contribute to the quality of the laser beam time to time. These aspects may lead to variance in the measurements/results.

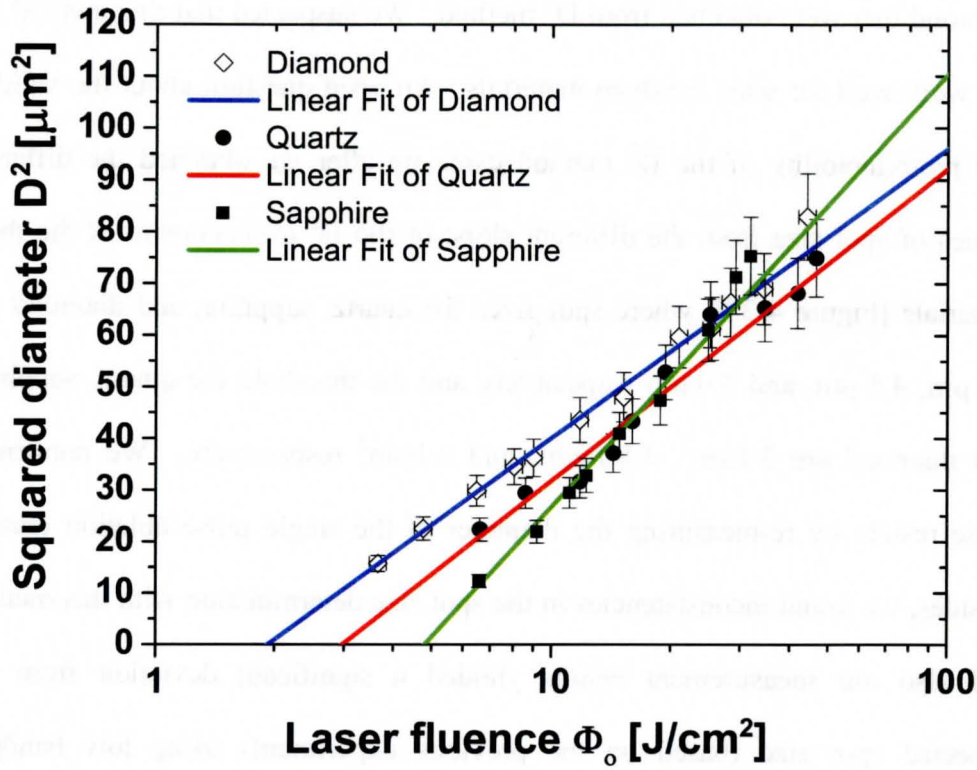

Figure 4-38: Squared diameter D^2 as a function of the logarithm of laser fluence of quartz, sapphire, and diamond.

This study involved laser experimental works that have been carried out from June 2007 to January 2008. In May 2008, an erratum about laser fluence determination was published by Puerto et al [120]. This erratum might support our question above about the inconsistency of spot size determination with D^2 analysis on quartz, sapphire, and diamond samples. They mentioned that the beam intensity profiling with D^2 method requires the use of a low band-gap material which shows linear absorption at the laser photon energy They observe a substantial deviation from the linear behavior for fused silica and significant

data scattering. For moderate band gap materials such as borosilicate glass (Eg=4 eV), spot size determination using this method appears to provide correct values. The linear absorption in the materials is a condition that is not satisfied in quartz, sapphire, and diamond.

Besides the question of possible issues when working with wide bandgap materials, we also have the possible issues when we are using a very small spot size. The precision and the reproducibility of this method need to be examined further. A direct example from this study is the spot size of 50× objective (2.8μm) that we expected to be much smaller.

Based on the general investigations of the features revealed by the femtosecond laser pulses with each material, we would like to correlate the properties of the materials with the features. As the absorption is by nonlinear photoionization, the value of the bandgap will determine how easily the incident photons will be absorbed. Generally quartz, sapphire and diamond behave distinctively upon laser wavelength due to different order of the absorption process.

A larger bandgap could lead to less absorption [125]. The larger bandgap of sapphire (Eg=9.9 eV) [20] would imply lower absorption and hence less ablation. The reduced damage severity with femtosecond pulses and higher modification threshold (4.8 J/cm^2) were expected. Supported by the sapphire's high value of the enthalpy of fusion (111.4 kJ/mol) [126-128] which is a measure

of the bond strength, we can deduce that sapphire can be damaged less easily than other two materials (quartz and diamond).

Quartz with slightly lower energy bandgap (Eg=8.4 eV) than sapphire [20] is expected to have slightly higher absorptivity and more ablation. The enthalpy of fusion of quartz is quite low (8.51 kJ/mol) [128] as compared to that of sapphire. So the damage severity is higher than in sapphire as indicated with the pronounced cracking phenomenon. Those above-mentioned factors cause quartz to have a lower modification threshold compared to sapphire (3 J/cm^2).

Diamond, with the lowest energy bandgap among the three dielectric materials (Eg=5.5 eV) [20, 21], is expected to have the highest absorptivity and hence more material ablation (removal). We can see from previous sections (refer to section 4.3) that the damage on the diamond is indicated with clear boundaries. Nevertheless, the material removal in diamond is not as pronounced as the material modification especially on the surface, as indicated with very broad range of ripples formation. This lower material removal phenomenon is related to the high enthalpy of fusion (104.6 kJ/mol at the solid-liquid-vapor triple point) [128]. Also, the lower modification threshold value of diamond (2 J/cm^2) may be caused by the use of a polycrystalline diamond, while the quartz and sapphire used in this study were single crystal. Grain boundaries in polycrystalline materials will increase the absorptivity coefficient, thus reducing the modification threshold.

5 Concluding Remarks

This study presents single, plural ($2 \leq N \leq 10$ pulses), multiple pulse ablations ($10 < N \leq 100$ pulses) and continuous lines micromachining on the surface and also continuous lines irradiation in the sub-surface of wide bandgap materials, e.g. quartz, sapphire, and diamond. All the experiments were performed with femtosecond pulses of 140-200 fs duration at a centered wavelength of 800 nm, continued with post mortem plan view and cross-section materials analysis with optical microscopy, SEM, FIB, AFM, and TEM.

The purpose of this research work was to look closer and deeper into what happened after the interaction of femtosecond laser pulses and wide bandgap materials. Previous studies focused on the semiconductors due to the demand for knowledge to allow semiconductor or photonic devices to be processed with femtosecond laser pulses. However, the applications of dielectric and transparent materials are also increasing. Based on those applications, this study was performed. In order to achieve a closer and deeper investigation, the focused ion beam method was exploited.

From surface and sub-surface laser micromachining, we observed that quartz is very prone to cracking in particular direction, 45° from the horizontal

axis that will cross and form the r or z cleaving planes. In this regime, we did not observe laser induced periodic surface structure. We observed alternating amorphous and crystalline core in the focal plane of the tightly focus laser beam in the bulk α-quartz crystal with the parallel orientation with respect to electric field polarization using FIB and TEM investigations. The bulk quartz has been modified into alternating amorphous regions in the crystalline matrix with cracks growing from the amorphous region along the irradiated area. Our experiment proves that a laser tightly focused in the bulk of quartz does not necessarily create any voids. The absence of compositional changes after femtosecond pulse laser irradiation has been confirmed with EELS investigation.

Some ripples were observed in sapphire at a consecutive number of pulses slightly below the ablation threshold. The surface ripples formed from the edge to the center of the crater. The continuous line micromachining on the surface reveals three different structures, droplet-like structures at higher fluence, overlapped path and crosshatch structures at fluence close to the modification threshold, and fine ripples at the lower fluence. Unfortunately we could not observe the structure transformations in the sub-surface micromachining of sapphire. We have not determined the best parameters for FIB to investigate the confined damage in the bulk sapphire.

The investigations on polycrystalline diamond reveal the strong tendency of ripples formation. Three consecutive pulses will form well-defined ripples on diamond. The surface ripples formed from the center to the edge of the crater.

Very broad range of spacing, both near wavelength and sub-wavelength ripples were observed in continuous lines micromachining on the surface of diamond with varied surface modification morphology. It is suggested to use single crystal diamond to continue the investigation on diamond to eliminate the uncertainties in the results. There is still enough room to investigate diamond and especially with FIB characterization method. The best FIB parameters have not been determined to reveal the sub-surface features. The possible graphitization due to femtosecond pulses on the irradiated area can be interesting subject for further investigation.

Electric field polarization direction plays an important role in the orientation of the surface ripples in sapphire, diamond and alternating amorphous-crystalline in the bulk crystalline quartz. However the exact mechanism of formation of ripples and/or sub-surface periodic structure and the dependency with the electric field polarization are still an open discussion.

The determination of the spot size and the modification threshold of the wide bandgap materials is still an issue in term of the accuracy and the consistency of the results. This issue is currently solved by using a low bandgap material, which shows linear absorption at the laser photon energy, together with wide bandgap investigation as explained in the erratum. With a growing number of results in the field of femtosecond laser pulses and material interaction, a modeling study would be of great interest.

References

[1] Hirano, M., Kawamura, K., & Hosono, H. (2002). Micro and nano-machining of transparent dielectrics by interfered two short laser pulses. *International Symposium on Photonic Glass (ISPG 2002), , 5061* 89-95.

[2] Kamlage, G., Bauer, T., Ostendorf, A., & Chichkov, B. N. (2003). Deep drilling of metals by femtosecond laser pulses. *Applied Physics A: Materials Science and Processing, 77*(2), 307-310.

[3] Bonse, J., Wrobel, J. M., Kruger, J., & Kautek, W. (2001). Ultrashort-pulse laser ablation of indium phosphide in air. *Applied Physics A (Materials Science Processing), A72*(1), 89-94.

[4] Borowiec, A., & Haugen, H. K. (2004). Femtosecond laser micromachining of grooves in indium phosphide. *Applied Physics A (Materials Science Processing), A79*(3), 521-9.

[5] Loesel, F. H., Kurtz, R. M., Horvath, C., Sayegh, S., Mourou, G., Bille, J. F., et al. (1999). Ultra-precise medical applications with ultrafast lasers: Corneal surgery with femtosecond lasers. *Proceedings of SPIE - the International Society for Optical Engineering, 3564*, 86-93.

[6] Perry, M. D., Stuart, B. C., Banks, P. S., Feit, M. D., Yanovsky, V., & Rubenchik, A. M. (1999). Ultrashort-pulse laser machining of dielectric materials. *Journal of Applied Physics, 85*(9), 6803-10.

[7] Richardson, M., Zoubir, A., Shah, L., Rivero, C., Lopez, C., Richardson, K., et al. (2004). Ablation and optical property modification of transparent materials with femtosecond lasers. *35th Annual Boulder Damage Symposium Proceedings: Laser-Induced Damage in Optical Materials 2003, , 5273* 472-481.

[8] Rayner, D. M., Naumov, A., & Corkum, P. B. (2005). Ultrashort pulse non-linear optical absorption in transparent media. *Optics Express, 13*(9), 3208-3217.

[9] Dupont, E., Zhu, X., Chiu, S., Moisa, S., Buchanan, M., Gao, M., et al. (2000). In situ repair of optoelectronic devices with femtosecond laser pulses. *Semiconductor Science and Technology, 15*, 15-18.

[10] Kautek, W., Krueger, J., Beyer, E., Cantello, M., La Rocca, A. V., Laude, L. D., et al. (1994). Femtosecond pulse laser ablation of metallic, semiconducting, ceramic, and biological materials. Paper presented at the , *2207* 600-611. doi:10.1117/12.184768

[11] Krueger, J., & Kautek, W. (1995). Femtosecond-pulse laser processing of metallic and semiconducting thin films. *Laser-Induced Thin-Film Processing, , 2403* 436-447.

[12] Ashkenasi, D., Herbst, G., Rosenfeld, A., Varel, H., Lorenz, M., Stoian, R., et al. (1998). Laser ablation and structuring of transparent materials with ultrashort laser pulses. Paper presented at the , *3343* 400-410. doi:10.1117/12.321575

[13] Liu, D., Li, Y., An, R., Dou, Y., Yang, H., & Gong, Q. (2006). Influence of focusing depth on the microfabrication of waveguides inside silica glass by femtosecond laser direct writing. *Applied Physics A (Materials Science Processing), A84*(3), 257-60.

[14] Diez-Blanco, V., Siegel, J., & Solis, J. (2007). Femtosecond laser writing of optical waveguides with controllable core size in high refractive index glass. *Applied Physics A: Materials Science and Processing, 88*(2), 239-242.

[15] Cheng, Y., Sugioka, K., & Midorikawa, K. (2004). Microfluidic laser embedded in glass by three-dimensional femtosecond laser microprocessing. *Optics Letters, 29*(17), 2007-9.

[16] Glezer, E. N., Milosavljevic, M., Huang, L., Finlay, R. J., Her, T. -., Callan, T. P., et al. (1996). Three-dimensional optical storage inside transparent materials. *Optics Letters, 21*(24), 2023-5.

[17] Miller, J. C., & Haglund, R. F. (Eds.). (1998). *Laser ablation and desorption*Academic Press.

[18] Von Der Linde, D., Sokolowski-Tinten, K., & Bialkowski, J. (1997). Laser-solid interaction in the femtosecond time regime. *Applied Surface Science, 109-110*, 1-10.

[19] Yao, Y. L., Chen, H., & Zhang, W. (2005). Time scale effects in laser material removal: A review. *International Journal of Advanced Manufacturing Technology, 26*(5), 598-608.

[20] Weber, M. J. (2003). *Handbook of optical materials* . Boca Raton: CRC Press.

[21] Vaseashta, A. (2002). Semiconductor devices using thin films of diamond and other wide band gap materials. *Proceedings of the Eleventh International Workshop on the Physics of Semiconductor Devices, , 2* 956-62.

[22] Ozkan, A. M., Malshe, A. P., Railkar, T. A., Brown, W. D., Shirk, M. D., & Molian, P. A. (1999). Femtosecond laser-induced periodic structure writing on diamond crystals and microclusters. *Applied Physics Letters, 75*(23), 3716-18.

[23] Borowiec, A., & Haugen, H. K. (2003). Subwavelength ripple formation on the surfaces of compound semiconductors irradiated with femtosecond laser pulses. *Applied Physics Letters, 82*(25), 4462-4.

[24] Wu1, Q., Ma1, Y., Fang1, R., Liao1, Y., Yu1, Q., Chen, X., et al. (2003). Femtosecond laser-induced periodic surface structure on diamond film. *Applied Physics Letters, 82*(11), 1703-5.

[25] Bonse, J., Munz, M., & Sturm, H. (2005). Structure formation on the surface of indium phosphide irradiated by femtosecond laser pulses. *Journal of Applied Physics, 97*(1), 13538-1.

[26] Jia, T. Q. 1., Chen, H. X., Huang, M., Zhao, F. L., Qiu, J. R., Li, R. X., et al. (2005). Formation of nanogratings on the surface of a ZnSe crystal irradiated by femtosecond laser pulses. *Physical Review B (Condensed Matter and Materials Physics), 72*(12), 125429-1.

[27] Hsu, E. M., Crawford, T. H. R., Maunders, C., Botton, G. A., & Haugen, H. K. (2008). Cross-sectional study of periodic surface structures on gallium phosphide induced by ultrashort laser pulse irradiation. *Applied Physics Letters, 92*(22), 221112.

[28] Hsu, E. M., Crawford, T. H. R., Tiedje, H. F., & Haugen, H. K. (2007). Periodic surface structures on gallium phosphide after irradiation with 150 fs-7 ns laser pulses at 800 nm. *Applied Physics Letters, 91*(11), 111102.

[29] Bonse, J., Baudach, S., Kruger, J., Kautek, W., & Lenzner, M. (2002). Femtosecond laser ablation of silicon-modification thresholds and morphology. *Applied Physics A (Materials Science Processing), A74*(1), 19-25.

[30] Hnatovsky, C., Taylor, R. S., Simova, E., Rajeev, P. P., Rayner, D. M., Bhardwaj, V. R., et al. (2006). Fabrication of microchannels in glass using focused femtosecond laser radiation and selective chemical etching. *Applied Physics A: Materials Science and Processing, 84*(1), 47-61.

[31] Wortmann, D., Gottmann, J., Brandt, N., & Horn-Solle, H. (2008). Micro- and nanostructures inside sapphire by fs-laser irradiation and selective etching. *Optics Express, 16*(3), 1517-1522.

[32] Malshe, A., & Deshpande, D. (2004). Nano and microscale surface and sub-surface modifications induced in optical materials by femtosecond laser machining. *Journal of Materials Processing Technology, 149*(1-3), 585-590.

[33] Zimmer, K., & Bohme, R. (2005). Precise etching of fused silica for refractive and diffractive micro-optical applications. *Optics and Lasers in Engineering, 43*(12), 1349-1360.

[34] Alavi, M., Buttgenbach, S., Schumacher, A., & Wagner, H. -. (1992). Fabrication of microchannels by laser machining and anisotropic etching of silicon. *EUROSENSORS V Conference, , A32*(1) 299-302.

[35] Mazilu, M., Juodkazis, S., Ebisui, T., Matsuo, S., & Misawa, H. (2007). Structural characterization of shock-affected sapphire. *Applied Physics A: Materials Science and Processing, 86*(2), 197-200.

[36] Matsuo, S., Tabuchi, Y., Okada, T., Juodkazis, S., & Misawa, H. (2006). Femtosecond laser assisted etching of quartz: Microstructuring from inside. *Applied Physics A (Materials Science Processing), A84*(1-2), 99-102.

[37] Liu, X., Du, D., & Mourou, G. (1997). Laser ablation and micromachining with ultrashort laser pulses. *IEEE Journal of Quantum Electronics, 33*(10), 1706-1716.

[38] Lenzner, M., Kruger, J., Sartania, S., Cheng, Z., Spielmann, C., Mourou, G., et al. (1998). Femtosecond optical breakdown in dielectrics. *Physical Review Letters, 80*(18), 4076-4079.

[39] Dana, J. D. (1892). *The system of mineralogy : Descriptive mineralogy* (6th ; entirely rewritten and much enl ed.). New York: John Wiley & sons.

[40] Klein, C., Hurlbut, C. S., & Dana, J. D. (1999). *Manual of mineralogy : (after james D. dana)* (21st , rev ed.). New York: J. Wiley.

[41] Nakamoto, T. 1. (1989). Study on quartz thickness-shear resonator immersed in liquid and its biosensor application. *17*, 619-26.

[42] Lin, Y., Lu, F., & Lu, L. (2005). Application of quartz transducer technique in SHPB. *Gaoya Wuli Xuebao/Chinese Journal of High Pressure Physics, 19*(4), 299-304.

[43] Danel, J. S., Dufour, M., & Michel, F. (1993). Application of quartz micromachining to the realization of a pressure sensor. *Proceedings of the 47th IEEE Annual International Frequency Control Symposium,* 587-596.

[44] Min1, C. (2005). Design and application of the small diameter quartz pressure gauge. *Instrument Techniques and Sensor,* (3), 8-25.

[45] Hamrour, M. R. 1., & Galliou, S. 1. (1994). Analysis of the infrared sensitivity of a quartz resonator application as a thermal sensor. *Proceedings of IEEE Ultrasonics Symposium, , 1* 513-16.

[46] Seo, M. (1999). Application of quartz crystal microbalance to corrosion research. *Zairyo to Kankyo/ Corrosion Engineering, 48*(10), 610-620.

[47] Michalzik, M., Wendler, J., Rabe, J., Buttgenbach, S., & Bilitewski, U. (2005). Development and application of a miniaturised quartz crystal microbalance (QCM) as immunosensor for bone morphogenetic protein-2. *Sensors and Actuators, B: Chemical, 105*(2), 508-515.

[48] Neil, W., Garrard, C., & Charlesworth, J. M. (1995). Application of the quartz crystal microbalance to measurement of the concentration of electrolyte in lead/acid batteries. *Journal of Power Sources, 56*(1), 19-23.

[49] Barish, B. C., Billingsley, G., Camp, J., Kells, W. P., Sanders, G. H., Whitcomb, S. E., et al. (2002). Development of large size sapphire crystals for laser interferometer gravitational-wave observatory. *IEEE Transactions on Nuclear Science, 49 II*(3), 1233-1237.

[50] Willander, M., Friesel, M., Wahab, Q., & Straumal, B. (2006). Silicon carbide and diamond for high temperature device applications. *Journal of Materials Science: Materials in Electronics, 17*(1), 1-25.

[51] Gondek, J. 1., & Kocol, J. (2001). New hybrid with Q-factor-pass-band microwave filter constructed with dielectric resonators and coupled with a thick-film microstrip line made in diamond substrates. *Diamond and Related Materials, 10*(8), 1511-14.

[52] Higaki, K. 1., Nakahata, H. 1., Kitabayashi, H. 1., Fujii, S. 1., Tanabe, K. 1., Seki, Y. 1., et al. (1997). High power durability of diamond surface acoustic wave filter. *IEEE Transactions on Ultrasonics, Ferroelectrics and Frequency Control, 44*(6), 1395-400.

[53] Assouar, M. B. 1., Benedic, F. 1., Elmazria, O. 1., Belmahi, M. 1., Jimenez Rioboo, R. 1., & Alnot, P. 1. (2001). MPACVD diamond films for surface acoustic wave

filters. *11th European Conference on Diamond, Diamond-Like Materials, Carbon Nanotubes, Nitrides and Silicon Carbide (Diamond 2000), , 10*(3-7) 681-5.

[54] Adamschik, M., Muller, R., Gluche, P., Floter, A., Limmer, W., Sauer, R., et al. (2001). Analysis of piezoresistive properties of CVD-diamond films on silicon. *Diamond and Related Materials, 10*(9-10), 1670-1675.

[55] Fu, Y. 1., Yan, B. 1., Loh, N. L. 1., Sun, C. Q., & Hing, P. (2000). Characterization and tribological evaluation of MW-PACVD diamond coatings deposited on pure titanium. *Materials Science & Engineering A (Structural Materials: Properties, Microstructure and Processing), A282*(1-2), 38-48.

[56] Lipatov, E. I. 1., Panchenko, A. N. 1., Tarasenko, V. F. 1., Schein, J., & Krishnan, M. (2001). Photosensitivity of a diamond detector to laser radiation in the 220-355-nm region. *Quantum Electronics, 31*(12), 1115-17.

[57] Zhu, X., Aslam, D. M., Tang, Y., Stark, B. H., & Najafi, K. (2004). The fabrication of all-diamond packaging panels with built-in interconnects for wireless integrated microsystems. *Journal of Microelectromechanical Systems, 13*(3), 396-405.

[58] Zhu, X., & Aslam, D. M. (2006). CVD diamond thin film technology for MEMS packaging. *Diamond and Related Materials, 15*(2-3), 254-258.

[59] Jackson, M. J. 1., & Ahmed, W. (2001). Deposition of diamond coatings on cutting tools used for micro machining applications. *Proceedings of the Eighteenth National Conference on Manufacturing Research,* 385-9.

[60] Tonshoff, H. K. 1., Hillmann-Apmann, H. 1., & Asche, J. 1. (2002). Diamond tools in stone and civil engineering industry: Cutting principles, wear and applications. *12th European Conference on Diamond, Diamond-Like Materials, Carbon Nanotubes, Nitrides and Silicion Carbide (Diamond 2001), , 11*(3-6) 736-41.

[61] Sein, H., Ahmed, W., Rego, C. A., Jones, A. N., Amar, M., Jackson, M., et al. (2003). Chemical vapour deposition diamond coating on tungsten carbide dental cutting tools. *Journal of Physics Condensed Matter, 15*(39), 2961-2967.

[62] Thompson, R. G. 1., Konovalov, V. V. 1., & Harman, K. M. 1. (2006). Die coatings: Nanostructured diamond coatings for cutting tools. *Die Casting Engineer, 50*(3), 50-3.

[63] Jackson, M. J. 1., Robinson, G. M. 1., & Ahmed, W. (2006). Micromachining selected metals using diamond coated cutting tools. *International Journal of Nanomanufacturing, 1*(2), 304-17.

[64] Zong, W. J. 1., Cheng, K. 1., Li, D. 1., Sun, T. 1., & Liang, Y. C. 1. (2007). The ultimate sharpness of single-crystal diamond cutting tools-part I: Theoretical analyses and predictions. *International Journal of Machine Tools & Manufacture, 47*(5), 852-63.

[65] Ageev, V. P., Builov, L. L., Konov, V. I., Kuzmichev, A. V., Pimenov, S. M., Prokhorov, A. M., et al. (1988). Interaction of laser light with diamond films. *Soviet Physics - Doklady, 33*(11), 840-2.

[66] Jeschke, H. O., Garcia, M. E., & Bennemann, K. H. (1999). Theory for laser-induced ultrafast phase transitions in carbon. *COLA'99, , A69* 49-53.

[67] Wang, C. Z., Ho, K. M., Shirk, M. D., & Molian, P. A. (2000). Laser-induced graphitization on a diamond (111) surface. *Physical Review Letters, 85*(19), 4092-5.

[68] BIMR. (2005). *Femtosecond laser micromachining manual.* Unpublished manuscript.

[69] Hsu, E. (2007). Study of ultrashort pulse laser induced surface ripples and investigation of other applications of ultrashort pulse laser micromachining and ablation. (MASc, McMaster University).

[70] Borowiec, A., Haugen, H. K., & McMaster University. Dept. of Engineering Physics. (2004). *Ablation and micromachining of INP with femtosecond laser pulses*

[71] Bäuerle, D. (2000). *Laser processing and chemistry* (3rd ed.). Berlin Heidelberg: Springer-Verlag.

[72] Rethfeld, B., Sokolowski-Tinten, K., Temnov, V. V., Kudryashov, S. I., Bialkowski, J., Cavalleri, A., et al. (2000). Ablation dynamics of solids heated by femtosecond laser pulses. *Nonreasonant Laser-Matter Interaction (NLMI-10), , 4423* 186-196.

[73] Motoyashiki, Y., Bruckner-Foit, A., Englert, L., Haag, L., Wollenhaupt, M., & Baumert, T. (2006). Use of femtosecond laser technique for studying physically small cracks. *International Journal of Fracture, 139*(3-4), 561-568.

[74] Chichkov, B. N., Momma, C., Nolte, S., von Alvensleben, F., & Tuennermann, A. (1996). Femtosecond, picosecond and nanosecond laser ablation of solids. *Applied Physics A: Materials Science & Processing, 63*(2), 109-115.

[75] Crawford, T. H. R., Yamanaka, J., Hsu, E. M., Botton, G. A., & Haugen, H. K. (2008). Femtosecond laser irradiation of metal and thermal oxide layers on silicon: Studies utilising cross-sectional transmission electron microscopy. *Applied Physics A: Materials Science and Processing, 91*(3), 473-478.

[76] Borowiec, A., Couillard, M., Botton, G. A., & Haugen, H. K. (2004). Sub-surface damage in indium phosphide caused by micromachining of grooves with femtosecond and nanosecond laser pulses. *Applied Physics A: Materials Science and Processing, 79*(8), 1887-1890.

[77] Couillard, M., Borowiec, A., Haugen, H. K., Preston, J. S., Griswold, E. M., & Botton, G. A. (2007). Subsurface modifications in indium phosphide induced by single and multiple femtosecond laser pulses: A study on the formation of periodic ripples. *Journal of Applied Physics, 101*(3), 033519.

[78] MRL Columbia University, NMRC University of Nebraska-Lincoln, RCAM Southern Methodist University. (2000). http://www.mrl.columbia.edu/ntm/index.html

[79] Ready, J. F. (2001). In Farson D. F. (Ed.), *LIA handbook of laser materials processing* . Orlando, FL: Laser Institute of America.

[80] Boyd, R. W. (2003). *Nonlinear optics* (2nd ed.). Boston: Academic Press.

[81] Liu, J. M. 1. (1982). Simple technique for measurements of pulsed gaussian-beam spot sizes. *Optics Letters, 7*(5), 196-8.

[82] Tran, D. V., Zheng, H. Y., Lam, Y. C., Murukeshan, V. M., Chai, J. C., & Hardt, D. E. (2005/9). Femtosecond laser-induced damage morphologies of crystalline silicon by sub-threshold pulses. *Optics and Lasers in Engineering, 43*(9), 977-986.

[83] van Driel, H. M., Young, J. F., & Sipe, J. E. (1983). LASER INDUCED PERIODIC SURFACE STRUCTURE. *Laser-Solid Interactions and Transient Thermal Processing of Materials. , 13* 197-204.

[84] Birnbaum, M. (1965). Semiconductor surface damage produced by ruby lasers. *Journal of Applied Physics, 36*(11), 3688-3689.

[85] Carl Zeiss. (2004). *Manual for the SUPRA (VP) and ULTRA scanning electron microscopes* . United Kingdom: Carl Zeiss SMT Ltd.

[86] Braga, P. C., & Ricci, D. (2004). *Atomic force microscopy : Biomedical methods and applications* . Totowa, N.J.: Humana Press.

[87] Veeco Instrument Inc. (2003). *SPM training book* Veeco Instrument Inc.

[88] Drelich, J., & Mittal, K. L. (2005). *Atomic force microscopy in adhesion studies* . Utrecht; Biggleswade: Vsp; Extenza Turpin distributor.

[89] Langford, R. M., & Petford-Long, A. K. (2001). Preparation of transmission electron microscopy cross-section specimens using focused ion beam milling. *Journal of Vacuum Science and Technology, Part A: Vacuum, Surfaces and Films, 19*(5), 2186-2193.

[90] Taniguchi, J., Ohno, N., Takeda, S., Miyamoto, I., & Komuro, M. (1998). Focused-ion-beam-assisted etching of diamond in XeF_2. *Japan/US Workshop on Formation of Ion Nanobeams, , 16*(4) 2506-10.

[91] Adams, D. P., Vasile, M. J., Mayer, T. M., & Hodges, V. C. (2003). Focused ion beam milling of diamond: Effects of H_2O on yield, surface morphology and microstructure. *Journal of Vacuum Science and Technology B: Microelectronics and Nanometer Structures, 21*(6), 2334-2343.

[92] Dana, J. D., Dana, E. S., Palache, C., Berman, H. M., & Frondel, C. (1944). *The system of mineralogy of james dwight dana and edward salisbury dana, yale university, 1837-1892.* -- (7th , ed.). New York; London: Wiley; Chapman and Hall.

[93] Sink, R. K. (2000). Cleaved-facet group-III nitride lasers.

[94] Bonse, J., Wrobel, J. M., Brzezinka, K. -., Esser, N., & Kautek, W. (2002/12/30). Femtosecond laser irradiation of indium phosphide in air: Raman spectroscopic and atomic force microscopic investigations. *Applied Surface Science, 202*(3-4), 272-282.

[95] Martin, S., Hertwig, A., Lenzner, M., Kruger, J., & Kautek, W. (2003). Spot-size dependence of the ablation threshold in dielectrics for femtosecond laser pulses. *Applied Physics A: Materials Science and Processing, 77*(7), 883-884.

[96] Gattass, R. R., Cerami, L. R., & Mazur, E. (2006). Micromachining of bulk glass with bursts of femtosecond laser pulses at variable repetition rates. *Optics Express, 14*(12), 5279-5284.

[97] Sirutkaitis, V. 1., Gaizauskas, E. 1., Kudriashov, V. 1., Barkauskas, M. 1., Vaicaitis, V. 1., Grigonis, R. 1., et al. (2003). Self-guiding supercontinuum generation and damage in bulk materials induced by femtosecond pulses. *Laser-Induced Damage in Optical Materials: 2002 and 7th International Workshop on Laser Beam and Optics Characterization, , 4932* 346-57.

[98] Saliminia, A., Nguyen, N. T., Chin, S. L., & Vallee, R. (2004). The influence of self-focusing and filamentation on refractive index modifications in fused silica using intense femtosecond pulses. *Optics Communications, 241*(4-6), 529-538.

[99] Yasumaru, N., Miyazaki, K., & Kiuchi, J. (2005). Fluence dependence of femtosecond-laser-induced nanostructure formed on TiN and CrN. *Applied Physics A: Materials Science and Processing, 81*(5), 933-937.

[100] Bhardwaj, V. R., Simova, E., Rajeev, P. P., Hnatovsky, C., Taylor, R. S., Rayner, D. M., et al. (2006). Optically produced arrays of planar nanostructures inside fused silica. *Physical Review Letters, 96*, 057404-1.

[101] Taylor, R. S., Hnatovsky, C., Simova, E., Rajeev, P. P., Rayner, D. M., & Corkum, P. B. (2007). Femtosecond laser erasing and rewriting of self-organized planar nanocracks in fused silica glass. *Optics Letters, 32*(19), 2888-2890.

[102] Hnatovsky, C., Taylor, R. S., Rajeev, P. P., Simova, E., Bhardwaj, V. R., Rayner, D. M., et al. (2005). Pulse duration dependence of femtosecond-laser-fabricated nanogratings in fused silica. *Applied Physics Letters, 87*(1), 14104-1.

[103] Hnatovsky, C., Taylor, R. S., Simova, E., Bhardwaj, V. R., Rayner, D. M., & Corkum, P. B. (2005). High-resolution study of photoinduced modification in fused silica produced by a tightly focused femtosecond laser beam in the presence of aberrations. *Journal of Applied Physics, 98*(1), 013517.

[104] Gorelik, T., Will, M., Nolte, S., Tuennermann, A., & Glatzel, U. (2003). Transmission electron microscopy studies of femtosecond laser induced modifications in quartz. *Applied Physics A: Materials Science and Processing, 76*, 309-311.

[105] Roccaforte, F., Bolse, W., & Lieb, K. -. (2001). Epitaxial crystallization of keV-ion-bombarded α quartz. *Journal of Applied Physics, 89*(7), 3611-18.

[106] McNeil, L. E., & Grimsditch, M. (1992). Pressure-amorphized SiO2 a-quartz: An anisotropic amorphous solid. *Physical Review Letters, 68*(1), 83-5.

[107] Juodkazis, S., Nishimura, K., Misawa, H., Ebisui, T., Waki, R., Matsuo, S., et al. (2006). Control over the crystalline state of sapphire. *Advanced Materials, 18*(11), 1361-1364.

[108] Palik, E. D. (1991). *Handbook of optical constants of solids II* . Boston: Academic Press.

[109] Glezer, E. N., & Mazur, E. (1997). Ultrafast-laser driven micro-explosions in transparent materials. *Applied Physics Letters, 71*(7), 882-884.

[110] Wang Dan-Ling, Li Cheng-De, Le, L., Hong, Y., & Gong Qi-Huang. (2001). Sub-diffraction-limit voids in bulk quartz induced by femtosecond laser pulses. *Chinese Physics Letters, 18*(1), 65-7.

[111] An, R., Li, Y., Dou, Y., Yang, H., & Gong, Q. (2005). Simultaneous multi-microhole drilling of soda-lime glass by water-assisted ablation with femtosecond laser pulses. *Optics Express, 13*(6), 1855-1859.

[112] Wang, Y., Dong, S., Yang, Y., Liang, Y., & Zou, H. (2006). Investigation on the fabrication of femtosecond laser induced waveguides and gratings inside quartz crystals. *2nd International Symposium on Advanced Optical Manufacturing and Testing Technologies - Advanced Optical Manufacturing and Testing Technologies, 6149* 61493.

[113] Schaffer, C. B., Jamison, A. O., & Mazur, E. (2004). Morphology of femtosecond laser-induced structural changes in bulk transparent materials. *Applied Physics Letters, 84*(9), 1441-3.

[114] Schaffer, C. B., Brodeur, A., & Mazur, E. (2001). Laser-induced breakdown and damage in bulk transparent materials induced by tightly focused femtosecond laser pulses. *Measurement Science & Technology, 12*(11), 1784-94.

[115] Glinka, Y. D. 1., Sheng-Hsien Lin, Lian-Pin Hwang, Yit-Taong Chen, & Tolk, N. H. (2001). Size effect in self-trapped exciton photoluminescence from SiO2-based nanoscale materials. *Physical Review B (Condensed Matter and Materials Physics), 64*(8), 085421-1.

[116] Tsuda, N. (2000). *Electronic conduction in oxides* (2nd rev. and enl. ed.). Berlin ; New York: Springer.

[117] Ashkenasi, D. 1., Varel, H. 1., Rosenfeld, A. 1., Noack, F. 1., & Campbell, E. E. B. 1. (1996). Pulse-width influence on the laser-induced structuring of CaF2 (111). *Applied Physics A (Materials Science Processing), 63*(2), 103-7.

[118] Jeel, Y., Becker, M. F. 1., & Walser, R. M. 1. (1988). Laser-induced damage on single-crystal metal surfaces. *Journal of the Optical Society of America B (Optical Physics), 5*(3), 648-59.

[119] Nolte, S., Will, M., Chichkov, B. N., & Tunnermann, A. (2002). Waveguides produced by ultra-short laser pulses inside glasses and crystals. *Photon Processing in Microelectronics and Photonics, , 4637* 188-196.

[120] Puerto, D., Gawelda, W., Siegel, J., Solis, J., & Bonse, J. (2008). Erratum: "plasma formation and structural modification below the visible ablation threshold in fused silica upon femtosecond laser irradiation" [applied physics letters (2007) 91 (082902)]. *Applied Physics Letters, 92*(21), 219901.

[121] Ramanathan, D., & Molian, P. A. (2002). Micro- and sub-micromachining of type IIa single crystal diamond using a ti:Sapphire femtosecond laser. *Journal of Manufacturing Science and Engineering, Transactions of the ASME, 124*(2), 389-396.

[122] Adachi, S. (1999). *Optical constants of crystalline and amorphous semiconductors : Numerical data and graphical information* . Boston: Kluwer Academic Publishers.

[123] Wagner, R., Gottmann, J., Horn, A., & Kreutz, E. W. (2006). Subwavelength ripple formation induced by tightly focused femtosecond laser radiation. *Applied Surface Science, 252*(24), 8576-8579.

[124] Dumitru, G., Romano, V., Weber, H. P., Sentis, M., & Marine, W. (2002). Femtosecond ablation of ultrahard materials. *Applied Physics A: Materials Science and Processing, 74*(6), 729-739.

[125] Chowdhury, I. H., Wu, A. Q., Xu, X., & Weiner, A. M. (2005). Ultra-fast laser absorption and ablation dynamics in wide-band-gap dielectrics. *Applied Physics A (Materials Science Processing), A81*(8), 1627-32.

[126] Speight, J. G., & Lange, N. A. (2005). *Lange's handbook of chemistry.* -- . New York: McGraw-Hill.

[127] Lide, D. R. (2006). *CRC handbook of chemistry and physics.* -- . Cleveland, Ohio: CRC Press.

[128] Lide, D. R., & Kehiaian, H. V. (1994). *CRC handbook of thermophysical and thermochemical data* . Boca Raton: CRC Press.